An Investigation of the Nanostructural Features of Avian Eggshell

Donna Lammie

Thesis submitted for the degree of Doctor of Philosophy to the Faculty of Veterinary Medicine, University of Glasgow.

August, 2006

Acknowledgements

I would like to acknowledge many people for their help during my thesis. I would like to thank Professor Tim Wess (Cardiff University) for his supervision, guidance, advice and support over the past four years. At the University of Glasgow, I would like to thank my supervisors Dr. Maureen Bain and Professor Sally Solomon for their assistance, advice and support throughout this work.

I have been fortunate to have worked with many people whose contributions were invaluable and therefore I would like to thank them. This includes Dr. Oskar Paris and Dr. Aurélien Gourrier at the Max-Planck Institute of Colloids and Interfaces, Germany, and Dr. Eva Valsami-Jones, Dr. Paul Schofield and Giulio Lampronti at the Natural History Museum, UK.

I am grateful to the Poultry Research Unit (University of Glasgow) for providing the eggshell samples and the SEM images, Dr. Kenny Stahl (Technical University of Denmark) for carrying out the Rietveld analysis, Professor David Manning (University of Newcastle) for conducting the mercury intrusion porosimetry analysis, and the Roslin Institute, Edinburgh for providing the oviducal fluid. I would also like to thank George MacLeod (University of Stirling) and Annemarie Martins (Max-Planck Institute of Colloids and Interfaces, Germany) for the preparation of thin sections of eggshell.

A major proportion of this work was undertaken at synchrotron radiation sources; therefore, I would like to thank the following people for their help: Dr. Michael Drakopoulos (presently

at Diamond), Dr. Ray Barrett and Dr. Alex Simionovici (ID18F, ESRF), Dr. Manfred Burghammer (ID13, ESRF), and Dr. Chris Martin (MPW6.2, SRS Daresbury Laboratory).

Thank you to past and present members of the research group: Jen Hiller, Craig Kennedy, Clark Maxwell, Christian Pinali, Kate Thomas, Joanna Glab, Lee Gonzalez, Graeme Cameron, Kheng-Lim Goh, Veronique Siegler, Louise Haston, Julie Laing and Craig Lawrie for their friendship, help and support. I would also like to thank Dr. Carlo Knupp for useful discussions.

I gratefully acknowledge the financial support of the Biotechnology and Biological Sciences Research Council.

Finally, many thanks go to my friends for their support and friendship over the years, and special thanks to my family and partner, Lee, for their continuous support and love.

Declaration

I hereby declare that this thesis embodies the results of my own work and that it has been composed by myself. Any exceptions to this are clearly stated in the thesis and the sources acknowledged.

Donna Lammie

Table of Contents

List of Figures

Chapter 1

Chapter 2

Chapter 3

Chapter 4

Chapter 5

Chapter 6

List of Tables

List of Abbreviations and Symbols

ADC	Analogue-to-Digital Converter
ADSC	Area Detector Systems Corporation
AIM	Acquisition Interface Module
ANOVA	A One-Way Analysis of Variance
arb. units	Arbitrary Units
θ	Incidence Angle and the Angle of Reflection
2θ	Scattering Angle
λ	Wavelength
χ	Azimuthal angle
CCD	Charge Coupled Detector
CRL	Compound Refractive Lens
d	Lattice Plane Spacing
ELISA	Enzyme-Linked Immunosorbent Assays
ESRF	European Synchrotron Radiation Facility
EXAFS	Extended X-ray Absorption Fine Structure Spectroscopy
FWHM	Full Width at Half Maximum
h,k,l	Miller Indices
ID	Insertion Device
I(q)	Scattering Intensity
ISA	Institut de Sélection Animale
J	Invariant
KB	Kirkpatrick-Baez
MPW	Multipole Wiggler
µSAXS	Microfocus Small Angle X-ray Scattering
OC-17	Ovocleidin-17
OC-116	Ovocleidin-116
P	Porod Constant
PDB	Protein Data Bank
PMMA	Polymethyl Methacrylate
P(q)	Form Factor

psi	Pounds per square inch
q	Modulus of the Scattering Vector
R	Radius of a Particle
R	Vector Length
RAPID	Refined ADC Per Input Detector
RF	Radio Frequency
R_g	Radius of Gyration
SAXS	Small Angle X-ray Scattering
SEM	Scanning Electron Microscopy
SFM	Stopped-Flow Module
S(q)	Structure Factor
SRS	Synchrotron Radiation Source
T	Size Parameter
TEM	Transmission Electron Microscopy
VCL	Vertical Crystal Layer
WAXS	Wide Angle X-ray Scattering
XRA	X-ray Associates
XRD	X-ray Diffraction

Abstract

The avian eggshell is a highly ordered bioceramic with both inorganic and organic constituents. The eggshell takes approximately 18 hours to form in the shell gland region of the hen's oviduct, a process which is repeated every 24 hours in modern hybrid laying hens, which are capable of laying in excess of 300 eggs per annum. Although the formation of the eggshell is rapid, it still results in a structure that is highly organised and which displays unique functional properties that depend on the interplay between its mineral and protein phases. The interactions between the inorganic and organic components during the formation of the eggshell however are poorly understood but it is likely that they occur at the nanometer level. Thus, it is hypothesised that structural variation at the nanostructural level will impinge on the overall structural integrity and mechanical performance of the eggshell.

In this thesis, X-ray diffraction (XRD), small angle X-ray scattering (SAXS) and microfocus small angle X-ray scattering (μSAXS) were applied to investigate the nanostructure of the eggshell. A description of these different techniques is given in Chapter 2 along with theoretical considerations as to how the resulting data presented in subsequent chapters was analysed.

In Chapter 3, thin sections of normal and abnormal eggshells, where the layers were structurally intact, were analysed using μSAXS. The results of this experiment suggest that there are nanostructural features within the different layers of normal eggshells, especially in the mammillary layer. The size dimensions of these nanopores/nanovoids were subsequently estimated to be between 3 – 5 nm in both visually normal and abnormal eggshells. However,

despite being of similar size, the distribution of these nanopores or voids was found to be disrupted in the abnormal eggshell samples.

In Chapter 4, XRD and SAXS were used to analyse powdered eggshell samples which represented different stages of gestation. In this case, the diffraction and scattering data produced were used to calculate an average size measurement of the structural features within bulk eggshell samples. The X-ray diffraction data indicated that the crystallite sizes were large, between 54 – 232 nm. However, size dimensions of approximately 5.7 – 7.2 nm were observed from the analysis of the SAXS data confirming the hypothesis that SAXS was measuring nanovoids within the crystallites arising from the presence of embedded protein.

A further study using SAXS to compare the nanostructural features of eggshells of varying mechanical strengths is presented in Chapter 5. Here, powdered eggshells from young and aged hens were compared and found to contain an average nanovoid size value of approximately 5.9 nm and 5.8 nm, respectively. These size dimensions were confirmed by a parallel study in which mercury intrusion porosimetry was used to investigate pore size distribution. It was concluded that the average size of nanovoids is comparable in eggs of different mechanical strength.

Chapter 6 describes the results of an investigation in which SAXS was used to monitor the nucleation events which take place when calcium carbonate is grown *in vitro* with and without the presence of eggshell proteins. The results of this study although preliminary suggest that the initial nucleation event is extremely rapid and provides a unique insight into the size of the calcium carbonate crystals which initially form.

The main conclusions from this thesis are summarised in Chapter 7, in relation to the effect that changes in eggshell nanostructure could have on the overall structure and function of this complex biomineralised structure. Potential further studies are also discussed.

Chapter 1

Introduction

1.1 Biomineralisation

Biomineralisation is the process of inorganic material deposition by living organisms. Studying this process involves examining the formation, structure and properties of inorganic material in biological systems. Deposition includes the uptake and extraction of particular elements from the local surroundings and the incorporation of these elements into functional structures that are formed under biological control (Mann, 2001). Biomineralisation has been studied extensively in many biological systems including bones, teeth, corals, mollusc shells and eggshells. Within all five kingdoms (monera, protoctista, fungi, plantae and animalia) organisms can produce minerals; therefore, biomineralisation is widespread (Lowenstam, 1981; Addadi and Weiner, 1992). There are more than sixty different minerals that are formed by living organisms, including organic crystals, inorganic crystals and amorphous minerals (Lowenstam and Weiner, 1989). Biomineralisation is involved in many important functions within organisms, these include support, protection, storage, motion, cutting/grinding, optical/magnetic/gravity sensing and mechanical strength (Mann, 2001).

Approximately 50% of all known biominerals are calcium derivatives (Addadi and Weiner, 1992). Calcite (avian eggshells), aragonite (mollusc shells), vaterite (shells of gastropods), calcium carbonate monohydrate, calcium carbonate hexahydrate and amorphous calcium carbonate (plant leaves) have different lattice structures but the same principal composition. Calcium carbonate monohydrate and calcium carbonate hexahydrate seem to be precursors

for the anhydrous forms of calcium carbonate (Mikkelsen *et al.*, 1999; Tlili *et al.*, 2001). The most thermodynamically stable polymorph of calcium carbonate at normal atmospheric temperatures is calcite. Rhombohedral calcite is shown in Figure 1.1. Amorphous calcium carbonate is a transient precursor phase of calcite and aragonite and is important in many calcium carbonate formation processes. It is easily dissolved and is hard to detect when associated with a crystalline form of calcium carbonate (Addadi *et al.*, 2003).

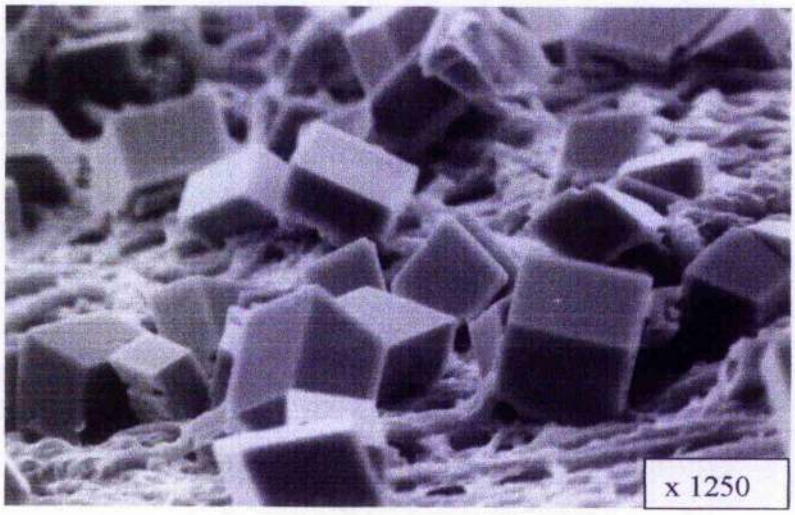

Figure 1.1 Calcite in its rhombohedral form grown on an eggshell membrane. Scanning electron micrograph courtesy of the Poultry Research Unit, University of Glasgow.

Biologically controlled mineralisation results in the deposition of mineral in a regulated manner and consequently leads to the production of functional materials. Biomineralisation occurs at different sites, these include epicellular (on the cell wall), intercellular (in the spaces between closely packed cells), intracellular (inside enclosed compartments within the cell) and extracellular (within or on an insoluble macromolecular framework outside the cell). The two sites that are more often associated with controlled biomineralisation are intracellular and extracellular. Examples of biomineralisation at intracellular sites include lipid vesicles, which are usually fluid filled sites (Lowenstam, 1981; Mann, 2001). Examples of biomineralisation at extracellular sites include bone, teeth and avian eggshells. In the case of bone, the gaps between the collagen fibres in bone are the principal site where hydroxyapatite crystals are found. With regard to the eggshell, the deposition of calcium carbonate is initiated at specific sites (nucleation sites) on the outer eggshell membrane fibres (Figure 1.2). Calcium carbonate deposition at these nucleation sites begins as spherulitic structures, where they nucleate and grow outwards radially. As well as eggshells many different organisms produce spherulitic structures: these include scleractinian corals, red calcareous algae and pennatulid sea fans (Lowenstam and Weiner, 1989). Spherulites are crystal aggregates that are formed easily *in vitro* in supersaturated solutions of calcium carbonate. Thus in biological systems, the mineralisation of spherulitic structures seems to provide a way of filling large volumes with minerals quite quickly (Addadi and Weiner, 1992).

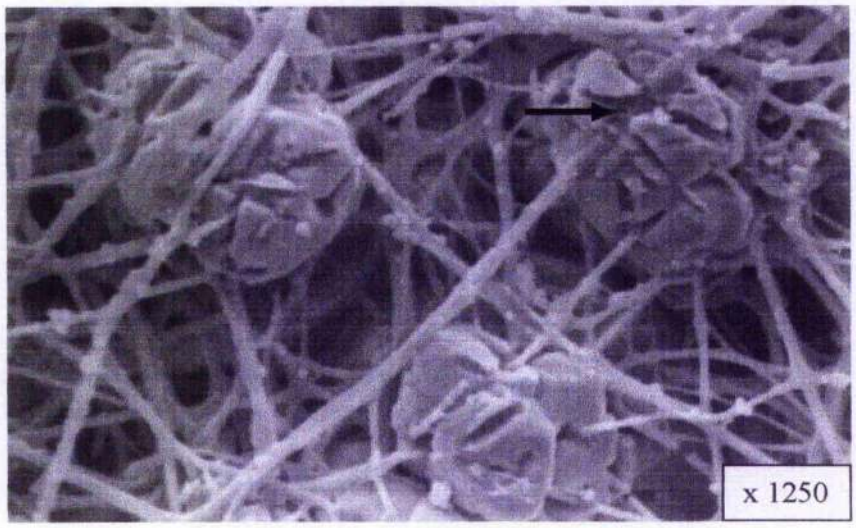

Figure 1.2 Scanning electron micrograph of an eggshell membrane where calcium carbonate deposition has occurred at specific nucleation sites on the membrane, this is shown with the black arrow. Image courtesy of the Poultry Research Unit, University of Glasgow.

In biomineralised structures, the inorganic phase associates with the organic matrix (Lowenstam, 1981; Addadi and Weiner, 1985), which is composed of proteins and polysaccharides. In some cases, for example mollusc shells and avian eggshells, the components of the matrix can be separated into water-soluble and insoluble fractions. The soluble fraction is assumed to be intracrystalline, while the insoluble fraction is intercrystalline (Meenakshi *et al.*, 1971; Krampitz and Graser, 1988). The organic matrix of biominerals has many functions; these include controlling nucleation, growth, morphology and organisation of the inorganic minerals, which in turn influence the mechanical properties of the resulting composite. Furthermore, it is also important structurally, acting as a supporting framework in eggshell, bone and teeth. The functions of biocomposites such as protection, reinforcement, movement, cutting and grinding are related to the organic matrix.

As another example within the eggshell, the organic matrix inhibits the propagation of cracks through the shell as it stops defects progressing through the inorganic material (Mann, 2001).

The formation of the avian eggshell is one of the most rapid mineralisation processes known. It takes approximately 24 hours to complete, and results in an eggshell composed of calcium carbonate in the calcitic mineral form. The resulting eggshell plays a critical role in protecting the egg contents from physical insult and bacterial penetration whilst allowing gas exchange and water loss; therefore, its functional properties are related to its structure. The eggshell structure relies on the interplay of crystalline material and biomolecules at a number of structural levels, and many external factors such as nutrition, housing and environmental stresses (Wolford and Tanaka, 1970). These can affect the physiology of the oviduct, and thus the biomineralisation events and the structural properties of this biocomposite.

1.2 Eggshell Formation

A detailed description of eggshell formation is described in Solomon (1991). In brief, following ovulation, the ovum is released from the ovary and enters the oviduct, which comprises six different regions (Figure 1.3).

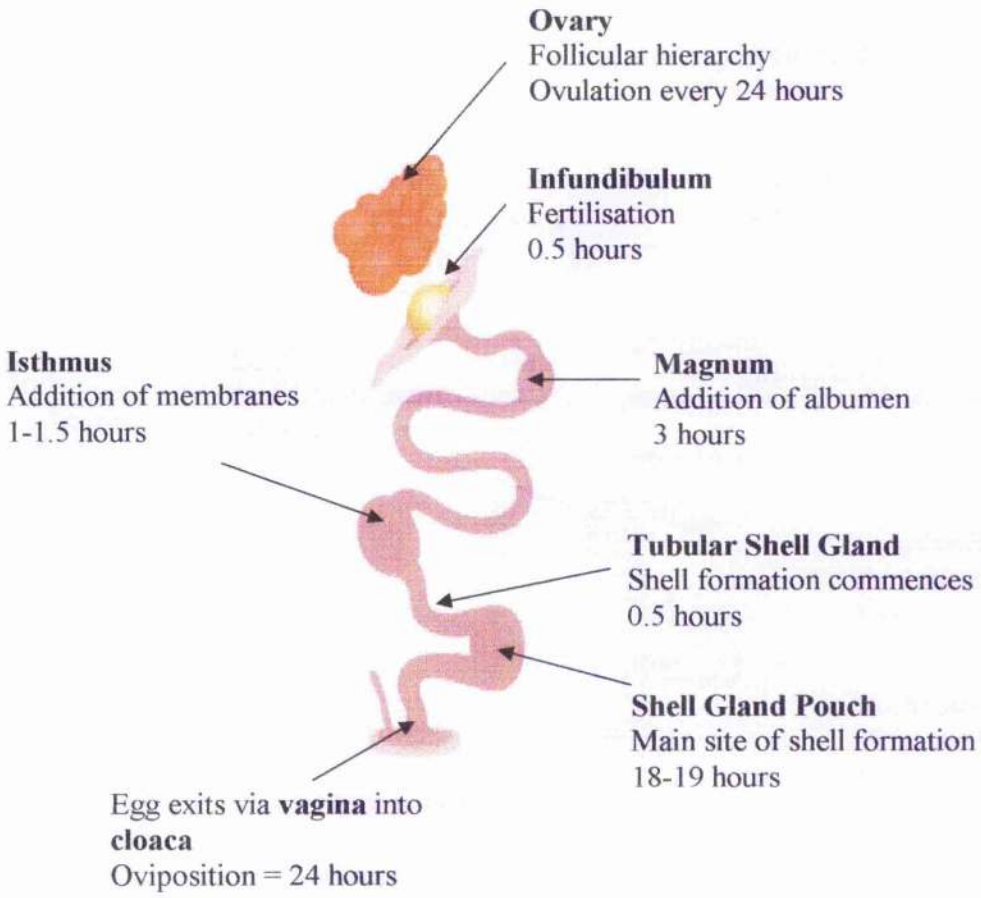

Figure 1.3 Diagram of the different regions of the reproductive tract of the hen. For the purpose of demonstration only this diagram shows an egg in both the isthmus and shell gland regions of the oviduct but in reality only one egg would normally be present in each 24 hour cycle. Graphic obtained with permission of QLK5-CT-2001-01606 "EggDefence".

The first region is the infundibulum, which is the area involved in the production of the perivitelline membrane (the membrane that surrounds the yolk) and the formation of the chalazae (rope-like structures that anchor the yolk in the centre) (Figure 1.4). The infundibulum is also the region where fertilisation takes place, if appropriate. The egg spends about 0.5 hours in this region before it enters the next part of the oviduct, the magnum, where it resides for 3 hours.

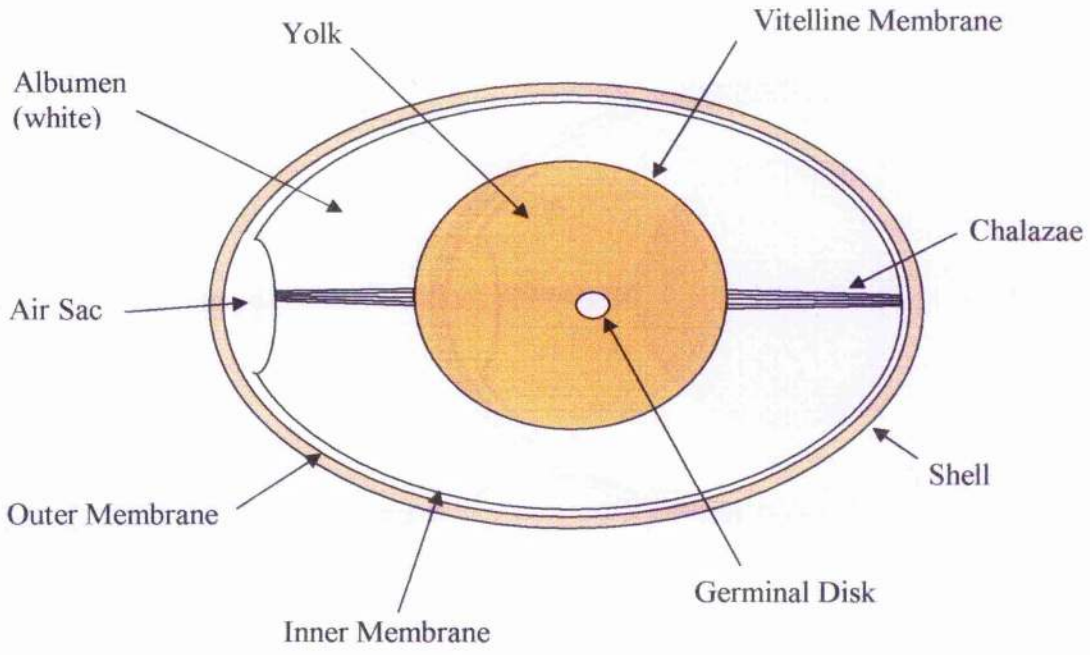

Figure 1.4 Diagrammatic representation of the different components that comprise the egg.

The magnum is the longest part of the oviduct, where the ovum acquires the egg white or albumen, a complex mixture of proteins, including ovalbumin, conalbumin, ovomucoid, lysozyme, globulins and ovomucin; however, at this stage the albumen is not in its final form. Albumen performs a number of diverse roles; for example, several components have antibacterial action. The albumen also provides a mechanical buffer for the yolk. On leaving the magnum, the forming egg travels to the isthmus where the two (inner and outer) eggshell membranes are formed over the albumen mass (Figure 1.2); the membranes are permeable to gas and water but do not permit the outward migration of the egg white proteins. The eggshell membranes are necessary for the calcification process to occur (Krampitz and Graser, 1988). The time spent in the isthmus is about 1 – 1.5 hours. The egg proceeds to the tubular shell gland, which is responsible for the initial transfer of calcium salts onto the shell membrane fibres, specifically at the mammillary cores. These sulphur rich areas are randomly located on the outer eggshell membrane fibres, and represent the initiation sites for calcium carbonate deposition (Creger, 1976). The resulting 'mammillary bodies' are best defined as the mammillary cores plus their attached calcium salts (Figure 1.5). The egg resides in the tubular shell gland for only a limited time, approximately 0.5 hours.

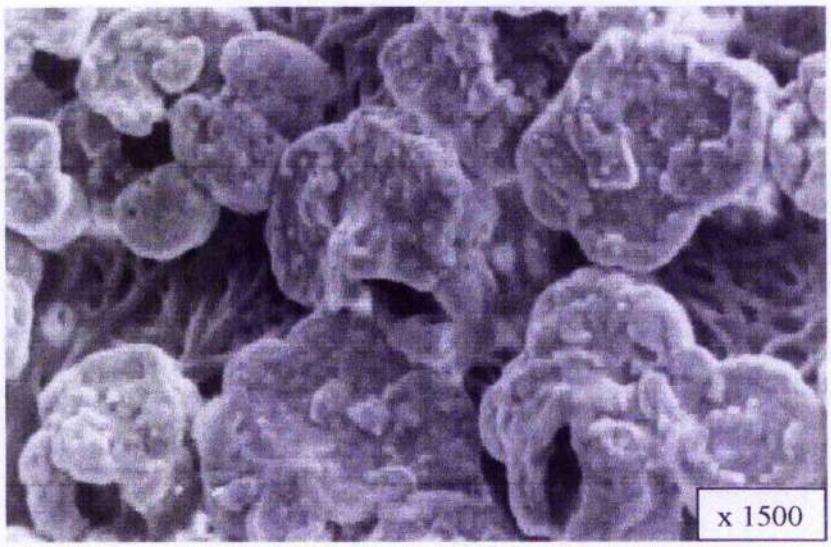

Figure 1.5 Scanning electron micrograph of mammillary bodies forming in association with the mammillary cores, which are sulphur rich regions associated with the outer shell membrane fibres, courtesy of the Poultry Research Unit, University of Glasgow.

The shell gland pouch is the main shell forming region of the oviduct, but is also responsible for the addition of plumping fluid. This glucose rich fluid swells the egg and exposes the mammillary bodies to allow deposition of calcium carbonate; it also reduces the protein content or concentration of albumen in the egg.

Mineralisation takes place in an acellular milieu (the uterine fluid), which contains the eggshell constituents in their native form (Nys *et al.*, 2004). The mammillary layer (Figure 1.6) is first to form from spherulitic crystal growth that initially proceeds outwards in all directions from the mammillary bodies, but which eventually grow upwards and outwards to fuse with their neighbours to form the palisade layer (Figure 1.6). The palisade layer makes up the majority of the eggshell thickness and takes approximately 10 hours to complete. In

total, the egg resides in the shell gland pouch for approximately 18 – 19 hours. Before oviposition, the cuticle (Figure 1.6) is added to the shell, this contains the bulk of the eggshell pigment. The fully formed egg then exits through the cloaca via the vagina. Thus, ovulation to oviposition takes around 24 hours to complete.

1.3 Eggshell Structure

1.3.1 The Ultrastructural Organisation of the Eggshell

The fully developed eggshell is a highly ordered structure (Parsons, 1982; Solomon, 1991) and is comprised of five different layers. These include, from the inside outwards, the shell membranes, of which there are two (inner and outer), the mammillary layer, palisade layer, vertical crystal layer (VCL) and the cuticle (Figure 1.6).

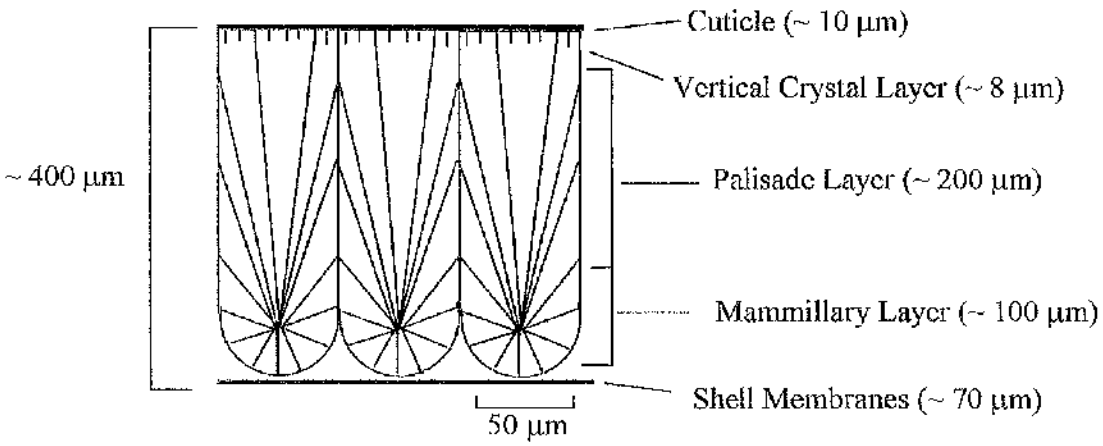

Figure 1.6 Schematic of the hen's eggshell showing the different layers and their corresponding thicknesses. The information used to create this figure was obtained from Simons (1971); Parsons (1982).

The eggshell membrane fibres, both inner and outer, are together about 70 μm thick and consist of collagen, types I and V (Wong *et al.*, 1984), and type X (Arias *et al.*, 1991). Calcium deposition occurs at initiation sites on the outer shell membrane (Creger, 1976; Dieckert *et al.*, 1989). The outer membrane is therefore firmly attached to the calcified portion of the eggshell. The mammillary layer has been described by Solomon (1991) as the structurally most diverse layer and is approximately 100 μm thick. Cain and Heyn (1964) revealed that the mammillary layer consists of "small" randomly orientated crystals. The nucleation centres are composed of microcrystals radiating out from the centre. These grow outwards and compete for growth space resulting in the formation of columnar structures (Nys *et al.*, 2004), which gives rise to the palisade layer (approximately 200 μm thick). Thus, each columnar calcite crystal unit associated with the palisade layer is grown from separate nuclei associated with the mammillary layer (Figure 1.6). Abnormal organic mammillary cores are smaller and more fragmented than normal, and have been related to weak and thin eggshells (Robinson and King, 1970).

In the palisade layer, the crystal columns continue to grow perpendicularly to the shell surface. The palisade columns are thus polygonal, conforming to the shape of the underlying mammillary bodies (Parsons, 1982). Studies have shown that the competitive growth process of adjacent calcite crystals in this layer produces a columnar microstructure that has a preferred crystallographic orientation (Rodriguez-Navarro and Garcia-Ruiz, 2000). The layer above the palisade layer and below the cuticle is called the vertical crystal layer. This is made up of narrow crystals that are aligned perpendicularly to the surface. The vertical crystal layer makes up about 8 μm of the eggshell thickness. The cuticle consists of proteins, polysaccharides and lipids, and functions to protect the egg from bacterial infection and

excessive water loss (Parsons, 1982). It is about 10 μm thick and covers the gas exchange pores. The cuticle coverage of an egg is however rarely complete (Solomon, 1991).

1.3.2 Gaseous Exchange Pores and Vesicular Pores or Holes

The eggshell is often described as a porous structure; however, it is important to distinguish between the gaseous exchange pores (Figure 1.7) and the vesicular holes or pores (Figure 1.7), which give rise to the typical honeycomb appearance of this calcified structure when viewed at high power in a scanning electron microscope.

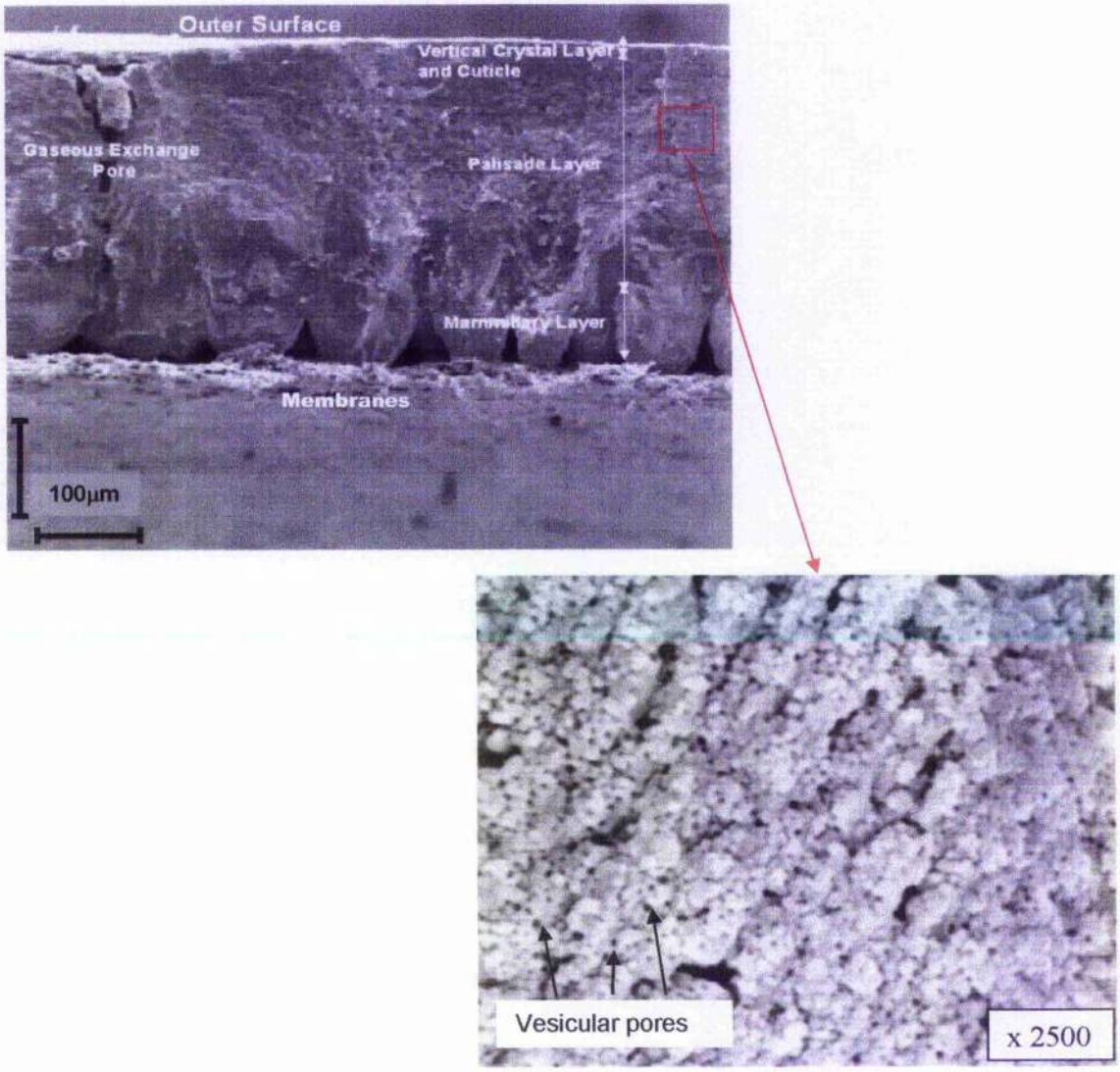

Figure 1.7 Scanning electron micrographs of the hen's eggshell illustrating gaseous exchange pores and vesicular holes or pores. The top image is taken at low power and shows a gaseous exchange pore extending though the eggshell thickness. The bottom image is taken at a much higher magnification and shows the typical honeycomb appearance of the palisade caused by the presence of vesicular pores or holes. Images courtesy of the Poultry Research Unit, University of Glasgow.

The gas exchange pores extend throughout the eggshell thickness and are essential for embryonic development. The outermost extent of these pores are usually plugged by the cuticle (Figure 1.7) but this is not always the case (Figure 1.8). Tyler (1956) measured the diameter of these pores to be 63 – 45 μm towards the outer surface and 23 – 17 μm towards the inner of the eggshell.

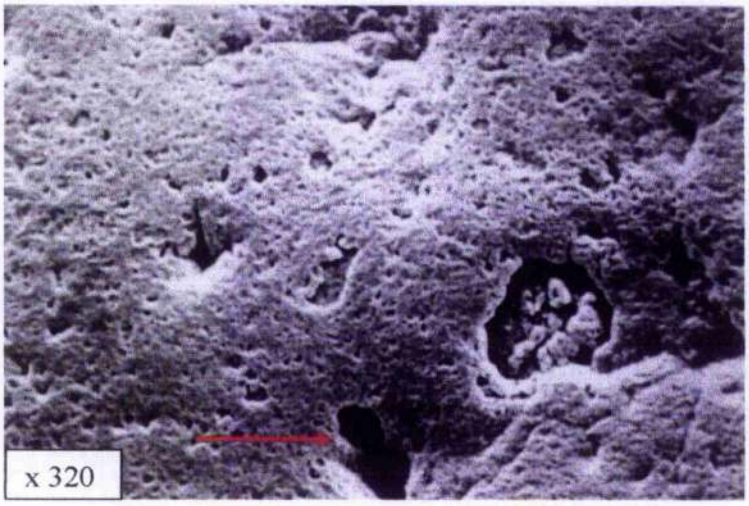

Figure 1.8 Scanning electron micrograph of the outer surface of a cuticleless eggshell to illustrate the outermost extent of a gaseous exchange pore (arrowed). Image courtesy of the Poultry Research Unit, University of Glasgow.

Vesicular holes or pores are thought to occur as a result of the modifying effects played by the organic matrix during the formation of the eggshell and appear to vary in size and distribution from the inner to outer surface of the shell (Simons, 1971). Simons (1971) also observed that the distribution of vesicular holes in eggshells differed in good and poor quality shells in such a way that poor quality shells had a more vesicular or porous appearance than

good quality shells. The porosity of the eggshell has recently been investigated in more detail by La Scala *et al.* (2000) using mercury intrusion porosimetry. This technique, based upon the pressure required to force liquid mercury into the pores, can be used to investigate vesicular pore size distribution within a solid sample, and has previously been used to investigate the porosity of other biominerals including bone (Nielsen-Marsh and Hedges, 1999). According to La Scala *et al.* (2000), the vesicular pores in eggshells range from 0.2 to above 5 μm, which coincides with the values provided by Simons (1971). To date, however, this technique has not been used to investigate if the pore size distribution of vesicular pores varies in eggs of differing quality.

1.3.3 Eggshell Microstructure and Orientation of Calcite Crystals

Crystallographic studies have been used to investigate the preferred orientation of calcite within the different layers of the avian eggshell. A polarized light microscopy study by Terepka (1963) reported that the c-axes of the calcite columns were perpendicular to the shell surface. Using X-ray diffraction, Cain and Heyn (1964) observed that the c-axis of the calcite crystals in the outer layer was inclined at 28 ± 16° to the shell normal. The structure of calcite in its rhombohedral form is shown in Figure 1.9.

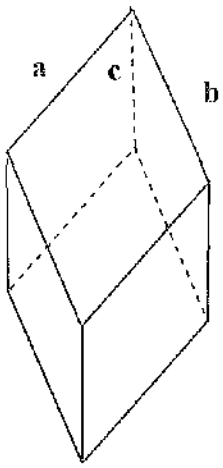

Figure 1.9 Calcite crystal structure depicted as a rhombohedron. This is a trigonal crystal system characterised by a single triad axis. The conventional unit cell dimensions are a = b = c and the angles are $\alpha = \beta = \gamma < 120°$ (Kelly and Groves, 1970).

Creger *et al.* (1976) provided evidence to suggest that each crystal nucleus may consist of a group of crystallites, which grow out in all directions during eggshell development and concluded that there are no dominant preferred crystal orientations within the mammillary layer. It has since been suggested that the lack of preferred crystal orientation in the mammillary layer indicates that the nucleation sites for calcite growth have little relationship with one another, and that this could be due to the organic nature of the fibrous membrane on which the calcite grows (Perrott *et al.*, 1981). Calcitic growth at these nucleation sites begins as spherulitic structures as described previously. Using electron diffraction, Perrott *et al.* (1981) stated that the only layer that showed any preferred orientation was the vertical crystal layer. This was subsequently confirmed by Sharp and Silyn-Roberts (1984) who suggested that calcite crystals within the eggshell of the domestic fowl have a degree of preferred orientation that develops gradually, becoming more orientated towards the outer surface.

More recently, Rodriguez-Navarro *et al.* (2002) investigated the microtextural properties of eggs laid by hens of different ages, and found that the eggshells from the aged hens showed two preferred crystal orientations in comparison to only a single preferred orientation (c-axis perpendicular to the eggshell surface) in the eggshells from the younger hens. This study also revealed a strong correlation between eggshell crystallographic texture and eggshell strength; namely, shells with a lesser degree of crystal orientation were stronger than those with a greater degree of orientation. In its role as an incubating chamber, the eggshell must be strong enough to resist mechanical insult but it must also be easy to break from the inside out to allow for hatching of the embryo. Rodriguez-Navarro *et al.* (2002) suggested that this could be why the outer portion of the shell is composed of larger crystallites than the inner area of the eggshell. The inner region of the eggshell is composed of microcrystals with spherulitic texture, this facilitates crack propagation (Nys *et al.*, 2004).

1.3.4 Grains, Crystals, Crystallites and Voids

The hen eggshell thickness is approximately 280 – 400 μm (Parsons, 1982). Cain and Heyn (1964) estimated the average particle size to be 200 μm by X-ray diffraction. Perrott *et al.* (1981) suggested that each column of calcite in the palisade layer consisted of crystallites that had a diameter of 20 – 30 μm by electron diffraction studies. Recently, Rodriguez-Navarro *et al.* (2002) used polarised light microscopy to study the crystallographic properties of eggshells and deduced that the average width of each crystal was 20 μm at the inner surface of the eggshell increasing to about 80 μm at the outer. The same method was subsequently applied in the work by Ahmed *et al.* (2005) who found that the average crystal size before moult was 72 ± 12 μm and after moult 58 ± 7 μm.

From reading these accounts it would appear that there is much confusion in the existing literature regarding the terminology used to describe the different structural features of the eggshell at different length scales. Therefore, in the context of this thesis, the term "grain" is used to describe one calcite column associated with the palisade layer, which arises from one mammillary body associated with the mammillary layer. The term "crystal" is used in the context of being one of the smaller calcite units, which comprises each calcite grain or column. The term "crystallite" is used to describe the calcite units that compose each individual crystal, and finally the term "void" is used to describe an absence of inorganic material within each crystallite, which in this thesis are described in relation to the presence of intramineral proteins associated with the organic matrix. These inter relationships are shown diagrammatically in Figure 1.10. To allow comparisons to be made with the existing literature these definitions have been assigned approximate size values.

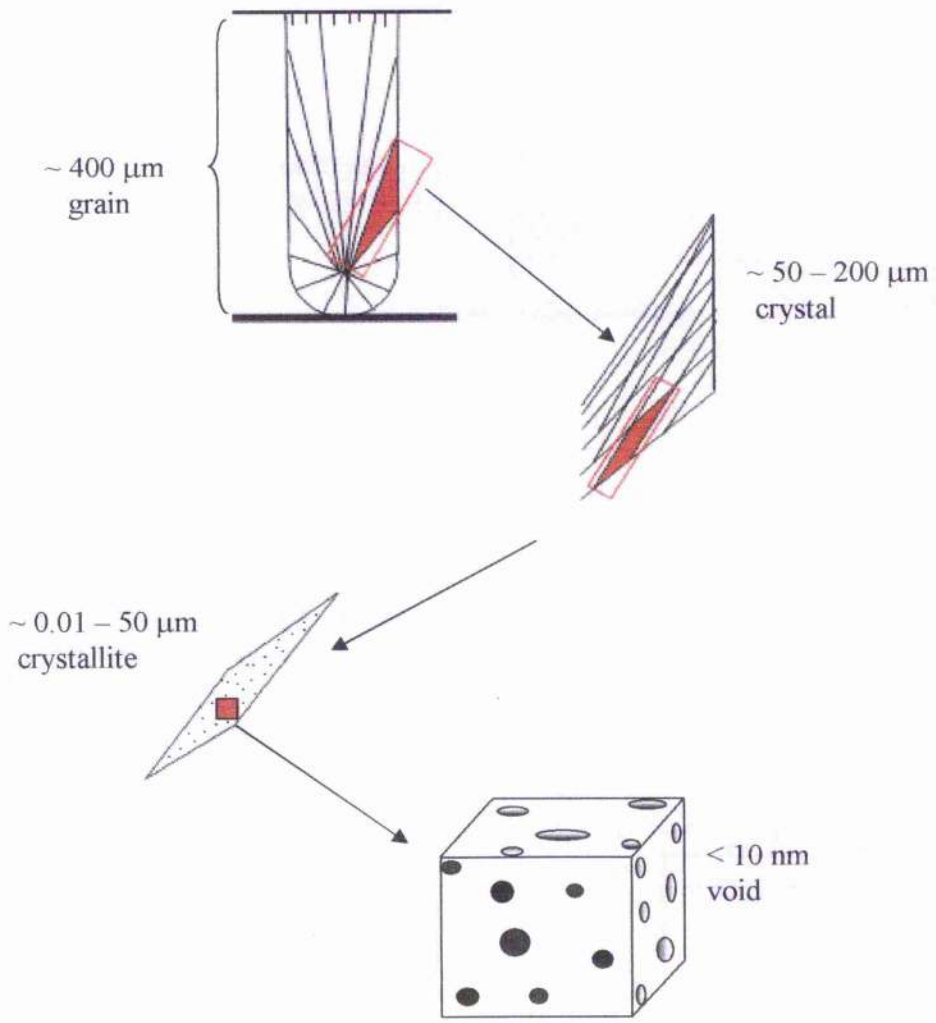

Figure 1.10 The different levels of structural detail within the eggshell as applied in this thesis. The grain column is around 400 μm; each grain consists of a mammillary body and palisade column. The grain is composed of a number of calcite crystals and each of these is composed of a large number of crystallites. Within the crystallites, measurements of a dimension that is likely to correspond to protein voids is described in this thesis and included here for completeness.

1.4 The Eggshell as a Biomineral

As previously indicated the eggshell consists of both organic and inorganic constituents: approximately 95% calcium carbonate in the form of calcite and approximately 3.5% organic material (including membranes) (Arias *et al.*, 1993; Gautron *et al.*, 1996; Nys *et al.*, 1999). There are also other trace elements within the eggshell, including magnesium and phosphorus. A study by Cusack *et al.* (2003) reported that magnesium is not uniformly distributed throughout the thickness of the eggshell. According to these authors, magnesium levels decrease from the site of nucleation until beyond fusion of the mammillary caps and then increase again until termination; this is consistent with the fact that magnesium acts as an inhibitor of crystal growth (Addadi and Weiner, 1992). Phosphorus, conversely, is only found in the outer quarter of the eggshell, and increases in concentration towards the external surface. Phosphorus is also thought to act as a crystal poison and therefore could be involved in the termination of eggshell formation (Nys *et al.*, 1991; Dennis *et al.*, 1996; Cusack *et al.*, 2003), as phosphates have been shown to inhibit calcite formation *in vitro* (Simkiss, 1964).

1.5 The Organic Matrix Component of the Eggshell

1.5.1 Morphology

The organic matrix throughout the eggshell is thought to influence nucleation, to control crystal growth and shape, and to play a role in controlling the biomechanical properties of the resulting composite, as has been suggested in other systems such as bone and dentine (Addadi and Weiner, 1992; Mann, 2001). From a morphological point of view, the organic component of the palisade layer of the shell is in the form of cross-linked fibrous sheets of protein running parallel to the shell surface. This sheet-like arrangement is absent in the mammillary layer; the organic material within this layer shows a fan-like radiation from the mammillary cone tip detected using light microscopy (Simons, 1971). Silyn-Roberts and

Sharp (1986) suggested that the organic fibrous sheets hinder crystal growth instead of controlling it, and thus their sole function is to act as a fibrous reinforcement that ties the calcite columns together. Fraser *et al.* (1999) observed using transmission electron microscopy (TEM) that the organic matrix fibres were orientated perpendicularly throughout the palisade layer and became vertically orientated and more tightly packed as they proceeded to the outer surface in the region of the vertical crystal layer. Research by Dennis *et al.* (1996) also indicated that within the vertical crystal layer, there was a vertically-orientated matrix. An example of a TEM image of the organic matrix from the palisade layer of an eggshell is shown in Figure 1.11.

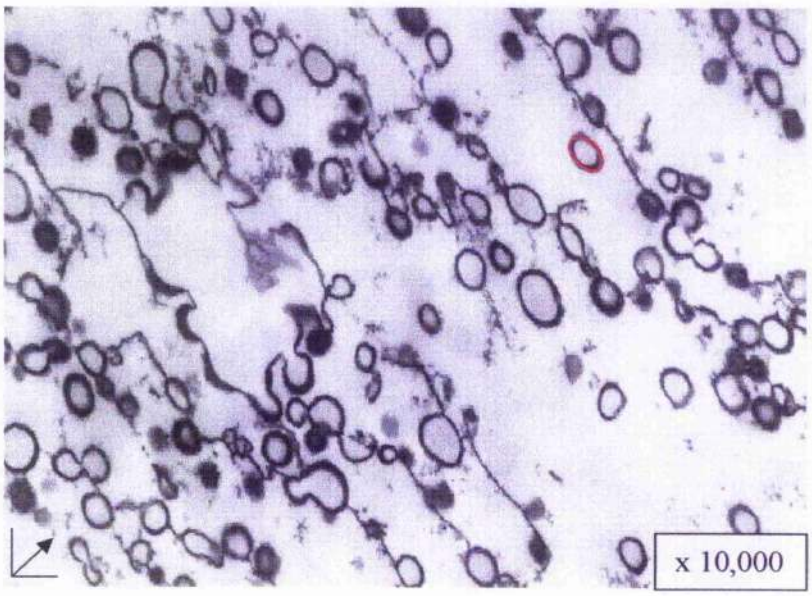

Figure 1.11 Transmission electron micrograph of the organic matrix within the palisade layer. The arrow in the bottom left hand corner indicates the direction to the outer surface. The red circle highlights a vesicular hole. Image courtesy of the Poultry Research Unit, University of Glasgow.

1.5.2 Organic Matrix – Eggshell Extract

Gautron *et al.* (1996) found that when the eggshell was decalcified through guanidine hydrochloride treatment, the amount of solubilised protein obtained in eggshell protein extraction experiments was less than 0.15 % of the shell weight and corresponded to less than 5 % of the total organic part of the eggshell. The concentration also varied depending on the stage of shell formation. Eggshell proteins are found both within and between individual calcite crystal columns and are referred to as the intramineral and extramineral organic matrix components respectively. In the initial stage (6-9 hours after ovulation) of eggshell formation, a large proportion of the soluble extracts are found in the extramineral part and at the later stages 95 % of the soluble extracts are found in the intramineral part of the eggshell (Gautron *et al.*, 1996). A greater understanding of the eggshell organic matrix has been generated by the realisation that the organic and mineral precursors of the eggshell are contained within the uterine fluid (Gautron *et al.*, 1997).

1.5.3 Organic Matrix – Precursors Present in the Uterine Fluid

The eggshell forms in the shell gland of the oviduct in an acellular milieu, which is supersaturated with calcium and bicarbonate ions and which also contains a range of proteins that are essential for eggshell formation (Arias *et al.*, 1993; Nys *et al.*, 1999). Studies have shown that the protein composition of the uterine fluid changes during the initial, growth and terminal phases of shell formation (Gautron *et al.*, 1997). The uterine fluid collected at the initial stage (6-9 hours after ovulation) corresponds to the stage when calcite crystals are deposited on the mammillary bodies. Rapid eggshell deposition occurs during the active growth phase (14-18 hours after ovulation). The terminal phase (22-23 hours after ovulation) corresponds to the end of shell calcification. Given that the uterine fluid contains all the

organic matrix proteins in their native form, it has proved most pertinent to study these proteins in terms of their specific roles.

1.5.4 Characterisation and Identification of Eggshell Matrix Proteins

Significant progress has been made in the past 15 years in the identification and characterisation of the proteins associated with the eggshell matrix. The different types of proteins that have thus far been identified can be subdivided into three groups: egg white proteins, eggshell specific proteins and ubiquitous proteins.

1.5.4.1 Eggwhite Proteins

Although normally associated with the egg white, three egg white proteins, ovalbumin (Hincke, 1995), ovotransferrin (Gautron *et al.*, 2001a) and lysozyme (Hincke *et al.*, 2000), have been isolated and identified in the eggshell matrix. An overview of their localisation in the eggshell is shown in Figure 1.12.

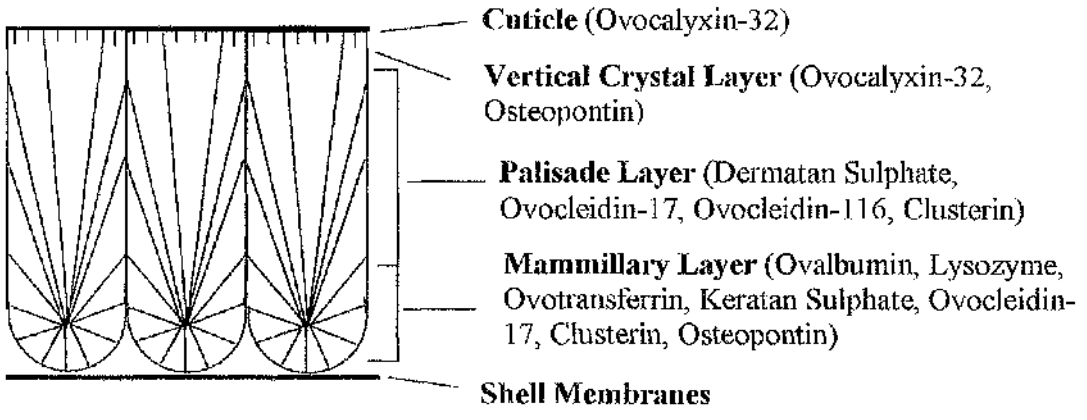

Figure 1.12 Localisation of the proteins and glycosaminoglycans found in the different layers summarised from the information given in the text.

According to Nys *et al.* (2004) the egg white proteins are likely to have a protective role as they have antimicrobial properties, whilst the specific eggshell proteins are likely to influence calcification by modifying crystal growth and thereby altering the mechanical properties of the eggshell. Ovalbumin (45 kDa) was the first egg white protein to be identified within the eggshell matrix found in the mammillae of the eggshell (Hincke, 1995) and is present in the uterine fluid mainly in the initial stages of eggshell formation (Gautron *et al.*, 1997). Previous researchers have suggested that the role of ovalbumin could be to drive calcium affinity molecules, and so influence the initiation of eggshell formation due to its localisation in the eggshell, its production in the isthmus region and its effect on nucleation (Panheleux *et al.*, 1999). The amino acid sequence of ovalbumin has been determined (Nisbet *et al.*, 1981) and the crystal structure (Figure 1.13) defined by X-ray diffraction (Stein *et al.*, 1991). An estimation of the average size of the protein can be made using small angle X-ray scattering (SAXS) by analysing the initial part of the scattering curve and determining the radius of gyration (R_g) (see subsection 2.6.2.2). Briefly, the R_g corresponds to the radius of inertia, which is the root mean square of all the electron distances from their centre of gravity (Glatter and Kratky, 1982). The R_g of ovalbumin has been determined and was found to be 2.44 ± 0.6 nm (Bu and Engelman, 1999).

Ovotransferrin, also known as conalbumin (78 kDa), is also associated with the initial phase of egg development and is present at high levels in the eggshell membranes but its intramineral localisation is limited to the mammillary knobs (Gautron *et al.*, 2001a). The crystal structure has been determined for both the fully iron-loaded diferric hen ovotransferrin (Kurokawa *et al.*, 1995) shown in Figure 1.13, and hen apo-ovotransferrin (Kurokawa *et al.*, 1999). Ovotransferrin binds iron and transports it to target cells. The radius of gyration of this protein is 2.95 nm (Zhou, 1998).

Lysozyme (15 kDa) is found in the shell membranes and in the shell matrix of the eggshell, its intramineral localisation is also limited to the mammillary knobs (Hincke *et al.*, 2000). The crystal structure of hen lysozyme has been determined by X-ray diffraction (Diamond, 1974) as seen in Figure 1.13. Lysozyme is a bacteriolytic enzyme and has antimicrobial activity against a limited number of fungi and bacteria. Studies have shown that calcite crystals grown in the presence of purified hen lysozyme exhibit altered crystal morphology suggesting that shell matrix lysozyme may have a structural role, which in soluble form influences calcium carbonate deposition during calcification (Hincke *et al.*, 2000).

Ovalbumin

Lysozyme

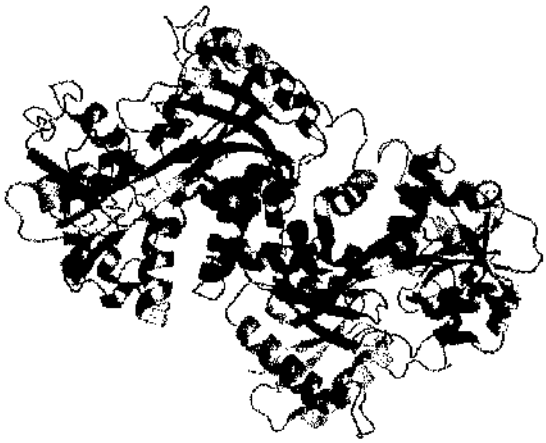

Ovotransferrin

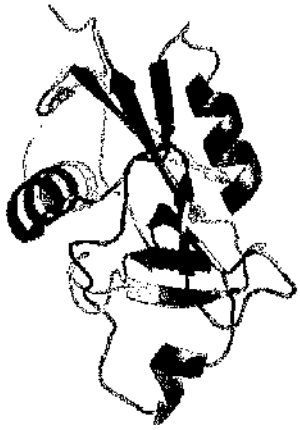

Ovocleidin-17

Figure 1.13 Crystal structures of four of the eggshell proteins obtained from the Research Collaboratory for Structural Bioinformatics Protein Data Bank (www.rcsb.org). From top left to right, ovalbumin (Protein Data Bank (PDB) code 1OVA) (Stein *et al.*, 1991), and lysozyme (PDB code 1LYZ) (Diamond, 1974). From bottom left to right, ovotransferrin (PDB code 1OVT) (Kurokawa *et al.*, 1995) and ovocleidin-17 (PDB code 1GZ2) (Reyes-Grajeda *et al.*, 2002).

1.5.4.2 Eggshell Specific Proteins

Within the eggshell there are also a number of novel proteins associated with the eggshell organic matrix, which are only secreted by tissues involved in shell calcification. The soluble intramineral matrix protein, ovocleidin-17 (OC-17), is one such protein that has been purified to homogeneity (Hincke *et al.*, 1995). This protein has been found in the mammillary layer and the palisade layer and is present in the uterine fluid at all three stages of calcification, initial, growth and terminal, with its highest concentration being at the growth phase (Gautron *et al.*, 1997). OC-17 (17 kDa) is synthesised in the tubular gland cells of the shell gland and is not produced in other tissues (Hincke *et al.*, 1995). OC-17 is 142 amino acids in length and contains a single C-type lectin-like domain also known as a calcium-dependent carbohydrate recognition domain. Recent work by Reyes-Grajeda *et al.* (2004) determined the three-dimensional crystal structure of monomeric ovocleidin-17 by X-ray diffraction (Figure 1.13); this will lead to a better understanding of the biological behaviour of this protein and other structurally related biomolecules in calcification mechanisms of the eggshell. OC-17 is a phosphoprotein with two phosphorylated serines (Mann and Siedler, 1999), there is also a minor form with a higher molecular weight (23 kDa). The latter is a glycosylated protein with identical sequence but has one phosphorylated serine, and has been named ovocleidin-23 (Mann, 1999). The exact roles of these different forms in the eggshell are not known, but may have separate functions since ovocleidin is alternatively modified (Mann, 1999).

Ovocleidin-116 (OC-116) (116 kDa) (Hincke *et al.*, 1999) is abundant in the uterine fluid during the growth phase and is found in the palisade layer. The granular cells of the surface epithelium of the uterus are responsible for its release. The N-terminal sequence corresponds to a core protein, eggshell dermatan sulphate proteoglycan (ovoglycan) (Carrino *et al.*, 1997). OC-116 contains two N-glycosylation sites and two disulfide bonds (Mann *et al.*, 2002). The

N-glycan structures of this eggshell specific protein have also been further investigated (Nimtz *et al.*, 2004).

Ovocalyxin-32 is found in the uterine fluid during the growth phase but is mainly present during the terminal phase. It is localised in the uterus (shell gland pouch) and red isthmus (tubular shell gland) regions of the oviduct and is known through immunocytochemistry to be secreted by the surface epithelial cells of the uterus (Gautron *et al.*, 2001b). Within the eggshell it is found in the outer palisade layer, the vertical crystal layer and the cuticle and has been observed to be in both the extramineral and intramineral protein extracts. Ovocalyxin-32 levels increase at the termination phase and as a result are likely to be associated with the processes involved in the cessation of calcification.

Ovocalyxin-36 is expressed in the uterine tissue and is found to be up-regulated after the egg enters the uterus or shell gland pouch, so it may be involved in the regulation of eggshell formation (Nys *et al.*, 2004). An additional eggshell and uterine fluid protein has been recently identified and named ovocalyxin-25. It is found in the uterus (shell gland pouch) where mineralisation takes place and in the red isthmus (tubular shell gland) where calcification is initiated (Nys *et al.*, 2004).

1.5.4.3 Ubiquitous Proteins

These proteins are found not only in the eggshell but are also present in other tissues. For example, osteopontin is a phosphorylated glycoprotein that has been identified in the hen eggshell. The osteopontin gene expression occurs in embryonic skeletal tissue and also in adult tissues, normal and transformed bone cells and in some bone marrow cells; this protein has also been found in the kidney (Lavelin *et al.*, 2000). Osteopontin found in the chicken

has 65 % homology at the nucleotide level and 35 % homology in the protein sequence to mammalian osteopontin (Castagnola *et al.*, 1991). In the oviduct, osteopontin has been detected only in the shell gland (Pines *et al.*, 1995), the main site of calcification, and is therefore likely to be involved in eggshell formation. It is localised in the core of the non-mineralised eggshell membrane, in the base of the mammillae and in the outermost part of the palisade layer (Fernandez *et al.*, 2003).

Clusterin, a secretory glycoprotein that has also been found in the eggshell matrix, is a disulfide-bonded heterodimer (Mann *et al.*, 2003). The molecular weight of clusterin is 70 kDa; however, under reducing conditions (10 mM dithiothreitol and 0.5 % 2-mercaptoethanol) the molecular weight is decreased to approximately 35 kDa (Mann *et al.*, 2003). It is distributed in the mammillary and palisade layers. These authors suggest that the function of clusterin could be to prevent premature aggregation and precipitation of eggshell matrix components before and during their assembly into the rigid protein scaffold which is necessary for ordered mineralisation. Therefore, clusterin could act as a chaperone protein during eggshell formation.

1.5.4.4 Identified Eggshell Macromolecules

The glycosaminoglycans dermatan sulphate and keratan sulphate have been localised in the eggshell (Arias *et al.*, 1992; Carrino *et al.*, 1997). Keratan sulphate proteoglycan is secreted in the isthmus by the isthmus gland cells (Fernandez *et al.*, 2001) which occurs when the mammillae are forming and thus could play a role in the initial stages of eggshell formation. Dermatan sulphate is secreted during the active growth phase and is found throughout the palisade layer, this is in association with the localisation and regulation of its core protein, ovocleidin-116 (Hincke *et al.*, 1999).

1.5.5 Quantification of Eggshell Matrix Proteins

Panheleux *et al.* (2000) developed enzyme-linked immunosorbent assays (ELISA) to extract and quantify three eggshell matrix proteins (ovocleidin-17, ovalbumin, and ovotransferrin) in eggshells from young and old hens. According to these authors, the concentration of each of the three proteins analysed was increased in the weaker eggs (determined by their breaking strength) from older hens (58 weeks old); however, the overall protein content was unchanged. These experiments allow for the relationship between proteins and eggshell defects to be investigated further and could be used as a promising tool for analysing the origin of these defects. Therefore, ELISA tests can be used to quantify the proteins in eggs of differing quality but the effect that each individual protein has on eggshell formation is still relatively unknown.

1.6 *In Vitro* Crystallisation Studies

In vitro crystallisation of supersaturated concentration of calcium carbonate can result in ordered structures of the crystal aggregates being formed (Addadi and Weiner, 1992). *In vitro* crystal growth experiments can help in understanding the relationship between proteins and inorganics, and the effects that the presence of proteins have on calcite crystal growth and formation. The *in vitro* measurement of the rate of calcium carbonate crystallisation in the presence of uterine fluid and eggshell extract can be used to study the role played by individual matrix proteins in mineralisation. The duration of precipitation of calcium carbonate from a medium of sodium bicarbonate and calcium chloride in water can be compared to that in which uterine fluid or eggshell extracts are present. Gautron *et al.* (1996) reported that the addition of soluble eggshell matrix delayed calcium carbonate formation. The experimental procedure that the authors followed and modified was that given in Wheeler *et al.* (1981). Water or eggshell extracts were added to 40 mM bicarbonate

solution in a glass vial and 10 mM calcium chloride was added to start the reaction. The pH was monitored and a decrease in the pH by one unit was used as an indication of the duration of precipitation. The same experimental procedure was used by Gautron *et al.* (1997). The oviducal fluid collected during the terminal phase or the dialysed oviducal fluid, irrespective of the stage of collection, also delays the rate of calcium carbonate precipitation (Gautron *et al.*, 1997). This effect is not apparent when the ultrafiltrate (ultrafiltration through a membrane with a 5 kDa molecular weight cut off) of the oviducal fluid had been introduced, thus confirming the involvement of organic macromolecules.

Dominguez-Vera *et al.* (2000) formed calcium carbonate crystals via the sitting drop technique in the presence of oviducal fluid that had been collected at the initial, rapid growth and terminal phases of development. The authors reported that the morphology of the resultant crystals was altered depending on the stage of eggshell formation at which the oviducal fluid was taken. The morphology of the control crystals was rhombohedral. The oviducal fluid collected at the initial phase (6–9 hours after ovulation) facilitated the formation of twinned (two interwoven crystals that are mirror images of one another) calcite crystals, although the crystals still showed rhombohedral faces with some rounded corners. Oviducal fluid collected at the growth phase caused crystals to form which had rhombohedral faces although the corners became rough, and some of the rhombohedral faces became curved. The same morphological changes were seen with the presence of uterine fluid collected at the terminal phase. These results indicate that oviducal fluid components are involved in the growth process.

A study by Hernández-Hernández *et al.* (2003) investigated calcium carbonate formation in the presence of proteins (lysozyme, myoglobin, ribonuclease, α-lactalbumin). At high

protein concentrations, calcium carbonate formation was inhibited; at lower protein concentrations, crystal formation increased. They concluded that the proteins were binding to the crystal growth sites, resulting in the inhibition of calcium carbonate formation. A modification of this technique was used to study the effect of both dermatan sulphate and carbonic anhydrase on *in vitro* calcium carbonate formation upon eggshell membrane with "mammillae" (masses of organic material) that had been recently formed (Fernandez *et al.*, 2004).

The glycosaminoglycan dermatan sulphate has been detected in eggshell (Carrino *et al.*, 1997), and is found throughout the palisade layer, where it is deposited during the growth phase. Carbonic anhydrases catalyse the reversible reaction between carbon dioxide hydration and bicarbonate dehydration. These authors found that carbonic anhydrase (10 μg/ml) increased the rate of calcium carbonate crystal growth, which resulted in early nucleation and growth, and induced calcite crystal aggregation. Furthermore, dermatan sulphate (64 μg/ml) was found to modify crystal morphology, where large calcium carbonate crystal aggregates with a columnar morphology were formed.

1.7 Nanostructure, X-ray Scattering Techniques and the Aims of this Thesis

Studies have shown that eggshell formation is regulated by a precise spatio-temporal arrangement of sequentially deposited macromolecules (Fernandez *et al.*, 1997) and the precise ultrastructural localisation of these macromolecules (Fernandez *et al.*, 2001). Information concerning the complex relationship between the organic and inorganic components of the eggshell is therefore required in order to appreciate and understand the overall structural integrity and mechanical performance of the complex biomineral. The mechanical properties of other biomaterials are known to be dependent on their structural

organisation at all length scales, where the structure at each level has been optimised (Aizenberg *et al.*, 2005). For eggshells, ultrastructural studies using scanning electron microscopy have revealed that there are structurally distinct regions at the micron length scale (Solomon, 1991). There is also evidence of a relationship between the eggshell microstructure and its mechanical performance (Rodriguez-Navarro *et al.*, 2002). To date, however, there has been no published data regarding the nanostructure or nanotextural organisation of eggshells.

X-ray scattering techniques, primarily small angle X-ray scattering (SAXS), are ideal for investigating biomaterials at the nanometer length scale. SAXS, for example, has been shown to provide valuable structural information about the crystallite thickness, shape and orientation of bone (Matsushima *et al.*, 1981; 1982; 1984; Fratzl *et al.*, 1991; 1992; 1996a; 1996b; Wess *et al.*, 2000; 2001a; 2001b). Microfocus SAXS, which makes use of more highly focused X-ray beams (smallest being 300 nm) with greater point to point resolution, has also been used to analyse bone (Hiller and Wess, 2006), parchment (Kennedy *et al.*, 2004), wood (Paris *et al.*, 2000), calcified avian tendons (Gupta *et al.*, 2003), starch (Waigh *et al.*, 1997; Chanzy *et al.*, 2006) and polymers (Lorenz-Haas *et al.*, 2003). This technique allows for more precise details of biominerals to be obtained at the nanometer length scale.

In this thesis, it is hypothesised that the structure of the eggshell at the nanometer length scale is optimised in such a way that it promotes the functional properties of the resulting composite at both the microstructural and ultrastructural levels. The main aim of this thesis was therefore to conduct a detailed investigation of the eggshell's nanostructural features using SAXS. In Chapter 2, the theory, instrumentation, data collection and data analysis methods behind this technology is described. Microfocus SAXS is then used to investigate

and compare the nanostructural features of eggshells, which were visually classified as being normal or extremely abnormal in terms of their shell quality in Chapter 3. In Chapter 4, SAXS and X-ray diffraction (XRD) techniques are used to investigate the nanostructural properties of eggshells, which have been expelled at different stages of gestation. This study was specifically designed to see if the nanostructure of the eggshell changes in relation to the initial, rapid and terminal phases of shell formation. If nanostructural changes do occur as the egg is formed then this could result from the temporal and spatial deposition of the different components of the eggshell matrix. The nanostructures of eggshells from young and aged hens with different mechanical strengths are investigated in Chapter 5. According to the literature, the ultrastructural and microstructural properties of eggs from aged hens are significantly different than those from younger hens, resulting in poorer eggshell strength. It was therefore of interest to determine if similar changes occur at the nanostructural level. In order to further understand the initial processes of nucleation and subsequent crystal growth, which occur as the eggshell forms in the shell gland, a series of *in vitro* crystallisation experiments were also carried out, the result of which are presented in Chapter 6. In these experiments, the initial nucleation events of calcium carbonate were investigated for the first time using SAXS either with or without the presence of proteins. In the final chapter (Chapter 7), the main conclusions from this thesis are discussed in relation to the effect that changes in eggshell nanostructure could have on the structure and function of this highly complex biomineralised structure. Possible future considerations are also highlighted.

Chapter 2

Introduction to X-ray Scattering and Instrumentation

2.1 Introduction

X-rays are electromagnetic waves with dimensions in the order of a tenth of a nanometer (10^{-9} m) and were discovered in 1895 by G.C. Röntgen; they are of the same nature as visible light but with a shorter wavelength. The wavelength (λ) of visible light is in the order of 6.0×10^{-7} m, whereas X-rays used in diffraction are approximately $0.2 \times 10^{-11} - 2.5 \times 10^{-10}$ m (Cullity, 1978). X-rays are used to investigate the structure of matter such as gases, liquids, amorphous solids and crystalline solids at the molecular and atomic level. Techniques using X-rays include diffraction, absorption spectroscopy, small-angle scattering and fluorescence spectroscopy. This chapter provides a description of aspects of X-ray scattering and its application in examining biological materials. The use of synchrotron radiation sources to study eggshell material is also discussed in this chapter.

2.2 Coherent and Incoherent Scattering

When the incoming incident X-ray beam encounters an atom, two scattering processes occur referred to as coherent and incoherent scattering. Electrons that are tightly bound start oscillating and scatter X-rays with the same wavelength as the incident beam; this is coherent scattering. The scattered X-rays have the same frequency and wavelength as the incident wavelength, since there is a relationship between the phase of the scattered X-rays and that of the incident X-rays. The scattered X-rays from several different scattering centres are either cancelled out or are reinforced, where the latter produces diffraction of X-rays (Cullity, 1978).

Electrons that are loosely bound scatter part of the incident beam and increase the wavelength slightly, this is known as incoherent scattering or Compton scattering, named after A.H. Compton in 1923 who discovered this effect. Considering the incoming beam as a flow of photons and not as a wave motion, when incoming photons collide with an electron that is loosely bound some of the energy from the incoming photon is transferred to provide kinetic energy for the electron. There is an increase in the wavelength of the scattered beam compared to the incoming beam, and the extent of the increase is dependent on the scattering angle (Cullity, 1978). At small angles, incoherent scattering is weak therefore analysis is confined to coherent scattering (Glatter and Kratky, 1982).

For the analysis of the eggshell, only coherent scattering is taken into account within this thesis as the majority of the analysis was by small angle X-ray scattering.

2.3 Crystal Lattices

A crystal is a solid, which consists of atoms that have a periodic arrangement in three dimensions. Gases and liquids do not have this periodicity with their atomic arrangements; therefore, they differ from crystals. With regard to solids, not all are crystalline; for example, amorphous solids such as glass do not have any regular arrangement of atoms; these solids may have short-range order but no long-range order. Therefore, amorphous solids and liquids have no fundamental difference with regard to their regular atomic arrangement (Cullity, 1978). An imaginary set of points in space with a fixed relation to the atoms of the crystal can be thought of as a framework that the crystal is built on. Space can be separated into three parallel and equidistant planes. A set of cells (each identical in size, shape and orientation) are produced in this separation of space. Lines allow the planes to intersect with one another and the lines intersect a set of points. The cells of the lattice are

the same and are referred to as a unit cell, three vectors describe the unit cell **(a,b,c)** and also their lengths (a,b,c) and angles (α,β,γ). A lattice of points and a unit cell are shown in Figure 2.1.

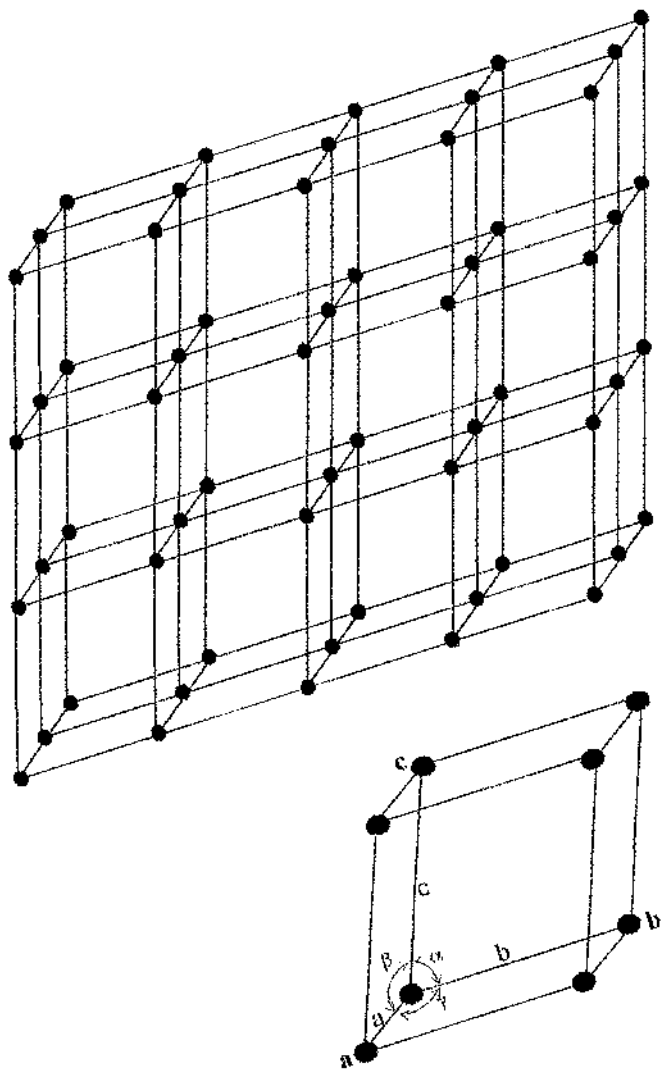

Figure 2.1 A lattice of points and a unit cell. The image at the top is of a lattice of points, where each of the cells of the lattice are identical to the others. An enlarged unit cell from the lattice is shown below, described by vectors (a,b,c) and their lengths (a,b,c) and angles (α,β,γ).

The planes in a lattice can be identified based on their orientation in the unit cell using Miller indices (h,k,l), which are the reciprocals of the lattice planes. If the axial lengths are a,b,c and the plane makes fractional intercepts at $1/h$, $1/k$, $1/l$ with the axes, the actual intercepts of the planes are a/h, b/k, c/l.

2.4 Bragg's Law

Bragg's Law explains the interference pattern of X-rays scattered by crystals. The distance travelled by the incident X-rays is dependent on the separation of the layers of atoms within the crystal and also the incidence angle. The incident X-rays are required to have travelled a whole number of waves after penetrating and whilst inside the sample for it to be in phase with the reflected X-rays.

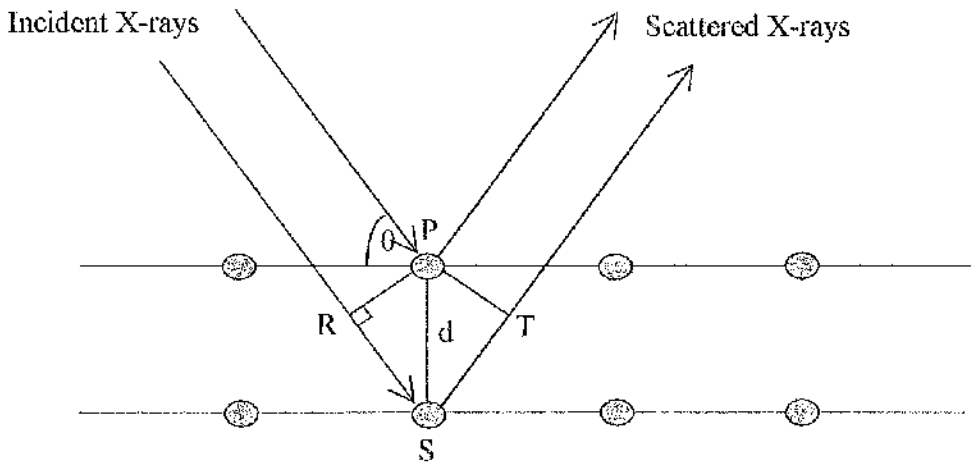

Figure 2.2 Schematic diagram representing Bragg's Law, which explains the diffraction of X-rays from crystals.

The reflection of X-rays from successive crystal planes and their interference can be described by Bragg's Law (Figure 2.2), where the incident X-rays through S travel a distance of RS + ST more than X-rays through P. The distance between RS and ST is $d\sin\theta$, where d is the interplanar distance in the crystal and θ is the incidence angle and the angle of reflection. Constructive interference occurs when $RS + ST = 2d\sin\theta = \lambda$, which is Bragg's Law, where λ is the wavelength of the incident X-ray beam. There has to be an integer number of waves for constructive interference to arise. When the incident X-rays and the reflected X-rays are in phase there will be a diffraction signal collected on the detector from this reflection. If the X-rays are not in phase there will be no signal or it will be very weak.

2.5 Fourier Series and Fourier Transform

This section provides a brief summary about Fourier series and Fourier transforms, a more in depth description is given by Rhodes (2000).

2.5.1 Periodic Functions

Periodic functions can be used to describe waves. The amplitude F (half of its height from peak to valley), frequency h (number of wavelengths per radian) and phase α (with respect to the origin, it is the position of the wave in radians) can describe sine and cosine waves. The wave equations are shown as equations 2.1 and 2.2. These equations are one-dimensional since they represent a numerical value at all the points along an axis, in this case the x-axis.

$$f(x) = F\cos 2\pi(hx + \alpha) \tag{2.1}$$

$$f(x) = F\sin 2\pi(hx + \alpha) \tag{2.2}$$

At any horizontal position x, $f(x)$ is the vertical height of the wave. x is measured in wavelengths, so when $x = 1$ this indicates a single complete wavelength or a single complete repeat of the periodic function from the origin.

2.5.2 Fourier Series

Complex periodic functions can be described using simple sine and cosine functions, where the wavelengths of these functions are integrals of the wavelength of the complex function. Each of the sine and cosine functions are Fourier terms and the sum of these is a Fourier series. In order to compute the Fourier terms that describe a complex wave, Fourier synthesis is used.

Diffracted X-rays are collected on a detector; a diffracted X-ray that has produced a reflection as part of the diffraction pattern can be described as the sum of the contributions of all scatterers in a unit cell, where the structure factor equation is used for the sum. The computed sum for a given reflection with indices *hkl* is F_{hkl}. Superposition of individual waves resulting from diffraction by an individual atom is used to create a wave, the structure factor.

X-rays are diffracted from electrons within the molecules in a sample and the diffraction pattern provides information about the distribution of electrons or electron density of the molecules. The molecules within a crystal are arranged in an ordered manner; therefore, the electron density can be described mathematically by a periodic function. The electron density $\rho(x,y,z)$ is a three-dimensional periodic function, where ρ is the electron density at all positions x, y and z in a unit cell. It describes the shape of all the molecules and the surface features in a unit cell. The electron density can be expressed and described as a Fourier

series. A Fourier series describing the reflections can be converted to a Fourier series describing the electron density by Fourier transform. A Fourier series describes the electron density where each term is a structure factor. The unit cell can be divided into n elements, where the average electron density in volume element m, is ρ_m. Equation 2.3 is a structure factor equation describing a diffracted X-ray from a unit cell. In the unit cell, each volume element contributes to each reflection in a diffraction pattern.

$$F_{hkl} = f(\rho_1) + f(\rho_2) + \ldots + f(\rho_m) + \ldots f(\rho_n) \tag{2.3}$$

A large number of equations are produced from each reflection and they describe reflections in terms of the electron density.

2.5.2.1 One-Dimensional Waves

A Fourier series of n terms is shown in equation 2.4, using cosine as an example.

$$f(x) = \sum_{h=0}^{n} F_h \cos 2\pi(hx + \alpha_h) \tag{2.4}$$

In order to obtain the complete information about the sample and the objects that scattered the X-rays, the amplitude, frequency and phase must be known. From a diffraction pattern the phase α is not known; therefore, the α_h term has to be removed from the Fourier series. As the phase cannot be obtained from the diffraction pattern this causes a problem (the phase problem). The phase problem can be overcome by several techniques including isomorphous replacement, where heavy atoms (large atomic number) are introduced to a structure binding specifically to each molecule in the unit cell, anomalous scattering and

molecular replacement. More information regarding the phase problem can be found in Stout and Jensen (1968), Glusker and Trueblood (1972), Rhodes (2000).

A basic waveform is $[\cos 2\pi(hx) + i\sin 2\pi(hx)]$ and a complex number is produced from the combination of the sine and cosine waveforms. The general form is $a + ib$, where i is an imaginary number $(-1)^{1/2}$. Shown in equation 2.5 is a Fourier series, which is the sum of n Fourier terms, one for each integral value of h starting at zero and finishing with n. Each of the terms in the sum is a wave with an amplitude F_h, a frequency h and phase α.

$$f(x) = \sum_{h=0}^{n} F_h[\cos 2\pi(hx) + i\sin 2\pi(hx)] \tag{2.5}$$

Equation 2.6 shows the complex number as an exponential.

$$\cos\theta + i\sin\theta = e^{i\theta} \tag{2.6}$$

$\theta = 2\pi(hx)$; therefore, the Fourier series becomes equation 2.7.

$$f(x) = \sum_{h=0}^{n} F_h e^{2\pi i(hx)} \tag{2.7}$$

2.5.2.2 Three-Dimensional Waves

A Fourier series of a three-dimensional wave $f(x,y,z)$ is shown in equation 2.8.

$$f(x,y,z) = \sum_{h}\sum_{k}\sum_{l} F_{hkl} e^{2\pi i(hx+ky+lz)} \tag{2.8}$$

The frequency in the x-direction is h, in the y-direction it is k and in the z-direction it is l. This adds up all the terms for the possible sets of integers h,k,l.

2.5.3 Fourier Transforms

Fourier transforms describe the mathematical relationship between an object and its diffraction pattern (Rhodes, 2000). The diffraction pattern is also the Fourier transform of the object or a group of objects. Fourier transform is a mathematical operation that solves the structure factor equations for the desired function $\rho(x,y,z)$. From a diffraction pattern, the intensity of a reflection gives the amplitude of one Fourier term in the series that describes $\rho(x,y,z)$. The position of the reflection hkl gives the frequency. The Fourier transform of a function $f(x)$ is demonstrated below (equation 2.9).

$$F(h) = \int_{-\infty}^{+\infty} f(x) e^{2\pi i(hx)} dx \tag{2.9}$$

The units of h are the reciprocals of the units of x. This equation is reversible, where $F(h)$ is the transform of $f(x)$ and vice-versa. Fourier transforms can be used to obtain information about real space ($f(x,y,z)$) from reciprocal space ($F(h,k,l)$) information. For any function $f(x,y,z)$ in three dimensions there is a function $F(h,k,l)$, displayed in equation 2.10.

$$F(h,k,l) = \int_x \int_y \int_z f(x,y,z)\, e^{2\pi i(lx+ky+lz)} dx dy dz \tag{2.10}$$

2.6 X-ray Diffraction and Scattering

Diffraction is a scattering phenomenon as incoming X-rays are scattered by atoms in all directions. In some of these directions, the scattered X-rays will be in phase; therefore, reinforcing each other and forming diffracted beams (Cullity, 1978). Therefore, diffraction is the restriction of scattering to specific vectors due to correlated objects. The ability of samples to scatter or diffract depends mostly on the ordering of that material. Diffraction results from samples with a repeating structure or regular packing, and small angle X-ray scattering results from the particles or electron density changes within the sample material, which provides structural information about the material being analysed. Electron density fluctuations within the sample material can be investigated using X-rays since they interact with electrons and scatter producing a characteristic scattering pattern that provides structural information. Scattering is the deviation of X-rays from their incident path, which is caused by uncorrelated objects. Length scales in the submicroscopic scale to the Ångstrom level contribute to the scattering data, which relates to information about the molecular and atomic organisation within the sample. The conceptual differences between SAXS and XRD are shown in Figure 2.3. SAXS and XRD differ in the location of the scattering of interest, where SAXS is typically at small angles in the vicinity of the primary beam and XRD is at high angles.

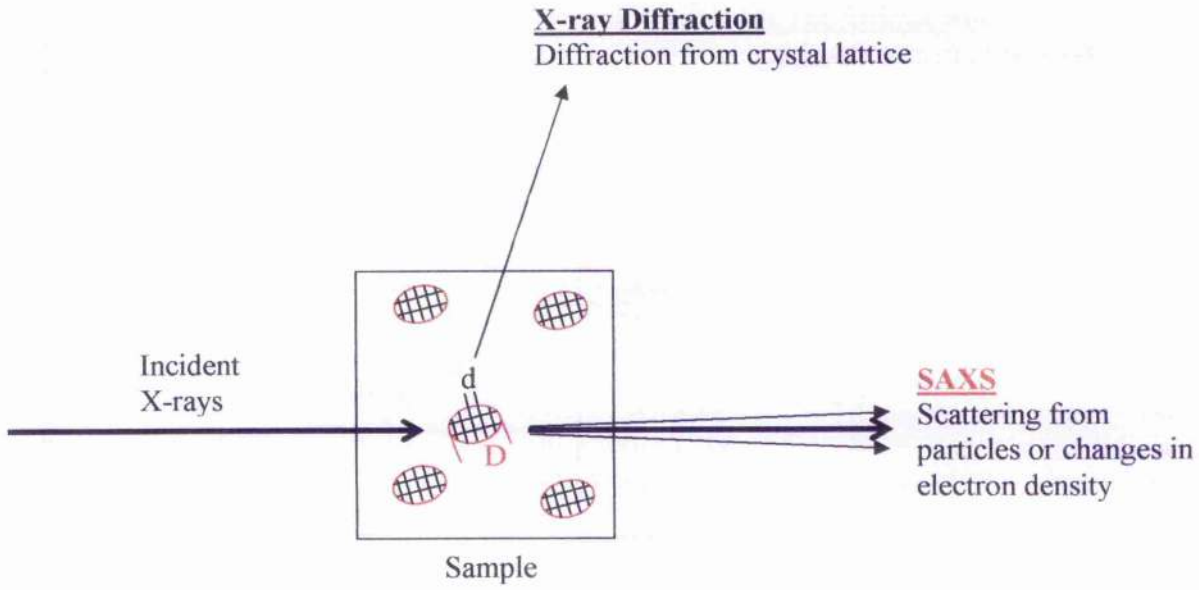

Figure 2.3 Schematic showing the principles of X-ray diffraction and SAXS. Scattering at small angles results from particles (D) shown in red or electron density changes within the sample. Diffraction results from the repeating structure or regular packing within the sample, such as from the crystal lattice (d) shown in black. X-ray diffraction occurs at high angles.

2.6.1 X-ray Diffraction

Peaks of X-ray intensity are observed at certain deflected angles, as a result of the specific interactions between the X-rays and the electrons within the sample. If the sample has no regular spatial relationship within it, this leads to no scattering signal accumulation from each of the individual scatterers; therefore, there is no peak present only a scattering signal that occurs over a broad range of scattering angles. The peak position, intensity and angular distribution from diffraction patterns provide structural information about the sample.

X-ray diffraction patterns from crystalline powders provide information on the sample from the position and intensity of the resulting concentric rings. Information regarding crystallite size can be obtained from the X-ray diffraction pattern of a crystalline powder by measuring the full width at half maximum (FWHM) of Bragg peaks. When crystallites are less than ~100 nm in size, there is found to be measurable broadening in the X-ray diffraction lines. A full description on analysing the broadening of powder lines is given by Lipson and Steeple, (1970). By measuring the FWHM of the diffraction peaks, information on coherent regions of crystallinity can be found. These regions may correspond to the actual size of the crystals, or act as a measure of coherent regions in the larger crystals. As an alternative to measuring the FWHM of individual peaks, all the peaks in a diffraction profile can be fitted as a whole using the Rietveld method (Rietveld, 1967; 1969). The Rietveld method is carried out using least-squares refinements until the best fit is obtained between the entire observed powder diffraction pattern taken as a whole and the entire calculated pattern based on simultaneously refined models for the crystal structures. X-ray diffraction line broadening can be used for investigating microstructural characteristics such as size and strain due to dislocations within a sample, and also can determine the degree of crystal perfection or atomic ordering. In comparison, the broadening of the primary beam with SAXS is insensitive to the strain and

imperfections of the crystallinity; therefore, SAXS analysis depends on the outer dimensions of the crystals (Fratzl *et al.*, 1991).

2.6.2 Small Angle X-ray Scattering

Small angle X-ray scattering is used to determine the structure and organisation of particles in systems. Examples of structures that can be investigated using SAXS are colloids, polymers, micelles, and voids or pores in solids. At low angles, scattering results from changes in the electron density of the matter, such as the interfaces between molecules. X-rays are scattered by electrons; therefore, when there are electron density inhomogeneities within the sample then small angle X-ray scattering occurs. SAXS experiments are carried out by passing an X-ray beam, which is well collimated and has a specific wavelength λ through the sample, and measuring the scattering intensity variation I(q) as a function of the scattering angle θ (Cotton, 1991). SAXS experiments measure the scattering intensity I(q) at low angles, in order to investigate large scale structures from about 10 Å up to several thousand Å (Glatter and Kratky, 1982). A more in depth description about small angle X-ray scattering is provided in Guinier & Fournet (1955) and Glatter & Kratky (1982).

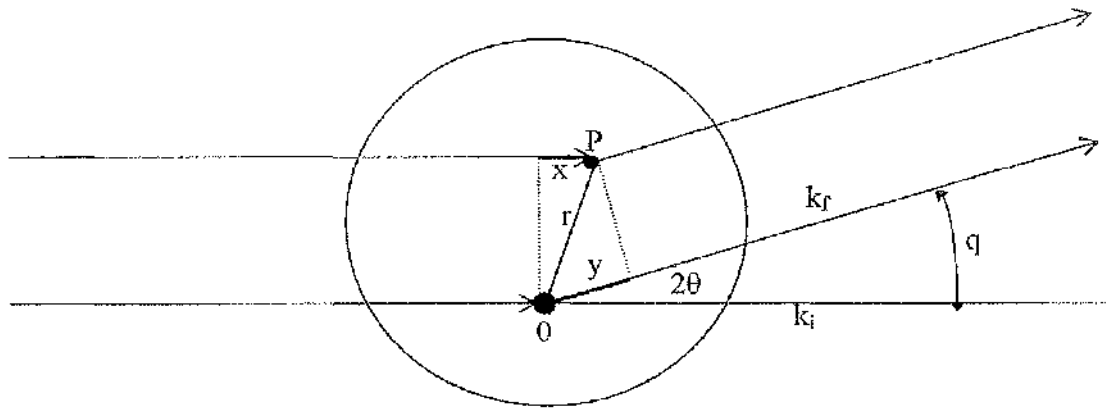

Figure 2.4 Schematic of a typical scattering event between two points P and O.

From the coherently scattered waves the scattering amplitudes need to be added according to their amplitude and relative phase φ. The relative locations of the scattering centres influence the phase difference. The phase φ is $2\pi/\lambda$ times the difference between an arbitrary reference wave and the optical path length of the wavelength. The incident wave vector k_i and the scattered wave vector k_f are in phase since there is no energy transfer and the scattering angle between them is 2θ. The path length difference is $x - y = rk_i - rk_f = -r(k_f - k_i)$, between the X-rays through a point P and an arbitrary origin O (i.e. between the two paths x and y) (Figure 2.4). The phase is $\varphi = -qr$ if the scattering vector is defined as $q = (2\pi/\lambda)(k_f - k_i)$. This scattering vector bisects the angle between the incident and scattered beam and has length $q = \frac{4\pi}{\lambda}\sin\theta$ (Glatter, 1991).

The amplitude of the scattering intensity I(q) is the Fourier transform of g(r), the correlation function of the electronic density ρ(r), which relates to the probability of finding a scattering

object in the sample at position *a* if there is another one at position *b* separated by distance r. Spatial correlations within a sample are revealed by elastic scattering experiments, where there is no energy change and therefore the scattered and incident wavelength have the same frequency. The shape and distribution of the scattering at low angles provides information such as size, shape, arrangement and internal porosity of the scattering particles. The information provided in the scattering intensity can be analysed by integrating around the two-dimensional scattering pattern at defined intervals and producing a one-dimensional linear trace. This is shown in Figure 2.5, where A is a two-dimensional SAXS pattern and B is the corresponding one-dimensional linear trace.

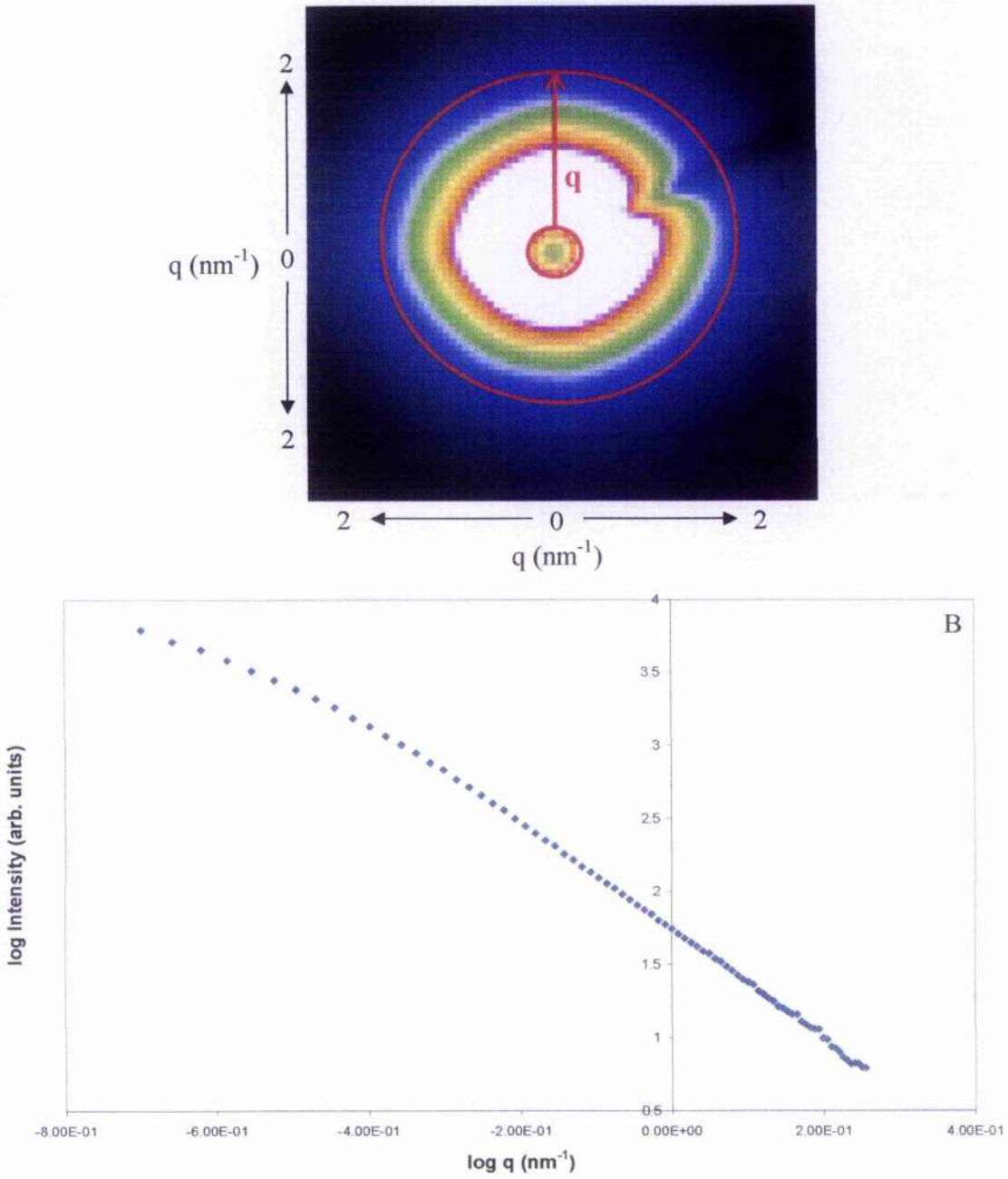

Figure 2.5 SAXS data from a typical powdered eggshell sample obtained at the ESRF, station ID18F. (A) A SAXS pattern showing the scattering distribution. 1 pixel corresponds to 0.02 nm^{-1} in q. Shape, size, orientation and arrangement of the scattering particles can be obtained from the scattering distribution. The colours on the image are an indication of intensity, where the lighter the colour the greater the intensity. The shading at the top right of the image is from the backstop. (B) The linear trace below is produced from the integration of the two-dimensional data between the intervals into a one-dimensional linear trace plotted as log I(q) against log q.

The analysis of a SAXS curve can provide different types of structural information about the material that is being examined depending on the system. The parameters that can be obtained from the specific regions of the scattering curve at different points on the q-axis are shown in Figure 2.6. A SAXS curve is essentially unchanged if the electrons within a particle are shifted by small distances in comparison to the overall dimension of the particle. Therefore, a uniform electron density distribution can be considered when a particle has small inhomogeneities.

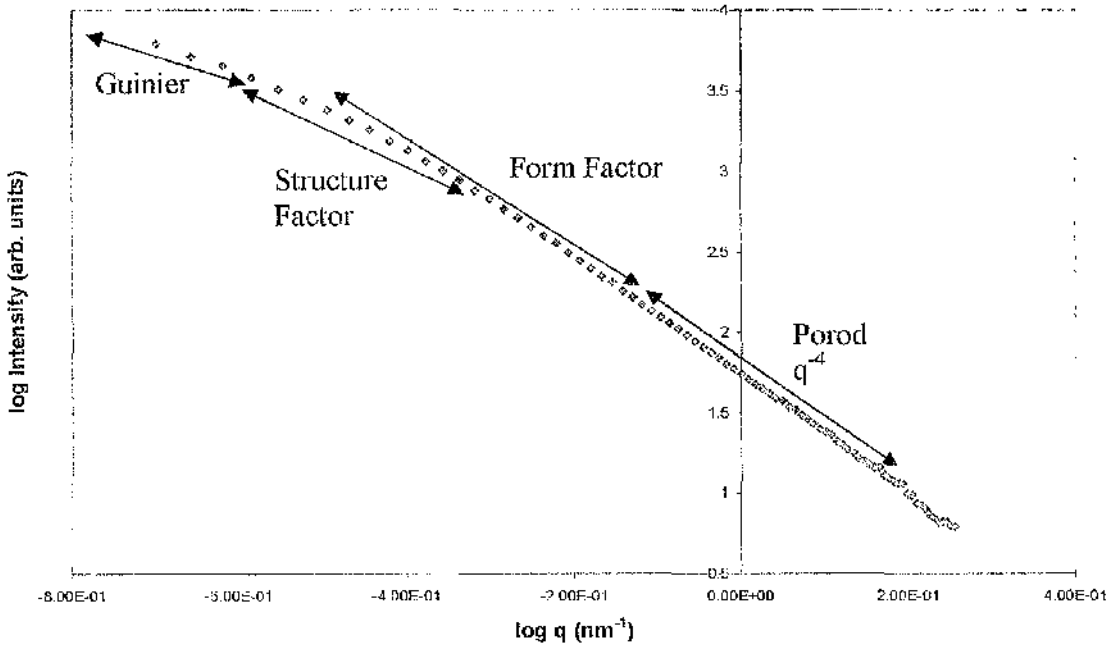

Figure 2.6 An example of a typical scattering curve is represented and indicated at approximate regions on the curve are the parameters that can be extracted from it.

The scattering intensity is composed of the form factor P(q) and the structure factor S(q), $I(q) = P(q) * S(q)$. The particle size and shape (intraparticle) is related to the form factor P(q), and interparticle correlations are related to the structure factor or interference function S(q), which is a function of local order or the potential of interactions between particles. If the scattering particles are independent scattering objects and there are no interparticle interactions, then the form factor can be measured, in the dilute regime. The scattering intensity is directly proportional to the contrast $\Delta\rho$, the volume fraction ϕ, the volume of one particle V_p, and the form factor of a single particle P(q). The structure factor can be obtained from the scattering intensity; however, this information in certain cases cannot be extracted from the intensity. If a peak is present in the scattering curve at low q, its position on the curve is associated with the interference factor. The position at which this peak occurs provides information about the distance between the scattering particles. At low q therefore, the structure factor can be obtained, providing information about the interactions between particles in a system. The form factor can be measured at intermediate q values as shown in Figure 2.6, providing information about the size and shape of the particles within the system. At high q, the scattering data provides information about the interfaces within the system, which can be described by Porod's Law.

2.6.2.1 Porod's Law

Porod's Law can provide information about average particle size and void size. Within the sample medium, spatial variations and density fluctuations contribute to the scattering intensity. Variations in the density are found at interfaces within many colloidal systems (Auvray and Auroy, 1991). If the surrounding solvent and the individual particles have a sharp interface, then the scattering curve will follow Porod's Law, which predicts a decay in the scattering intensity of q^{-4}, at lower q values. If the particle has pores within it and if

sharp interfaces occur, then at high q there will be a second Porod region. If there are different particles with their separate characteristic scales then it is possible to observe two Porod regions within the scattering curve. A measurement of the surface area of the scattering domains can be obtained by Porod's Law. At the high q region, the scattering intensity follows an asymptotic law if there are sharp interfaces between two media. The Porod constant (P) can be determined from the scattering intensity, where B is the background, shown in equation 2.11.

$$I(q)=Pq^{-4}+B \tag{2.11}$$

The Porod constant is the y-intercept (Figure 2.7) and the background is the slope can both be obtained from the scattering curve when it is plotted as $I(q)*q^4$ against q^4 (Thomas *et al.*, 1998). In order to obtain the Porod constant the most appropriate q-range has to be chosen, since the Porod constant is an important parameter in the calculation of the surface area.

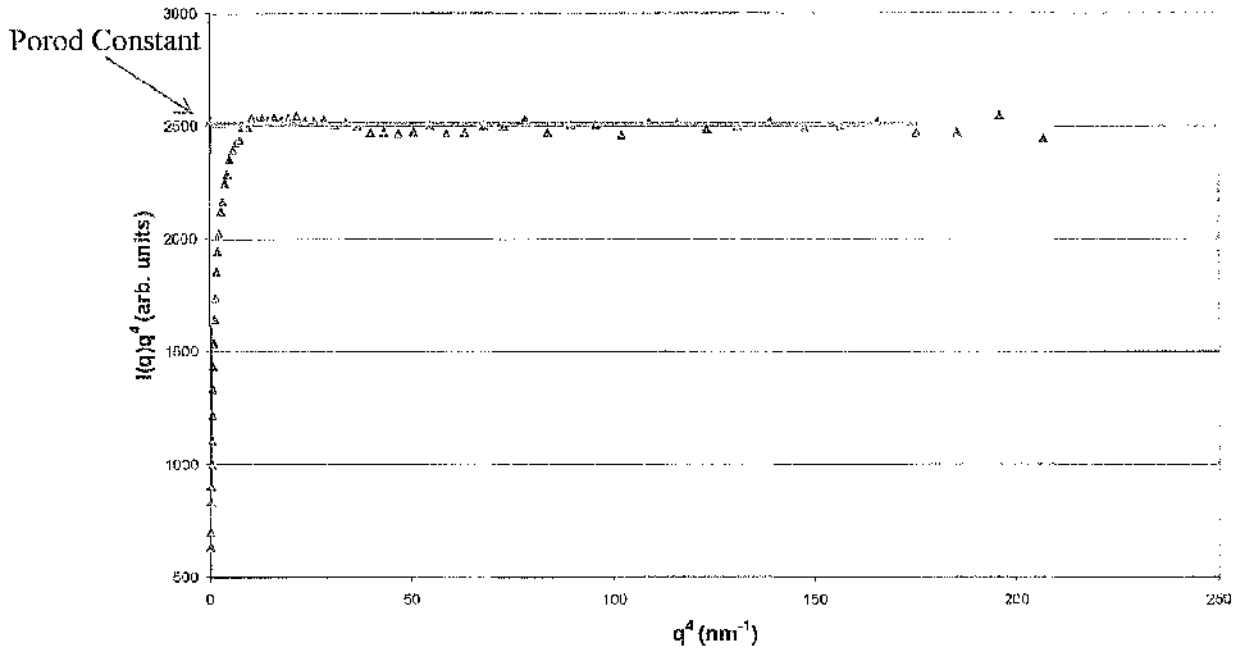

Figure 2.7 Scattering curve plotted as a Porod plot where the y-intercept is shown as the red line is the Porod constant.

The surface area of the scattering particles is directly proportional to Porod's constant, where the asymptotic behaviour at high q (where $q \rightarrow \infty$) of the scattering intensity I(q) is shown in Porod's Law (equation 2.12).

$$I(q) = I_e 2\pi\rho^2 S/q^4 \qquad (2.12)$$

In equation 2.12, I_e is a constant, ρ is the electron density difference between the scattering particles and the solvent/matrix, and S is the surface area of the interface between the two media. As an example, the Porod region for eggshell material is indicated on Figure 2.8, where the scattering intensity is decaying at a rate inversely proportional to the fourth power of the scattering vector q.

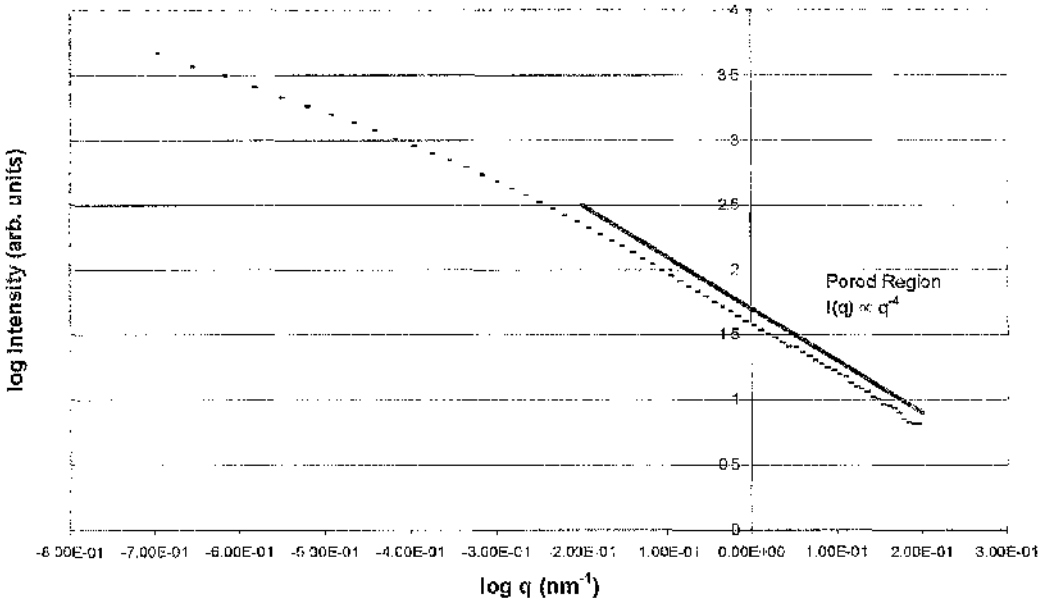

Figure 2.8 Double logarithmic scattering curve obtained from an eggshell sample. The straight line depicts the Porod region, where the decaying intensity is in inverse proportion to the fourth power of the scattering vector q, ($I(q) \propto q^{-4}$).

2.6.2.2 Guinier Approximation

Constructive interference involves the probability that *within* a particle there is a point (A) and another point (B) at a distance of $r = 1/q$ apart. With regards to an isotropic system, this is initially calculated by averaging any starting point within a particle and then averaging any direction for the vector, **r**, leading to a double summation, which is exactly the same as deducing the moment of inertia for a particle. The moment of inertia is the quantity mr^2 of the particle, where m is the mass. Instead of using the mass the electron density within the particle is used, this produces the radius of gyration (R_g) of the particle. The R_g, if there is a distribution of particle sizes and shapes, represents a second moment (the expected value of the square of the deviations of a random variable from the point of origin) of the distribution

of the shape and size about the mean. In order to obtain the R_g, all possible points in the particle that a vector r can have within the particle are averaged initially, and then from an arbitrary point the probability that a randomly directed vector will be within the particle is calculated. A Gaussian distribution cloud produced from the summation of the possible points of the particle can then be used to represent the meaning of this probability p(r), in the vicinity of r = particle size. The volume fraction of the particles squared is represented at low q. When r = 1/q, this is approximately the average particle size of R_g, and can be seen by a decaying exponential function. The average particle size is represented in the R_g. Therefore, the R_g is the root-mean square of distances of all the electrons from their centre of gravity (Glatter and Kratky, 1982).

In a Guinier plot, the ln I(q) vs q^2 is plotted. The square root of the slope of the linear part at low q provides R, where R provides information on the distribution of the scattering objects with respect to the particle centre of mass. A Guinier plot is shown in Figure 2.9, where all the scattering data are shown in Figure 2.9A. The initial points at lower q values are used for the determination of the radius of gyration as shown in Figure 2.9B.

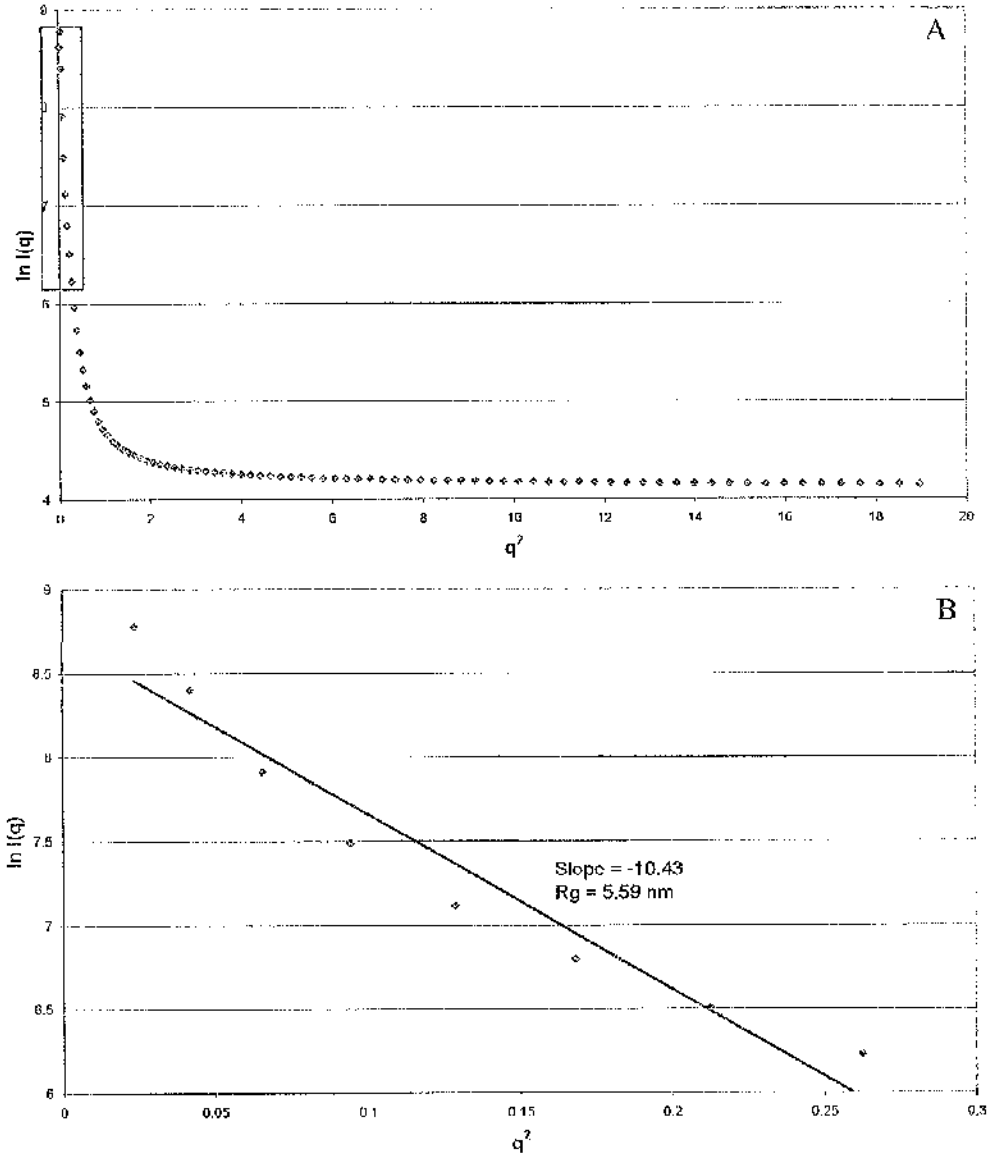

Figure 2.9 (A) A Guinier plot (ln I(q) against q^2) of all the scattering data. The red box contains the initial points that are used to calculate the radius of gyration and only these points are plotted and shown in B. The slope of this portion of the scattering curve is used to calculate the size of the particle.

From the scattering at low q values, the R_g of the particles can be obtained using the Guinier approximation (equation 2.13) (Butter *et al.*, 2005).

$$I(q)=I(q=0)\exp(-q^2 R_g^2/3) \tag{2.13}$$

In the Guinier plot, the data at low q should be a straight line with a slope $R_g^2/3$. With regards to homogenous spheres, the radius (R) of a sphere is related to the radius of gyration by equation 2.14.

$$R_g^2 = 3R^2/5 \tag{2.14}$$

2.7 X-ray Sources

A description of the instrumentation used throughout this work to collect data is given here. A major part of this work involved data collection using the NanoSTAR, a laboratory based X-ray facility at Cardiff University, and also synchrotron radiation sources (SRS) (Daresbury Laboratory and the European Synchrotron Radiation Facility). Here, the theory of synchrotron radiation is discussed, followed by a brief description of each of the beamlines that were used.

2.8 Synchrotron Radiation

Synchrotron radiation was developed in the 1940s, about 50 years after the discovery of X-rays. Synchrotron radiation is now used as a tool in many scientific research fields, such as physics, chemistry, geochemistry and biology. Synchrotron facilities are used to probe the structure of matter and investigate materials at a molecular and atomic level. The term synchrotron radiation is given to radiation that occurs when charged particles are accelerated in an orbit to relativistic velocities and their path is bent by a magnetic field. The radiation is characterised by certain parameters including flux, brilliance and spectral energy range. The flux is the amount of radiation per unit area per unit time and can be specified as photons; therefore, photon flux is the number of photons per unit area per unit time. The properties of synchrotron radiation include high spectral brilliance (brightness), which is the photon flux per unit area per unit solid angle. Synchrotron radiation is highly intense and collimated (most of the waves are in the same direction), and it is emitted with a wide spectrum of energies. Another property of synchrotron radiation is that it is highly polarised, either linearly or circularly. The synchrotron facilities that were used in the work presented in this thesis were the SRS Daresbury Laboratory, in Cheshire, UK, and the European Synchrotron Radiation Facility (ESRF), situated in Grenoble, France. The X-rays at the ESRF are a

thousand billion times brighter than the beams used in X-ray machines within hospitals. For example, at the ESRF, a high brilliance beamline (ID02) uses three undulators to provide a high photon flux with a low divergence.

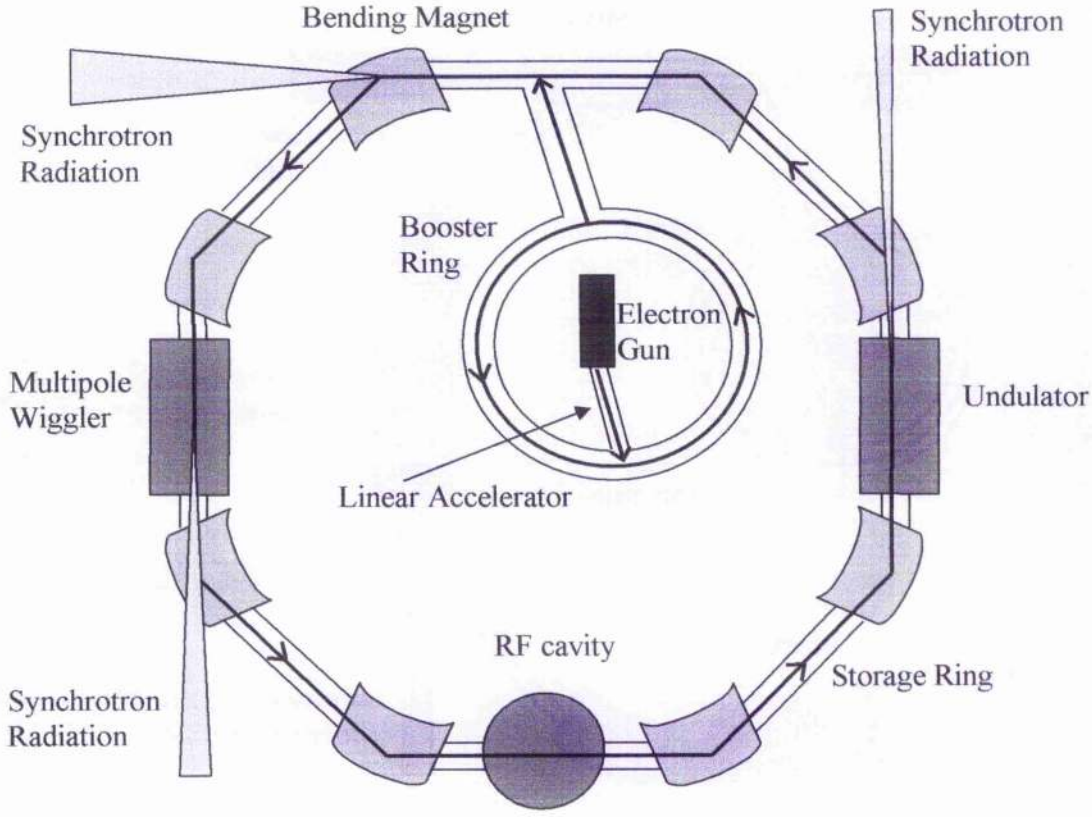

Figure 2.10 Schematic of a simplified layout of a synchrotron radiation facility.

Synchrotron radiation facilities are composed of a pre-injector (a linear accelerator), booster and storage ring (Figure 2.10). Briefly, electrons are emitted by an electron gun, and the pre-injector fires the electrons into the booster where they are accelerated by radio-frequency (RF) fields. Once they have reached their target energy the electrons leave the booster ring and enter the storage ring. When electrons are fired from the electron gun they flow into the klystron. Klystrons (evacuated electron tubes) are microwave amplifiers, where microwave power energises electrons therefore maintaining their energy in the storage ring. A microwave signal intersects the electron beam producing a pulsed beam, which is composed of separate electron bunches. Klystrons also power the RF cavity, which receive RF energy and pass it onto the electrons as they pass through them. Klystrons are required to maintain and restore loss of electron energy. The electrons are accelerated at relativistic velocities (when particles are moving close to the speed of light), which leads to the emission of photons at a tangent to the orbit. Emitted photons with energies ranging from infra-red to X-rays, termed synchrotron radiation, are channelled down beamlines. Whilst in the storage ring, the electrons pass through different types of magnets, including bending magnets, undulators, wigglers and focusing magnets. These devices force the beam of electrons to follow a sinusoidal trajectory, which produces an increase in the intensity of the radiation.

The bending magnets keep the electrons circling around the inside of the storage ring, and the electrons are deflected as they pass through the bending magnets resulting in the emission of synchrotron radiation. An example of a dipole bending magnet is shown in Figure 2.11.

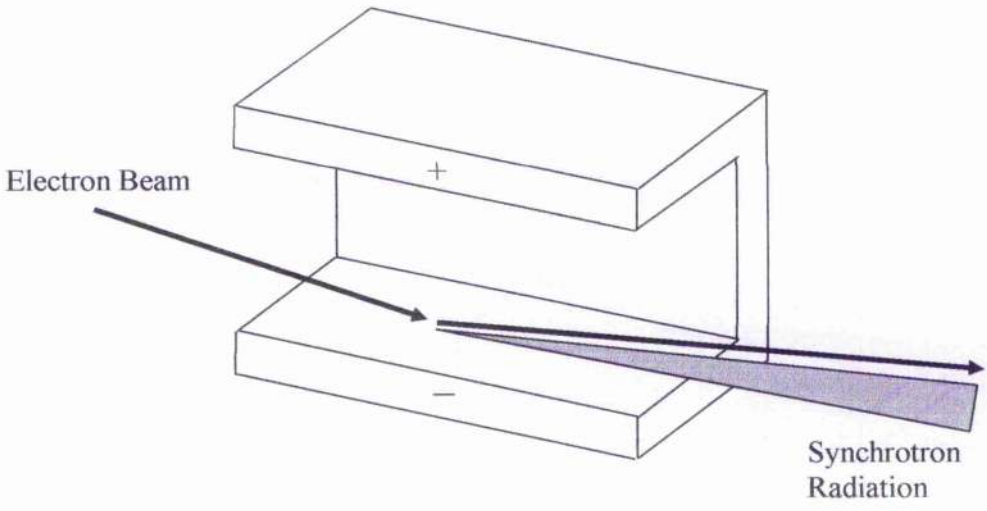

Figure 2.11 Schematic of a dipole bending magnet that is situated within the storage ring. Synchrotron radiation is emitted as the beam is deflected as it passes through the bending magnet.

Undulators are composed of small magnets in an array forcing the electrons into a wavy or undulating trajectory. This results in the radiation beams overlapping and interfering with one another and thus producing a more intense radiation beam. The emitted radiation produces a strong peak at a specific photon energy with higher harmonics, and the radiation is emitted in a cone that is narrower than that produced by bending magnets. The narrow beam is well collimated in both the vertical and horizontal directions with intense radiation at a specific wavelength and has a high spectral brilliance (brightness). An advantage of an undulator is that the emitted radiation is in a cone with small divergence; therefore, the majority of the photons that are emitted strike the sample. Beam divergence is increased when the beam is focused to a smaller size; however, apertures can decrease beam size and divergence but this results in a loss of flux.

Wigglers are similar to undulators in that they consist of a linear array of alternating magnetic dipoles but usually have fewer dipoles than undulators, forcing the electrons to oscillate and emit electromagnetic radiation. Multipole wigglers usually have higher magnetic fields compared to bending magnets, stimulating more radiation at higher energies since the electrons are forced around tighter bends. Wigglers produce a spectrum with higher flux which extends to shorter wavelengths compared to that produced by bending magnets. Therefore, the radiation is emitted over a range of energies. Focusing magnets maintain a well-defined electron beam in the storage ring; these are placed on the straight sections. Specific wavelengths of the synchrotron radiation can be tuned by changing the spacing of the magnets; therefore, each beamline can have its own spectral characteristic. The emitted synchrotron radiation is directed down beamlines which extend tangentially off the storage ring. The radiation is then used at each specific beamline, which has been designed for specialised experiments.

2.9 SAXS Instrumentation

The three main sources of data collection were the NanoSTAR facility at Cardiff University, beamlines 14.1 and 6.2 at the Synchrotron Radiation Source, Daresbury Laboratory, and beamlines ID18F and ID13 of the European Synchrotron Radiation Facility. The X-ray source for beamlines 14.1 and 6.2 are multipole wigglers, and undulators for beamlines ID18F and ID13. Each of the SAXS instrumentation set-ups are described below.

2.9.1 NanoSTAR Facility

The NanoSTAR facility is an in-house X-ray scattering system at Cardiff University that is capable of both SAXS and XRD measurements depending on the sample to detector distance (Figure 2.12). It is a commercially available system from Bruker AXS (Karlsruhe). This system has been used for the data collection of partially ordered biological systems, collagenous materials such as tendon, parchments, skin and bone, and also cellulose fibres. The NanoSTAR is mainly used to analyse samples under vacuum; however, hydrated samples can be examined but they need to be contained within specific sample cells to avoid dehydration in the vacuum sample chamber.

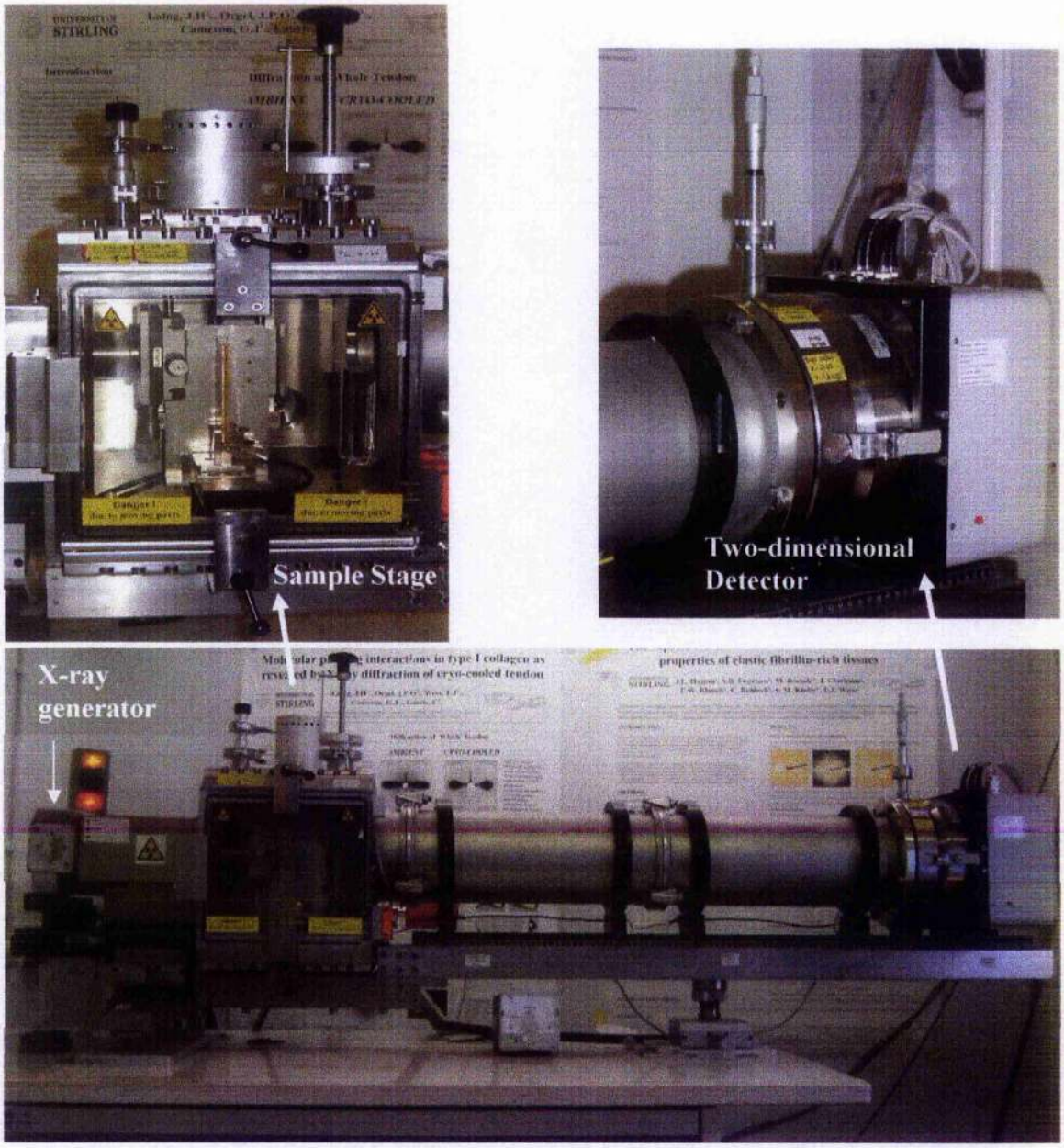

Figure 2.12 Images of the NanoSTAR. The top images show the detector and the sample stage, both the x-y sample stage and the two-dimensional area detector are computer controlled.

A Kristalloflex 760 X-ray generator is used to generate X-rays from an electrical source. Cross-coupled Göbel mirrors (Schuster and Göbel, 1995) and a 3 pinhole collimation system focus the X-rays to provide a highly intense, parallel X-ray beam of 0.4 mm by 0.8 mm and with a wavelength of 0.154 nm (Cu Kα). Göbel mirrors are parabolically bent; this results in a divergent beam hitting the mirror at different locations and angles producing a diffracted parallel beam. The scattering data is collected on a HI-STAR two-dimensional position-sensitive gas detector allowing both isotropic (identical in all directions) and anisotropic (exhibiting different properties in all directions) scattering data to be measured. The detector is comprised of an X-ray proportional chamber, two-dimensional multiwire grid, and electronics that control the detector, data collection and storage. The proportional chamber contains a beryllium window, which reduces X-ray absorption and parallax effects. To ensure the complete capture of all incoming X-ray photons, there is a high pressure xenon gas mixture. Each photon changes to a charged pulse and is collected on the multiwire grid.

The NanoSTAR has many advantages compared to the synchrotron radiation sources: the system is on site; therefore, it is readily available to use, unlike synchrotron radiation sources where beamtime needs to be applied for and time is limited. The NanoSTAR system is automated; therefore, samples can be loaded and left to collect data over a length of time defined by the user. The NanoSTAR sample holder has been designed to allow multiple samples to be analysed at one time therefore reducing the loading time of samples into the NanoSTAR.

2.9.2 Daresbury Synchrotron Radiation Source, Station 14.1

This station is used for protein crystallography, fibre diffraction and non crystalline diffraction. A fan of 4 mRad of radiation is provided to the beamline from the side of the multipole wiggler. Through the use of a 1.2 m silicon substrate, rhodium coated and water cooled mirror, the incoming radiation is vertically focused. The monochromator at station 14.1 is one of two cut Si (111) crystals to produce wavelengths of 1.488 Å and 0.977 Å. The focused, collimated and monochromatic X-ray beam has a focal spot of 200 μm by 200 μm. An image can take around a few tens of seconds to a few minutes to collect. The detector that is used is a Quantum 4 ADSC (area detector systems corporation), which has a readout time from 1 s to 9 s. The beam stop is made of lead and is mounted on a mylar strip.

2.9.3 Daresbury Synchrotron Radiation Source, Station MPW6.2

A detailed description of MPW6.2 (multi-pole wiggler 6.2) is provided in Cernik *et al.* (2004) and Tang *et al.* (2004). MPW6.2 is used for combined small angle X-ray scattering (SAXS), wide-angle X-ray scattering (WAXS) or powder diffraction and extended X-ray absorption fine structure spectroscopy (EXAFS) experiments (Tang *et al.*, 2004). This station enables examination of studies in solids and solutions to investigate changes in atomic and molecular arrangements. The high flux X-ray beam and low bandpass allows for the study of *in situ* material processes and for kinetic systems where the experiments involve nucleation and crystallisation, this is the case for the crystallisation experiments of calcium carbonate as described in Chapter 6.

The X-ray source for the station is a 10-pole wiggler that produces radiation which is split into two beams. The beamline consists of two lead shielded hutches, where the first hutch is the optics and the second is the experimental hutch. Within the latter, there is a one-

dimensional WAXS detector, EXAFS table and SAXS quadrant detector. The readout system uses Refined ADC (analogue-to-digital converter) Per Input Detector (RAPID) electronics (Berry *et al.*, 2003; Helsby *et al.*, 2003), which enables the detectors to operate at very high-count rate and permits for short data collection times around the millisecond and second regions.

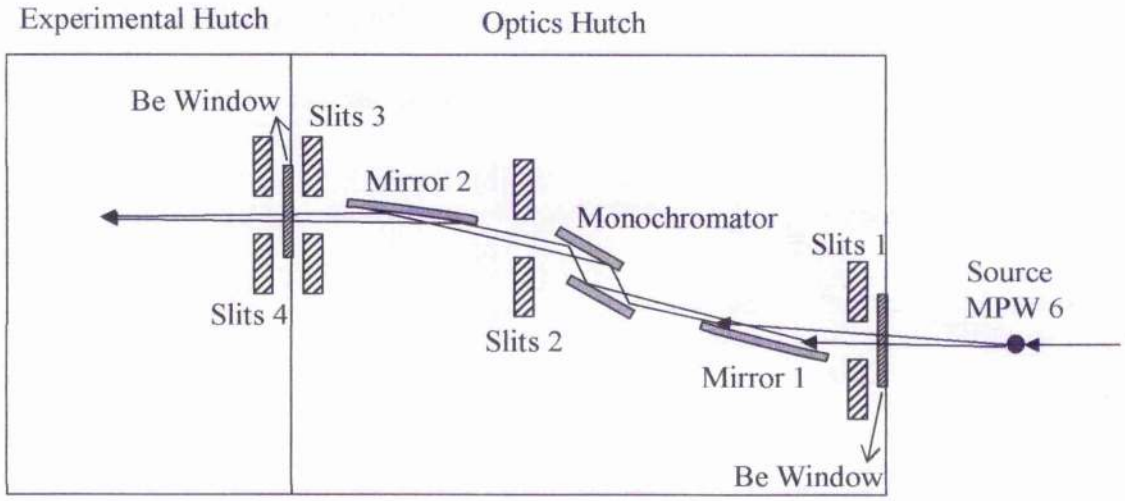

Figure 2.13 Schematic of the layout of station MPW 6.2 at SRS Daresbury showing all the optical components that are involved in the vertical focusing of the beam to the station. This schematic has been adapted from Tang *et al.* (2004).

The optics within the station consists of firstly one planar mirror, which provides a vertically collimated beam for the monochromator, the optics components are shown in Figure 2.13. The second mirror is after the monochromator and focuses the beam vertically. The monochromator has a double bounce arrangement and consists of two single silicon crystals that have the (111) direction cut normal to the reflecting surface (Tang *et al.*, 2004); this system allows for horizontal focusing of the beam (Figure 2.14). The energy range available

at this station is 5 to 18 keV; the optimum photon flux output is at a peak at about 8 keV (Cernik *et al.*, 2004). The focused beam size is approximately 0.5 mm vertically by 2 mm horizontally.

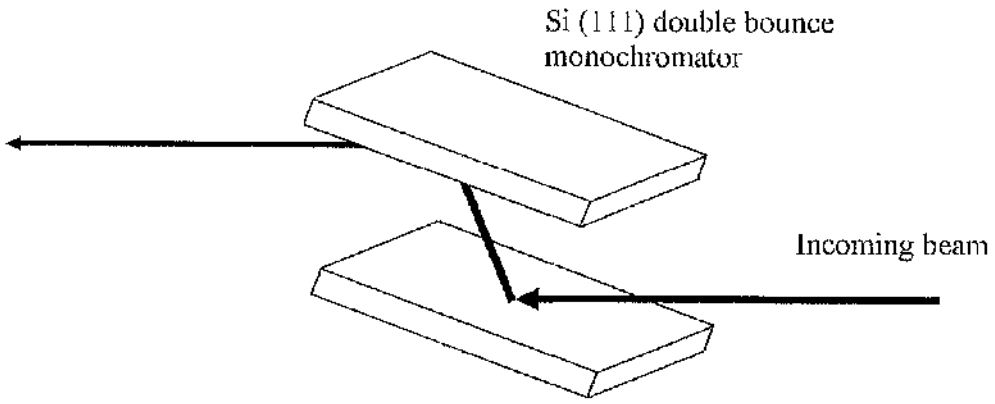

Figure 2.14 Schematic of a Si (111) double crystal monochromator, which helps focus the beam horizontally.

2.9.4 European Synchrotron Radiation Facility, Beamline ID18F

ID18F is used for scanning X-ray fluorescence microscopy, and XRD and SAXS microdiffraction (Figure 2.15).

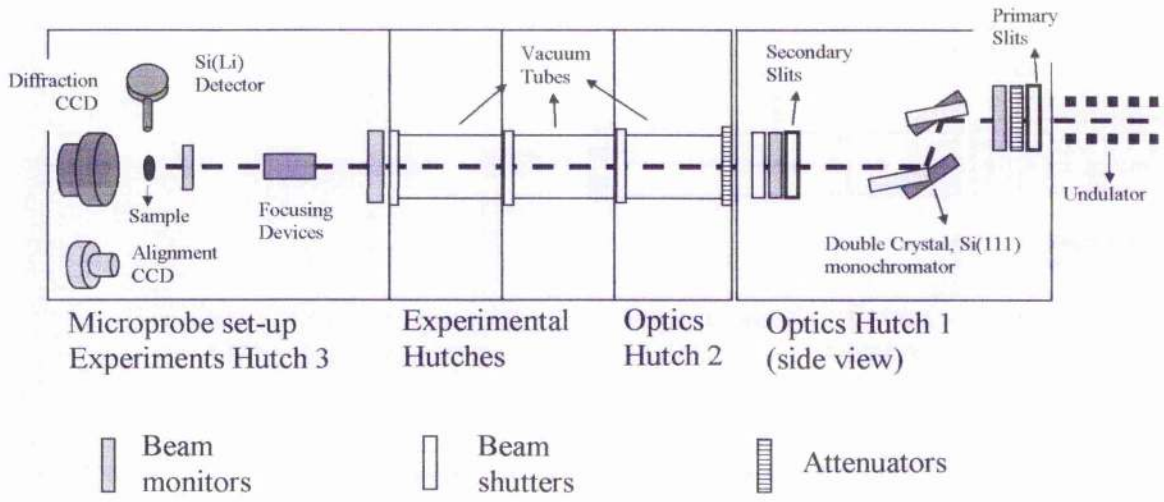

Figure 2.15 Schematic of the layout of beamline ID18F, showing the optics hutches and experimental hutches. Each beamline at the ESRF includes optics, experimental and control hutches. The control hutch at ID18F is found beside the third experiment hutch although has not been included in this diagram. This diagram has been adapted from Somogyi *et al.* (2001).

To produce a tuneable monochromatic excitation beam with an energy range of 6 – 27 keV, the beamline uses three undulators and high heatload fixed exit double crystal Si(111) monochromator (Somogyi *et al.*, 2001). The beamline has three detectors: a Si(Li) detector, a high resolution charge coupled detector (CCD) camera, and a two-dimensional diffraction CCD camera. Parabolic compound refractive lenses (CRL) (Snigirev *et al.*, 1996; Lengeler *et al.*, 1999), found at a distance of about 59 m from the X-ray source are used to produce a

focused X-ray beam. A number of individual Al lenses are used depending on the focused beam energy to comprise the CRL (Figure 2.16).

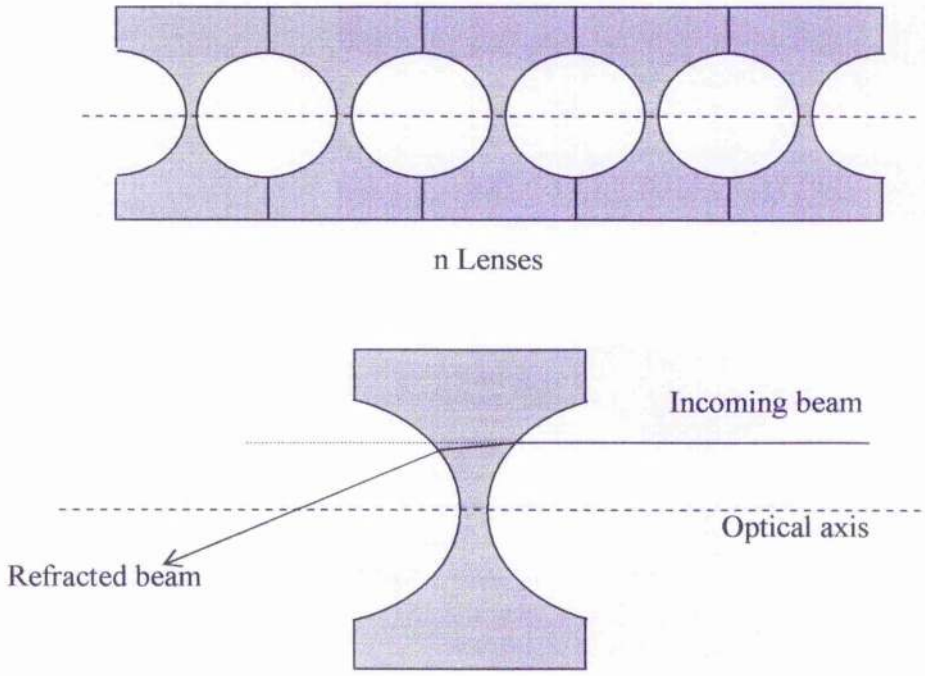

Figure 2.16 Schematic of a compound refractive lens at the top; underneath is an individual unit of a compound refractive lens used at ID18F to focus the beam. The CRL is composed of individual Al lenses.

The Si(Li) solid state detector (GRESHAM) is used to detect the characteristic X-ray line intensities produced from the excited micro sample area (Figure 2.17). This detector is used to collect fluorescence data simultaneously with the diffraction data if required; it has a 30 mm^2 active area, 3.5 mm active thickness and an 8 μm thick beryllium window. The Si(Li) detector is placed 90° to the plane of the incident beam. The X-ray spectra are collected by a

CANBERRA 9660 digital signal processor and a CANBERRA 556A AIM (acquisition interface module).

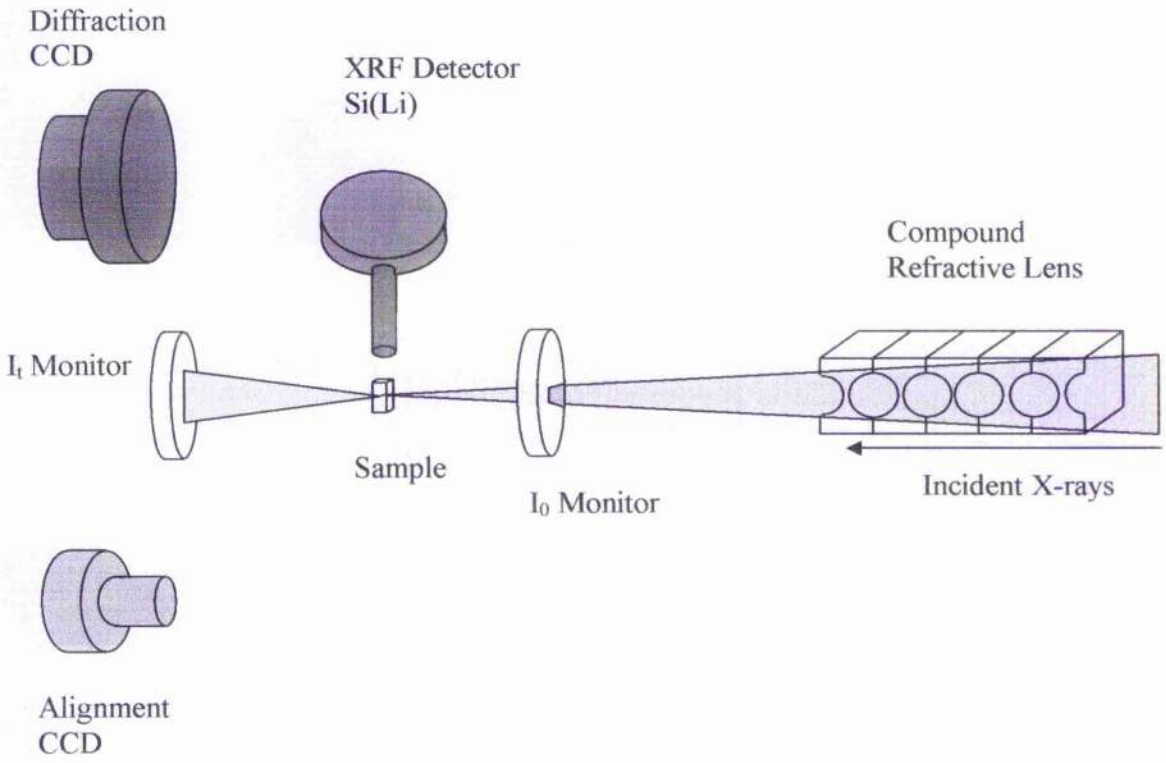

Figure 2.17 Schematic of the layout of the microfocus set-up at ID18F, showing the CRL, different detectors that are used, and the ionisation chamber monitors.

A high resolution X-ray camera is used to align the microprobe and to obtain a radiographic image of the sample. When the X-rays hit the thin phosphor screen they are changed to visible light and using light magnifying optics they are imaged on a 14-bit dynamic range CCD camera (Sensicam), with a resolution of approximately 1 μm and a field width of approximately 0.6 mm. The use of this camera ensures that the microprobe is aligned onto

the area of the sample that is to be scanned and also that the scanning area is known for reference purposes. The images produced on the Sensicam can be saved onto a computer controlled within the hutch.

The detector that is used for the collection of the X-ray scattering data is a CCD camera, described in Wess *et al.*, (2002). The X-rays hit a gadolinium-oxosulphate powder film, which is 30 mm thick and converts the X-rays into visible light. The camera is coupled to a tapered fibre-optic bundle which transfers the light to a peltier cooled CCD chip producing 16-bit dynamic range. The read-out time from the CCD camera is approximately 20 s. The software controlling the detector is within the hutch. To protect the detector from the direct beam a tungsten backstop 500 μm in diameter was used to absorb the main beam.

Between the CRL and the sample there is space for a pin-hole to define the beam-shape and also a photodiode and/or ionization chamber for beam monitoring. The focused beam has an intensity of typically 5×10^{10} photons per second; this is dependent on the number of undulators that are used as well as the incoming beam energy. The beam size is usually 1-2 μm vertically and 12-15 μm horizontally (FWHM); however, the horizontal beam size can be reduced if the secondary slits are closed. This will result in a decrease in the intensity: for example, for a 5 μm beam size, there will be a loss of intensity of about 40 %. The ionisation chamber monitors the incoming focused beam intensity and is used for correcting the variation in intensity of the excitation beam. It is 10 mm parallel to and 5 mm perpendicular to the beam direction so it is small enough that it can be placed relatively close to the sample.

The sample is mounted onto a sample stage (or can be mounted onto a goniometer head or slide frame holder), which consists of one rotation and three translation motors. The three translation motors control the sample alignment in the horizontal and vertical directions, where the scanning range is 50 mm by 50 mm, horizontal and vertical. The minimum horizontal step size is 1 μm and 0.1 μm vertically. The incidence angle to the surface of the sample can be adjusted on a vertical axis using the rotation stage.

2.9.5 European Synchrotron Radiation Facility, Beamline ID13

ID13 is a microfocus beamline, which provides small focused beams for X-ray diffraction and small angle X-ray scattering. The set up allows for both scanning diffraction and single crystal diffraction experiments, and also scanning X-ray microfluorescence. Further information about the beamline can be found on the ESRF website at www.esrf.fr. Briefly, the X-ray source for this beamline uses an 18 mm period in-vacuum undulator, which has been optimized to obtain energy of 13 keV. There is also a 46 mm period tuneable undulator for different energies. The incident photon energy range is between approximately 5 keV and 17 keV; however, without focusing, higher energies are available. The beamline also uses a liquid nitrogen cooled Si(111) double monochromator. The detector used is a two-dimensional Mar-CCD with 2048 by 2048 pixel image.

The station has two experimental hutches, where the first contains a microgoniometer, and using a focusing mirror and aperture combination generates beam sizes of 5, 10 and 30 μm. This hutch is specifically used for fibre diffraction, protein crystallography and small unit cell crystallography. The second experimental hutch, contains an x/y scanning stage and also specific optics to obtain a beam of ≥ 5 μm microbeam, a Kirkpatrick-Baez (KB) mirror (Kirkpatrick and Baez, 1948) and defining collimator are used. KB mirrors are grazing

incidence reflecting mirrors used to focus X-rays to spot sizes of the micron spatial scale. One reflector focuses in one dimension and another reflector focuses in the second dimension and is found further downstream than the first. A 2 μm beam size is obtained through use of capillary optics, where the beam divergence at the capillary exit is 2.3 mrad at 13 keV. 0.5 μm beam can be achieved by KB mirror submicron beam optics. By using waveguide optics a beam size of about 100 nm can be achieved, the horizontal beam size can be compressed to about 3 μm by a mirror.

2.10 XRD and SAXS Data Analysis

The XRD and SAXS data collected from the X-ray facilities described previously were analysed as detailed in the next sections.

2.10.1 XRD Data Analysis

The two-dimensional diffraction data from powdered eggshell samples obtained from the NanoSTAR facility, and station 14.1 at the SRS Daresbury Laboratory were converted and output as a linear trace (Intensity against Bragg angle degrees 2θ). The full width at half maximum (FWHM) measurements of the more predominant (104) reflection peak of calcite was fitted into the following Debye-Scherrer equation (2.15) to obtain the average crystallite size.

$$D = \frac{K\lambda}{\beta\cos\theta} \tag{2.15}$$

λ is the wavelength, θ the diffraction angle, K is a numerical constant of the order of unity, which Scherrer found to be $2(\log 2/\pi)^{1/2} = 0.94$, $\beta = \sqrt{(B^2 - b^2)}$, where B is the breadth of

the observed peak, and b is the breadth arising from instrumental broadening obtained from a standard diffraction pattern (Newman, 1999). For example, the highly crystalline [004] reflection peak from cellulose at a d-spacing of 0.2585 nm was used as b in this study. The FWHM measurements taken from the linear peak profile were extracted using the computer program Xfit obtained from Collaborative Computer Project 13, UK. The peak widths were measured using a Voigtian line shape fitting, which is the convolution of a Lorentzian with a Gaussian; this ensured the most appropriate and accurate measurements as it provided the best fit to the data. The ratio of the width of the Lorentzian to the width of the Gaussian, w, corresponds to the shape parameter, s. When $s = 0$, the consequent curve is a Gaussian of width w. This can be expressed as equation 2.16 (www.ccp13.ac.uk/software/program/xfit.html), where h is the height of the peak.

$$y = h\int \frac{e^{-4\ln 2(t/w)^2}}{[(x + (2\ln \frac{2}{w})^2) + \ln 2s^2]} dt \qquad (2.16)$$

2.10.2 SAXS Data Analysis

The two-dimensional SAXS data collected on the NanoSTAR and at the ESRF were integrated azimuthally as shown in Figure 2.18, where 0 is the scattering angle and χ is the azimuthal angle in the plane of the detector. This SAXS data analysis can provide information concerning crystal size and shape (Gupta *et al.*, 2003).

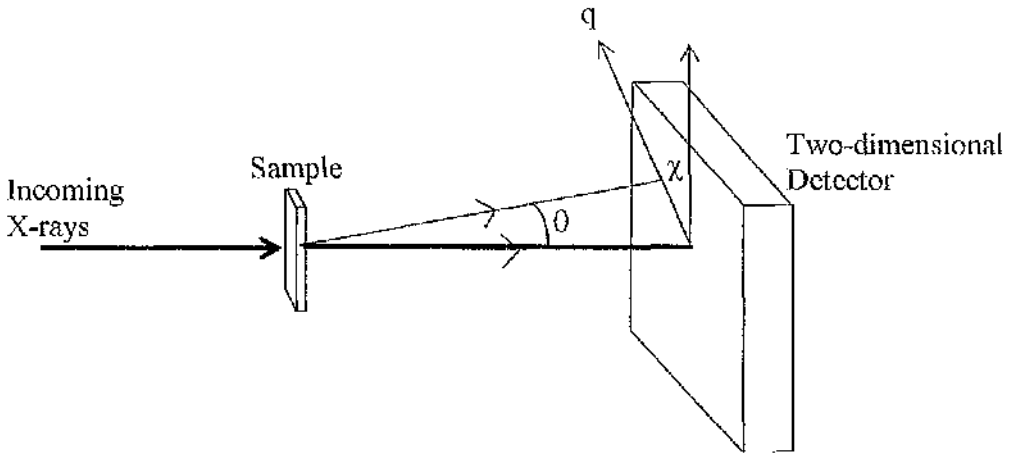

Figure 2.18 Schematic of a typical SAXS experimental setup. θ is the scattering angle and χ is the azimuthal angle in the plane of the two-dimensional detector.

With the data from the NanoSTAR and the ESRF, the intensity I(q) was plotted against q as linear traces, where q is the scattering vector and is equal to $q = \frac{4\pi \sin\theta}{\lambda}$, λ is the wavelength, and θ is the angle between the incident beam and the scattered beam. The linear SAXS intensity profiles allowed the surface area to volume ratio to be determined, which gives information on the size of the scattering objects. From the linear profiles, two parameters, the invariant and Porod constants were determined; the invariant, J, provides

information on the average volume and the Porod constant, P, provides information on the surface area. The invariant is the total area under the curve obtained in a Kratky plot ($I(q)q^2$ against q) (Figure 2.19). The Porod constant is the y-intercept in a Porod plot ($I(q)q^4$ against q^4), as described in subsection 2.6.2.1.

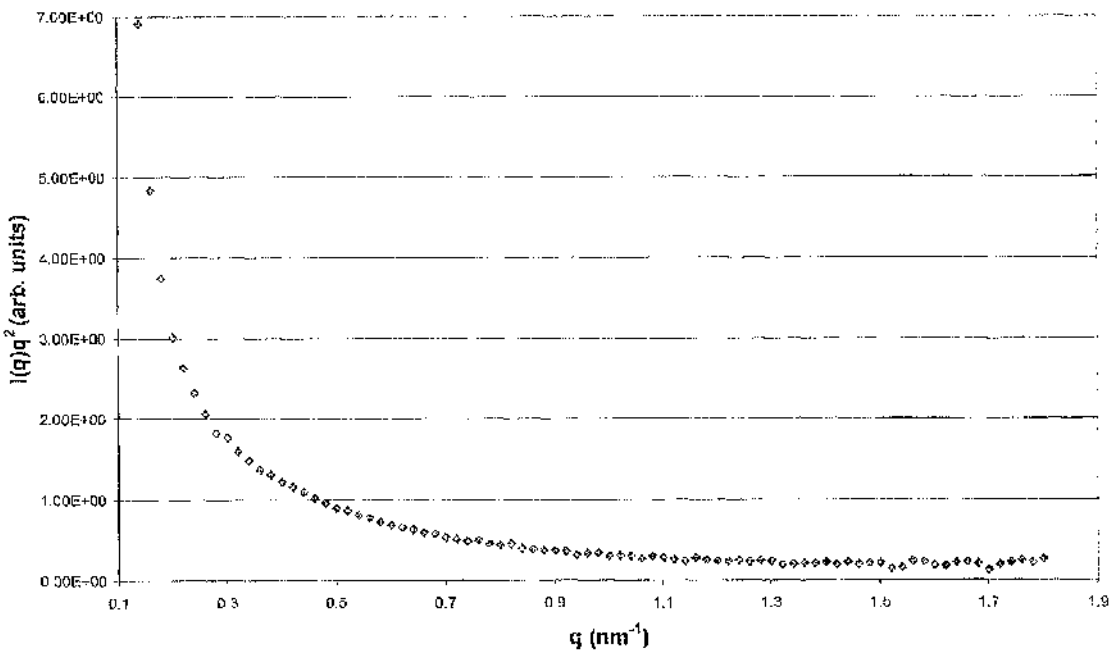

Figure 2.19 Scattering intensity ($I(q)q^2$) plotted against q produced by integrating the two-dimensional SAXS data.

The data is plotted from q_{min} (0.14 nm^{-1}) to q_{max} (1.8 nm^{-1}); when calculating the invariant, the curve is extrapolated to q = 0 and q = ∞. At high q values, above q_{max}, the curve $I(q)q^2$ can be extrapolated using Porod's Law. At low q there is no rule to extrapolate, and so the curve must be estimated with the least error. In the case here, little contribution is made at

low q before q_{min} from this region to the total integral and therefore can be extrapolated linearly to zero (Fratzl *et al.*, 1996a). At high q, $I(q) = \frac{P}{q^4}$, which according to Porod's Law applies to systems with sharp interfaces; for example, between the organic and inorganic components. The invariant and the Porod constant can be applied in equation 2.17 to estimate a parameter T, which is the size of the scattering objects, and has been used to determine typical crystal thicknesses in bone samples (Fratzl *et al.*, 1991; 1992; Fratzl, 1994).

$$T = \frac{4J}{\pi P} \tag{2.17}$$

Average properties of the scattering objects can be obtained through integrals and manipulations to provide information on the surface area and average volume. The surface area to volume ratio gives an estimation of the average object size.

2.11 Conclusion

This chapter has provided a background to the experimental techniques used in this thesis, and the XRD and SAXS data analysis was described. The X-ray sources and the different beamlines that were used were discussed. From each of the experimental configurations, valuable information was provided regarding the eggshell structure at the nanometer length scale, which until now has never been investigated using SAXS. This is described in the following results chapters of this thesis.

In the next chapter, microfocus SAXS is used specifically to scan through each of the layers within the eggshell and investigate nanostructural variations within the different layers, by step by step scanning over intact eggshell sections. This provides a more in depth analysis

due to the smaller beam size used, allowing a greater point to point resolution in order to obtain measurable structural parameters such as size of the scattering objects.

Chapter 3

Two-Dimensional Mapping of Normal and Abnormal Eggshells

3.1 Introduction

There are many factors that influence the structure and quality of the eggshell including the nutritional status, breed and age of the hen (Wolford and Tanaka, 1970). Eggshell quality has a direct effect on the economics of egg production with between 8 – 10 % of total egg production being downgraded due to cracked or broken eggshells (Hamilton *et al.*, 1979a). Cracked eggs however do not just result in financial loss to the producers they also pose a health risk to humans since potentially harmful bacteria can more readily enter the egg contents. As a consequence, considerable effort has gone into designing more efficient automated systems for handling eggs (Anderson and Carter, 1976) and developing online crack detection systems (De Ketelaere *et al.*, 2000; 2004). A complementary approach is to improve the strength and quality through breeding or nutritional programs.

The mechanical properties and overall quality of the eggshell result from a precise regulated sequence of events (Fernandez *et al.*, 1997), where structural alterations during the early stages of eggshell formation influence its overall functional properties. During eggshell formation, a number of different proteins are expressed in the oviduct and become incorporated into the eggshell.

As previously stated the mechanical and structural properties of any biomineral are likely to be due to their composition at each length scale. SAXS in conjunction with a focused microbeam allows for greater resolution and detailed analysis of biominerals at the nanometer length scale due to its smaller beam size. Scanning microfocus SAXS (μSAXS)

allows local nanostructural features over select regions or over the entire thickness of a specimen to be investigated. This technique has previously been applied to investigate structural features in other hierarchical biominerals including bone (Paris *et al.*, 2000; Wess *et al.*, 2001a), and calcified avian tendons (Gupta *et al.*, 2003).

The organic matrix component of the eggshell is thought to exert partial control on the eggshell microstructure by influencing crystal size and morphology (Arias *et al.*, 1993; Nys *et al.*, 1999; Nys *et al.*, 2004). In this section, the interaction between the protein and mineral phases of the eggshell are investigated for the first time at the nanometer level. In particular, nanostructural mapping through the thickness of the eggshell at micron size intervals is presented. The possible effects of oviducal dysfunction on the nanostructural properties of the eggshell are also investigated by comparing the nanostructural two-dimensional maps of visually normal versus abnormal eggs.

3.2 Materials and Methods

The eggshell samples used in these investigations were selected on the basis of being visually normal or abnormal following the criteria described by Hughes *et al.* (1986). A normal eggshell is characterised as having a regular shape, with an even colouring and smooth surface. Abnormal eggshells, under the classification of misshapen, are eggs that appear distorted or have a wrinkled shell surface at certain areas or over the entire surface. A total of six eggs, three normal (Figure 3.1A) and three abnormal - wrinkled eggs (Figure 3.1B) were obtained directly from a commercial egg production unit and prepared for microfocus SAXS as follows.

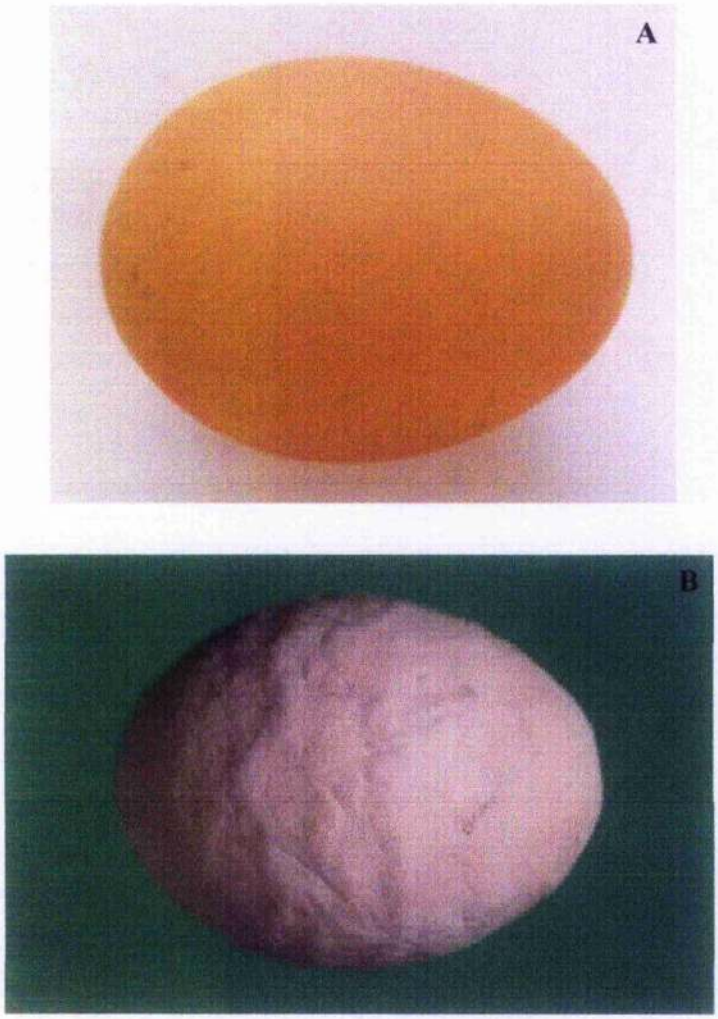

Figure 3.1 A = Example of a normal eggshell, and B = Example of an abnormal eggshell – wrinkled eggshell.

1 cm^2 sections of the normal and abnormal eggshells were removed from the equator of each egg using a rotating, diamond tipped saw attachment fitted to a dentist drill. Each specimen was then impregnated with Crystic resin using butan-1-one peroxide and cobalt octoate catalysts (Adderley *et al.*, 2004). The polyester resin system was mixed with acetone and degassed prior to vacuum impregnation. The embedding procedure was conducted at the University of Stirling. A Buehler Isomet low speed saw with diamond wavering blade was then used to cut impregnated eggshell sections of 300 μm thickness using rapeseed oil as a cutting fluid. All 300 μm sections were analysed on beamline ID18F (described in subsection 2.9.4).

150 μm thick sections of the normal eggshell samples were also prepared and then polished to a final thickness of approximately 110 μm using a DAP-V (Struers, Copenhagen, Denmark), which is a small motor-driven machine that is used for wet grinding, and for diamond and alumina polishing. To allow even finer sections (50 μm) to be attained additional samples of the normal eggshell were embedded using an alternative procedure carried out at the Max-Planck Institute of Colloids and Interfaces, Germany. Briefly, sections of eggshell were cut from the equator, then dehydrated and embedded into polymethyl methacrylate (PMMA). After curing, a diamond saw was used to cut sections, which were then polished to a final thickness of 50 μm. These thinner sections allow for less averaging over the depth of the sample and more accurate parameter measurements, and permitted the mammillary layer of a single calcite column to be examined independently of the surrounding columns. The 50 μm sections were analysed at beamline ID13 (described in subsection 2.9.5).

3.2.1 Data Collection

Microfocus SAXS (μSAXS) was carried out on the microfocus beamlines ID18F (see subsection 2.9.4) and ID13 (described in subsection 2.9.5) at the European Synchrotron Radiation Facility (ESRF), Grenoble, France.

3.2.1.1 Scanning μSAXS at beamline ID18F

At beamline ID18F, the wavelength of the microbeam was 0.086 nm and the beam was focused to 1.5 μm vertically by 7 μm horizontally (full width at half maximum) through the use of a compound refractive lens (Snigirev *et al.*, 1996; Lengeler *et al.*, 1999). The sample to detector distance was 20 cm; in order to stop the direct beam hitting the detector a tungsten backstop 500 μm in diameter was used. The detector pixel size was 150 μm both horizontally and vertically, and the scattering limits range from $q = 0.187\ nm^{-1}$ to $2.00\ nm^{-1}$. Each sample was mounted on a goniometer and then to a motorised stage controlled remotely. The eggshell samples were aligned perpendicularly to the direction of the incident X-ray beam, with the sectioned eggshell facing the beam (membranes at the bottom and cuticle at the top) as shown in Figure 3.2.

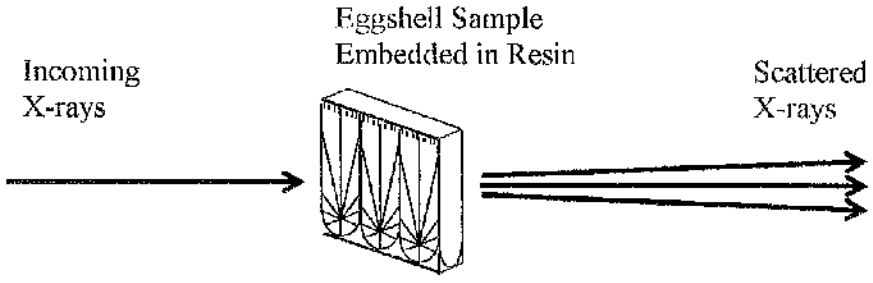

Figure 3.2 Schematic representation showing the alignment of the eggshell sample in the X-ray beam.

In order to observe microscopic features and locate the area to be scanned, an X-ray transmission image (Figure 3.3 and 3.8A) was taken of each of the eggshells prior to starting the microfocus SAXS scans. This was achieved by removing the microfocus elements and using the defocused beam in connection with a high resolution camera (see subsection 2.9.4). Using the microfocused beam, the normal eggshell sections were scanned over 500- by 300-μm areas sampled at intervals of 16.7 μm vertically and 12 μm horizontally. A total of 806 SAXS patterns were taken over this area. Overall scan dimensions ensured that both the outer and inner surfaces of the eggshell were included in the sample. A similar set-up was used for the abnormal eggshells, except the vertical scan length was 500 μm sampled at 16.7 μm intervals, and the horizontal scan length was 300 μm sampled at 10 μm intervals. 961 SAXS patterns were taken over this area. In order to obtain detailed scans from each eggshell sample, the horizontal step size was increased to reduce the time taken for each scan since beamtime was limited. The abnormal eggshells were scanned before the normal eggshells; therefore, the horizontal step size was increased for the normal eggshell scans. The structural detail obtained in the vertical scan provided information about the layers; therefore, instead of losing point to point resolution in the vertical direction only the horizontal step size was increased.

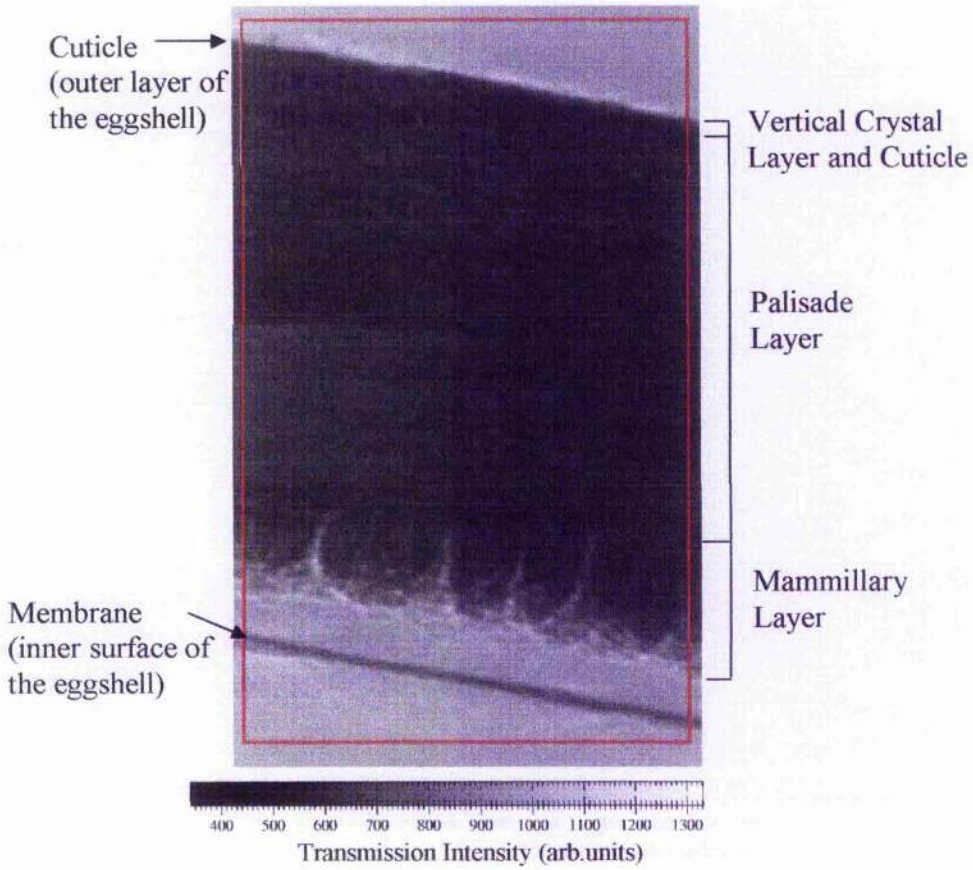

Figure 3.3 X-ray transmission image of a normal eggshell, obtained using the defocused beam. The box in red depicts the scanned region. The sample is bathed in the direct beam; differential X-ray absorbance allows microscopic features to be observed.

3.2.1.2 Scanning μSAXS at beamline ID13

A more detailed analysis focusing specifically on the mammillary layer of the 110 μm section of normal eggshell was investigated at beamline ID13 at the ESRF by using a smaller beam size and step size between each μSAXS measurement. In this experimental configuration, the microbeam was focused to 1 μm in diameter by two sets of Kirkpatrick-Baez mirrors (see subsection 2.9.5). A 16-bit readout CCD detector (X-ray Associates (XRA)) was used to collect data, and the wavelength of the beam was $\lambda = 0.0976$ nm. The scattering limits range from $q = 0.347$ nm^{-1} – 2.601 nm^{-1} and the sample to detector distance was 290 mm. The detector pixel size was 150 μm vertically by 150 μm horizontally. The sample section was attached to the end of a glass capillary using super glue and mounted on the sample stage. A light microscope was used to locate an area of interest on the sample to scan and to align the sample before the microfocus scan commenced. The area of the eggshell scanned corresponded to that of the mammillary layer. The scan dimensions were 130 μm vertically by 100 μm horizontally and each step size was 2 μm vertically and 5 μm horizontally.

The experiments at ID13 were repeated on the 50 μm sections of normal eggshell. The samples were again glued onto the end of a glass capillary tube mounted on the sample stage. A similar experimental configuration at ID13 was used as described before; however, in this case, waveguide optics were used in order to produce a smaller beam size of 300 nm and the sample to detector distance was 360 mm. The area scanned again corresponded to that of the mammillary layer. The scan dimensions were 60 μm vertically and 115 μm horizontally and each step size was 2 μm vertically and 4 μm horizontally. The scattering limits range from $q = 0.263$ nm^{-1} to 2.628 nm^{-1}. X-ray transmission measurements were obtained at exactly the same points on the eggshell as were taken for the μSAXS scan. The photon counts were

measured on a pin diode instead of the detector. These values were used to produce a two-dimensional transmission map.

3.2.2 Data Analysis

Using the FIT2D software package (A.P. Hammersley, ESRF, France), composite images of the two-dimensional microfocus SAXS patterns from the sections scanned at both beamlines ID18F and ID13 were produced (Figures 3.4B, 3.8B, 3.11B, 3.12B). The program was also used to generate the corresponding total intensity maps, where the greater the total scattering intensity the darker it will appear on the map (Figures 3.4C, 3.8C, 3.11C, 3.12D). These maps provide information about regions in the eggshell where there are greater electron density contrasts therefore resulting in an increase in scatter.

Details regarding the SAXS data analysis are given in subsection 2.10.2. Briefly, to obtain further information from the data, the scattering intensity of the two-dimensional μSAXS patterns were integrated to one-dimensional linear profiles with the background subtracted (Gupta *et al.*, 2003). From the linear profiles, the surface area to volume ratio, which gives an indication of the dimensions of the scattering object were determined through the two parameters, the invariant and Porod constant, as described in subsection 2.10.2. The scattering curves were analysed using Porod's Law (2.6.2.1) to determine the surface area of the scattering objects (refer to subsection 2.10.2). Two-dimensional maps of the invariant i.e. the data, extrapolated in the Guinier and Porod regions, were produced using in-house software. These maps provide an indicator of the amount of scattering interfaces within the scattering volume as they take into account the Porod tail, and therefore provide details about the nanoporosity within the sample. In this study, the size parameters of the smallest dimension of the scattering objects throughout the eggshell thickness were determined using

the method given by Fratzl *et al.* (1996). These values were used to generate two-dimensional maps that show nanostructural changes over a section of the eggshell at each point where a scattering pattern was collected. These maps were also characterised by a varying grey scale, where the larger the size value the darker the shade on the map.

3.3 Results

3.3.1 ID18F – Normal Eggshells

An X-ray transmission image of a normal eggshell using the defocused beam is shown in Figure 3.4A. The X-ray transmission image highlights the granular texture of the eggshell shown by the dark/light regions. This is most noticeable at the inner face of the eggshell, i.e. the mammillary layer region. In comparison, the palisade layer shows a more homogeneous texture, although structural variations seem to occur with a greater frequency at the outer palisade layer and towards the cuticle; these features hence forth referred to as microvoids cannot be detected or analysed by μSAXS because they are too large. In addition to microvoids, the scattering data presented in composite image Figure 3.4B suggests that there is also a population of nanovoids throughout the eggshell thickness; this is particularly obvious in the scattering patterns corresponding to the mammillary layer.

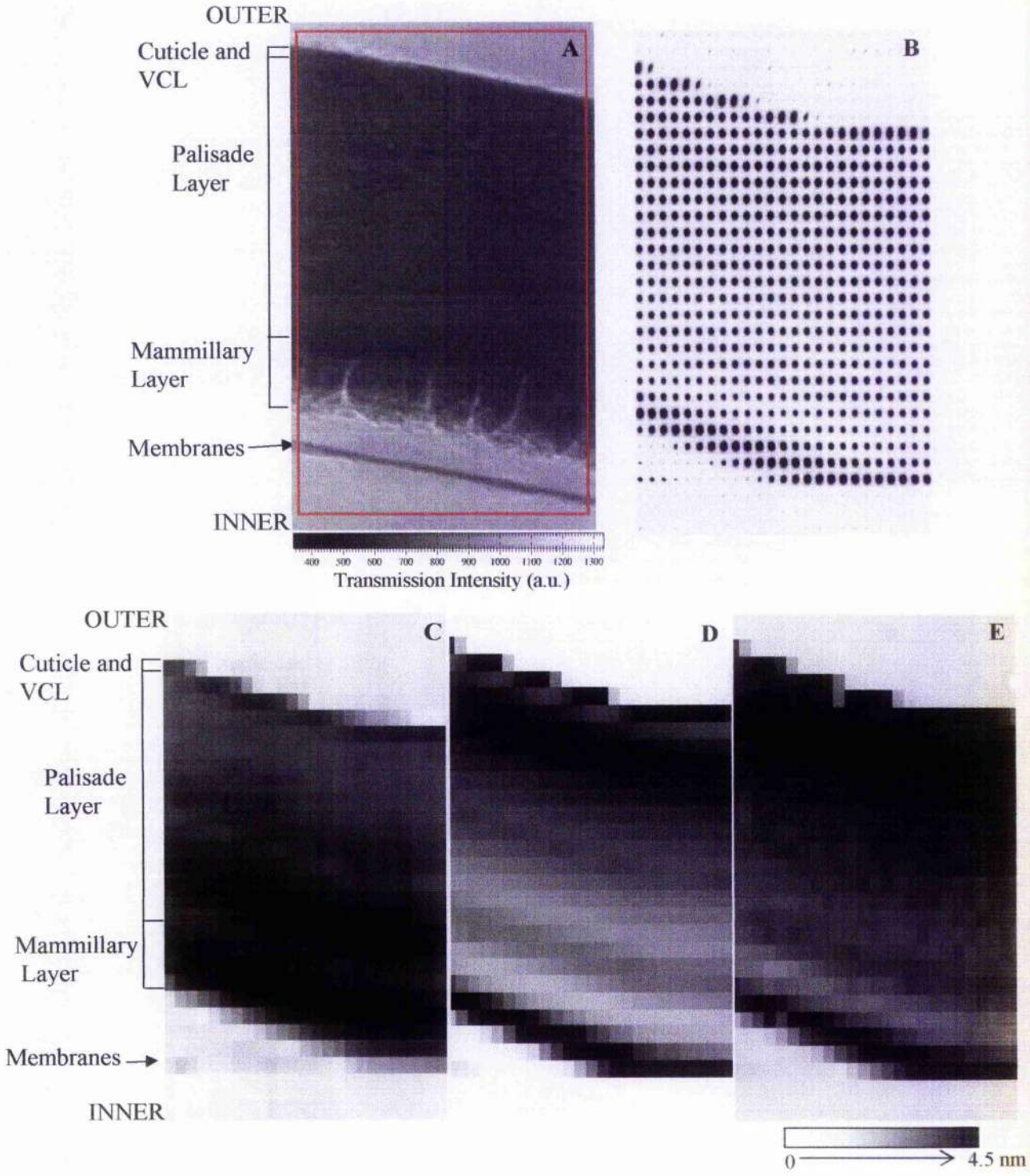

Figure 3.4 Two-dimensional maps composed from the data collected at ID18F from a normal eggshell. (A) X-ray transmission image. The box depicts the scanned region. (B) Composite of the μSAXS images obtained from the scanned section of eggshell. The top and bottom of the composite image corresponds to the embedding resin and therefore should be discounted. (C) Total scattering intensity map from each point on the two-dimensional scan, where the greater the intensity the darker the tone. (D) Invariant map from each point on the two-dimensional scan, where the greater the invariant the darker the tone. (E) Size dimension map showing size variation through the different layers of the eggshell, the darker shades correspond to a larger size value (scale bar is given).

The total scattering intensity map of each μSAXS pattern mapped over the section scanned is shown in Figure 3.4C. According to this figure, there are darker bands of tone within specific regions of the eggshell indicating that there are differing amounts of scatter depending on the nanoscopic features being sampled within the eggshell. For example, there is a gradual reduction in tone with the intensity becoming lower as the scan proceeds to the outer of the eggshell.

The invariant is the total integral (described in subsection 2.10.2) and was calculated for the individual scattering patterns and used to produce the two-dimensional map shown in Figure 3.4D. This type of map provides greater detail about the nanoporosity within the sample. In Figure 3.4D banding occurs throughout the different layers of the eggshell. Specifically, there is a dark band apparent in the mammillary layer and at the outer palisade region. These two regions therefore exhibit a higher nanoporosity than some of the other regions of the eggshell. The invariant together with the information presented in Figure 3.5 were required to calculate the smallest dimension of the scattering object within the eggshell sample as displayed in Figure 3.4E.

To produce Figure 3.4E , typical linear traces of the X-ray scattering intensity profiles from selected points within a vertical scan were plotted on a double logarithmic graph; different markers are used in Figure 3.5 to distinguish between the positions of the scans. Curves corresponding to scatter from the resin lie beneath the others and show clear differences in scattering compared to those from within the eggshell. A similar feature can also be seen with the scattering curve obtained from the membrane. The decaying intensity of the scattering curve at larger values is inversely proportional to the fourth power of q, an indication that the use of Porod's Law (see subsection 2.6.2.1) in the analysis is appropriate.

The 'knee' region of the curve gives an indicative lower limit size measurement of the scattering object when extrapolated to the q-axis and converted into real space; this was found to be 2.17 nm for the normal eggshell samples.

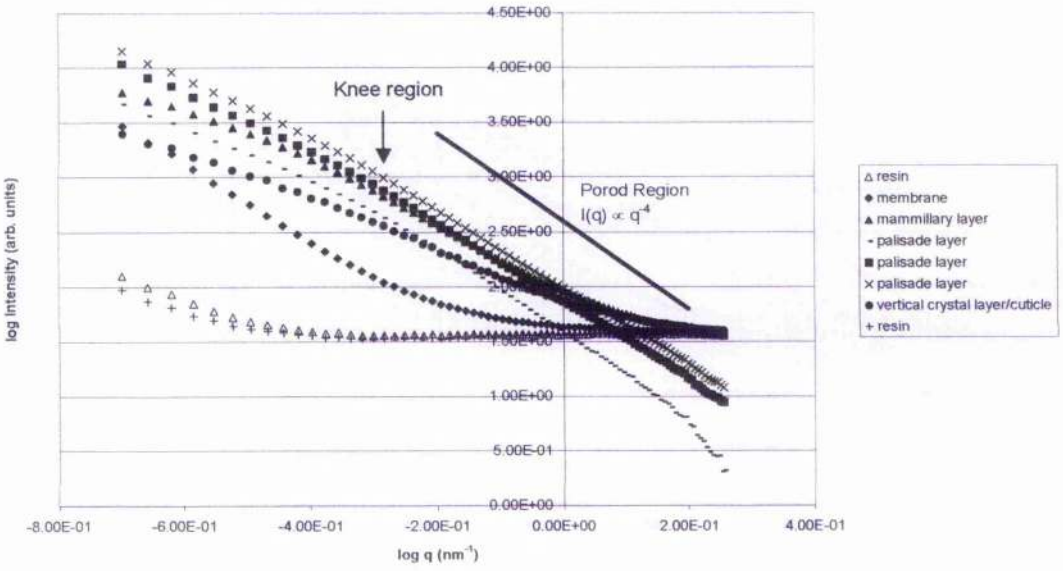

Figure 3.5 Double logarithmic graph of the one dimensional linear traces produced from the integrated intensity data. Linear traces from specific representative points on one of the vertical linear scans are indicated. The straight line depicts the Porod region. The knee region on the scattering curve gives an indicative size measurement of the scattering object. The embedding resin and membrane scattering curves are beneath the scattering from those within the calcified part of the shell. A constant background was subtracted from the scattering data.

In the context of this investigation, each individual scattering pattern allowed a corresponding size parameter at that point in the scan to be determined. These were subsequently used to produce two dimensional composite maps of size with varying grey scale (Figure 3.4E). The resulting composite maps show that there are changes in the scattering distribution within the different layers of the eggshell. The distinct darker bands towards the mammillary layer and nearer the outer region are indicative of changes in the scattering intensities. The size values within the mammillary layer were estimated to be approximately 3.9 nm. Within the palisade layer the size values decreased to approximately 3.6 – 3.8 nm, and then to approximately 3.0 - 3.5 nm at the most outer layer. It is possible that these changes in size values could be due to localised variations in the protein component of the organic matrix.

Visual assessment of the two-dimensional map with its varying grey-scale (Figure 3.4E) confirms that local nanostructural variations occur throughout the layers of the eggshell. The size values obtained at representative positions through three separate vertical scans from the inner to the outer surface of a normal eggshell are shown in Figure 3.6. The data presented in this figure suggests that there is only a small variation in size value between the different regions of the eggshell. The values obtained from the additional vertical scans confirm this result.

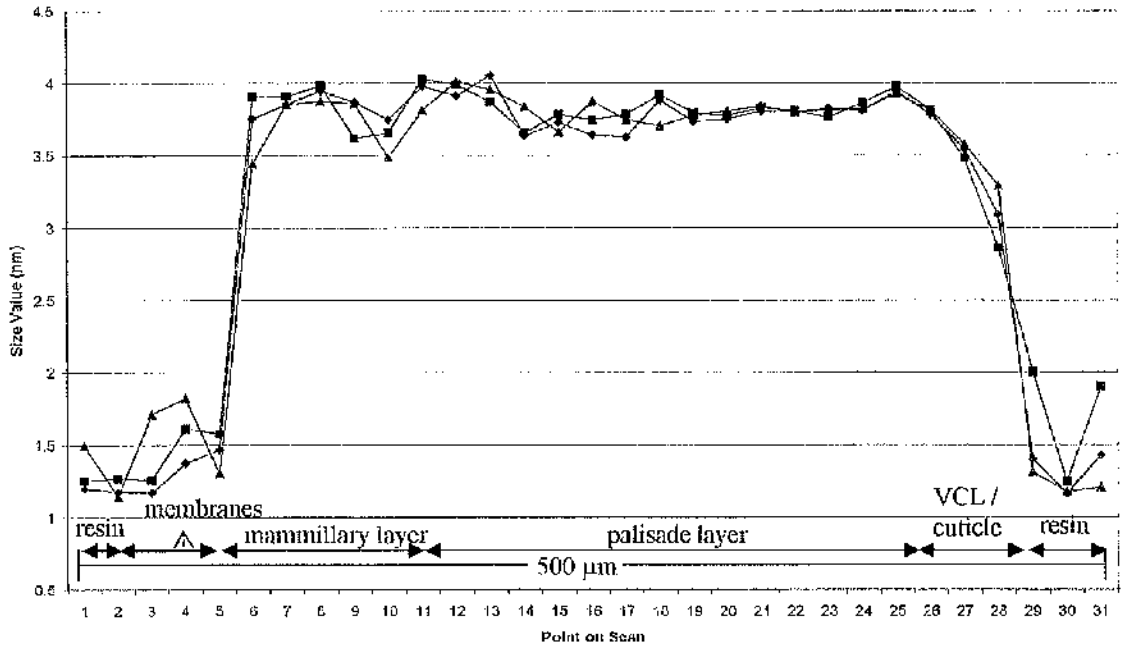

Figure 3.6 Measurements of the smallest dimension of the scattering objects from three scans at different areas from within a normal eggshell, each scan is depicted by a different symbol. The scans start at the inner membrane and finish at the outer surface cuticle. Embedding resin measurements are also included at the beginning and at the end of the scans.

The change in the invariant (total integral) of the scattering profiles from one of the vertical scans within the mesh is shown in Figure 3.7, indicating that the strength of scattering increases from the inner to outer region of the palisade layer. The largest value at point 8 corresponds to the central core of the mammillary layer.

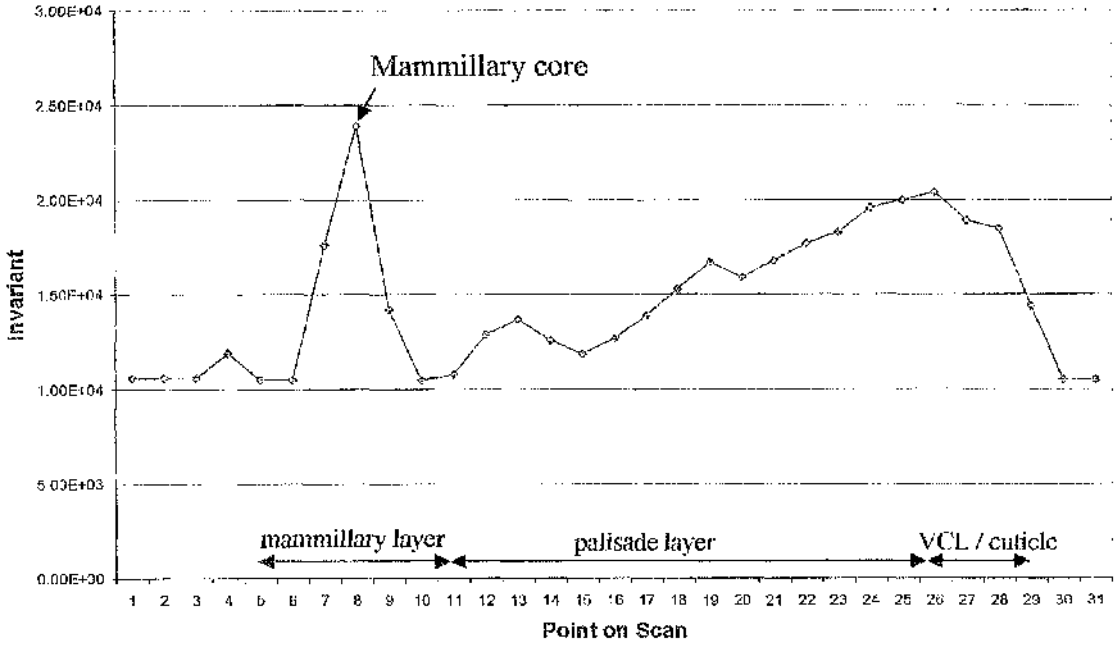

Figure 3.7 The invariant of the scattering intensity at each of the points on the vertical scan for a normal eggshell sample. The sample length was 500 μm for each vertical scan.

3.3.2 ID18F – Abnormal Eggshell

The X-ray transmission image from an abnormal eggshell is shown in Figure 3.8A. This image reveals that structural variations appear to exist throughout the shell thickness, and also gives the impression that the membrane has not been laid down correctly over the egg white (Figure 3.1B). This is consistent with the literature which states that wrinkled eggs arise from a dysfunction of the isthmus region of the oviduct, which is responsible for the formation of the shell membranes (Solomon, 1991). The palisade layer shows a homogeneous texture as seen with the normal eggshell. Microvoids can also be observed at the mammillary layer, the outer palisade and towards the exterior of the eggshell. Again these results coincide with a greater scattering signal seen within these regions in the composite scattering patterns shown in Figure 3.8B.

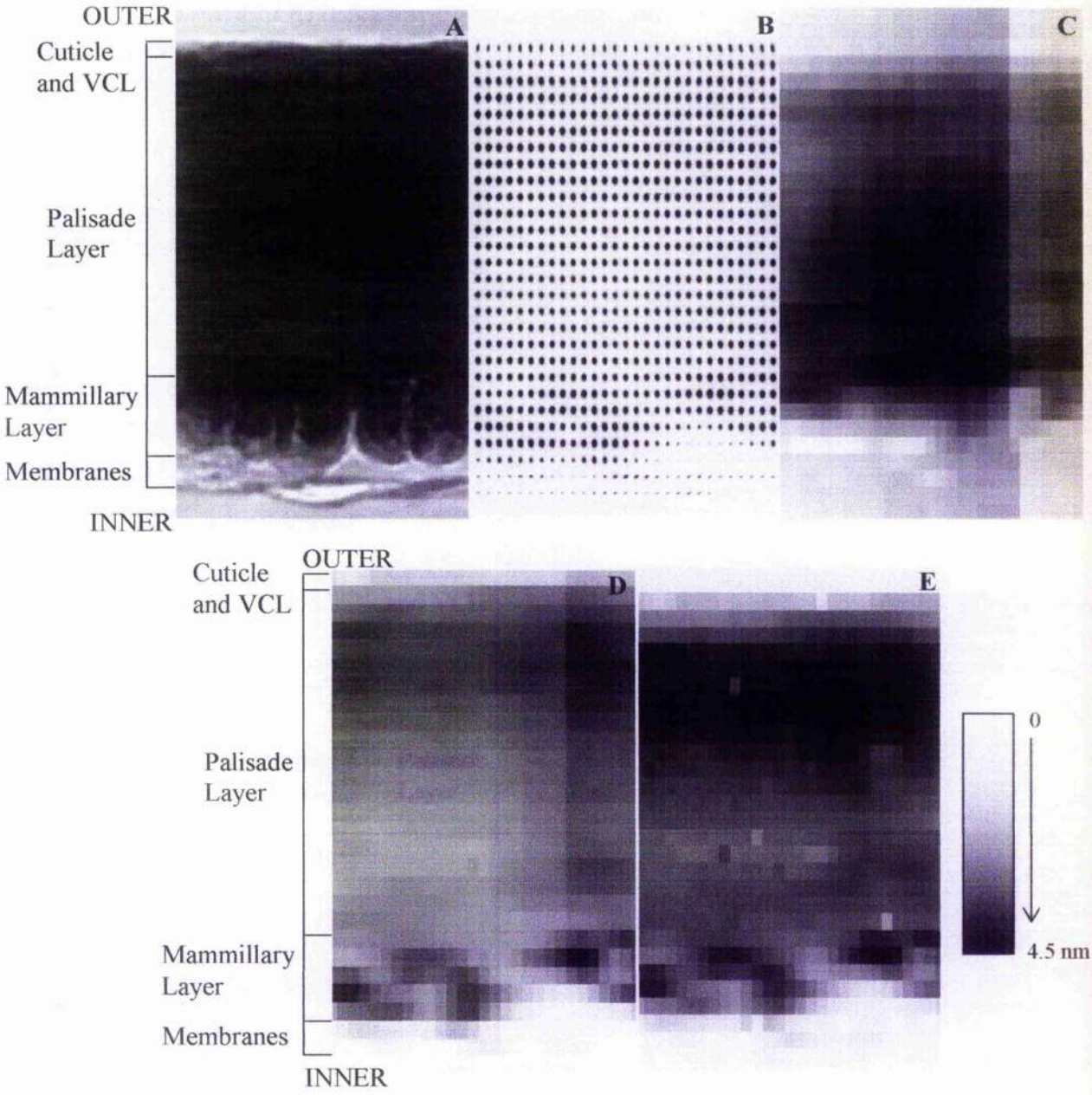

Figure 3.8 Two-dimensional maps produced from the data collected at ID18F from an abnormal eggshell. (A) X-ray transmission image. (B) Composite of the SAXS patterns from the section scanned. (C) Total scattering intensity map from each point on the two-dimensional scan, where the greater the intensity the darker the tone. (D) Invariant map, where the greater the value the darker the tone. (E) Size dimension map showing size variation through the different layers. The darker shades correspond to a larger size value. Note that in C and D there is an increase in the intensity, approximately three quarters into the scan; this is an artefact, due to the beam refill at the synchrotron. However, this is not apparent and does not alter the size dimension map (E).

Figure 3.8C shows areas where the total scattering intensity is greater (darker tones) than in others (lighter tones). However, unlike the normal eggshell, there is no obvious banding pattern within the different layers apparent in this figure. This indicates a lack of order of the structure in this sample. The two-dimensional invariant map (Figure 3.8D) also shows regions where the values for the invariant are larger and so are producing darker regions on the map. This is most apparent in the mammillary layer and outer palisade layer. However, similar to the previous map the darker regions are separated with lighter regions, and there is no obvious banding of tone observed, which differs from the maps of the normal eggshell scan (Figure 3.4C, D). Analysis of the size dimension map (Figure 3.8E) reveals random size dimension changes within the layers of this type of eggshell, for instance within the mammillary layer, there is no distinct banding. This suggests that there is a lack of structural order in the initially deposited layers. The size values from three different vertical scans have been plotted and shown on a linear graph in Figure 3.9. All three repeat scan measurements show similar trends in size dimension within the different regions.

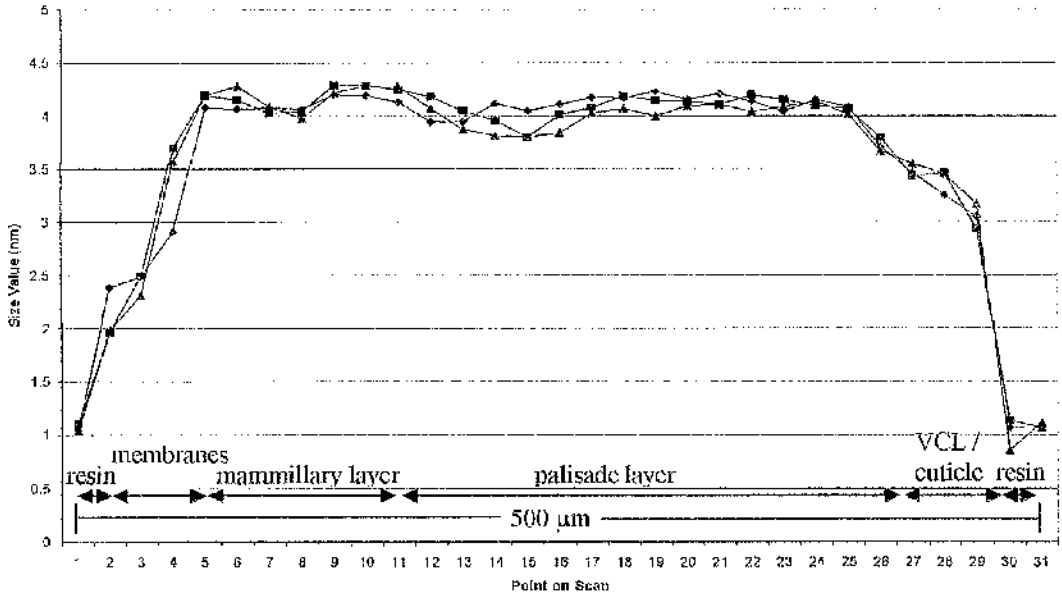

Figure 3.9 Measurements of the smallest dimension of the scattering objects from three scans at different areas from within an abnormal eggshell section. The scans start at the inner membrane and finish at the outer surface cuticle. Resin measurements are also included at the beginning and at the end of the scans.

According to this figure, most of the size values in abnormal eggs are between 3.7 – 4.3 nm, which is marginally larger than those obtained for the normal eggshell.

The invariant of the scattering intensity at each scan point was also determined for the abnormal eggs and the values obtained from one of the vertical scans are shown in Figure 3.10. According to this figure, there is a large increase in the intensity at point 6 on the scan corresponding to the centre of the mammillary layer. There is then a decrease from point 6 to 8 and then a steady increase again to the exterior of the eggshell. There is a slight difference in the scale between the two invariant graphs from the normal and abnormal eggshells that are displayed in Figures 3.7 and 3.10 respectively; this was due to the different

exposure times for each sample. The change in exposure time was required in order to complete the scan since beamtime was limited. However, even though the scale is different on each figure this can be discounted as the overall trend is similar.

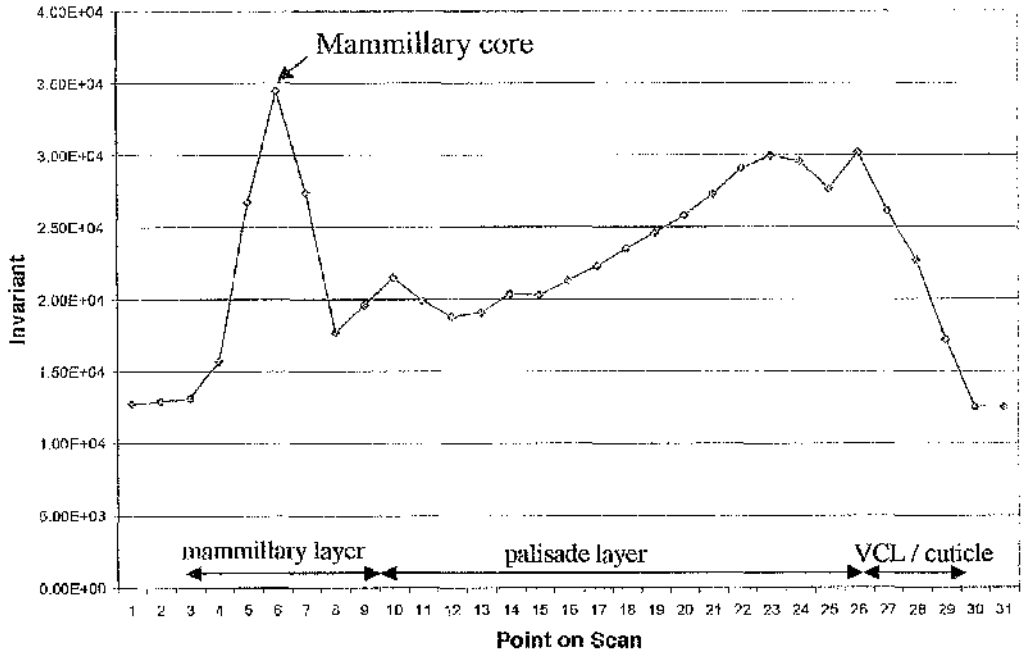

Figure 3.10 The invariant of the scattering intensity for an abnormal eggshell at each of the points on the vertical scan. The sample length was 500 μm for each vertical scan.

3.3.3 ID13 - 110 μm Section of Normal Eggshell

A light microscope image of the mammillary layer taken from one of the additional samples of the normal eggshells is shown in Figure 3.11A. The section that was scanned using a 1 μm beam is depicted by the red box, and the composite of the corresponding scattering patterns taken over this section are shown in Figure 3.11B. The composite shows regions within the mammillary layer that have a greater scattering signal compared to other regions.

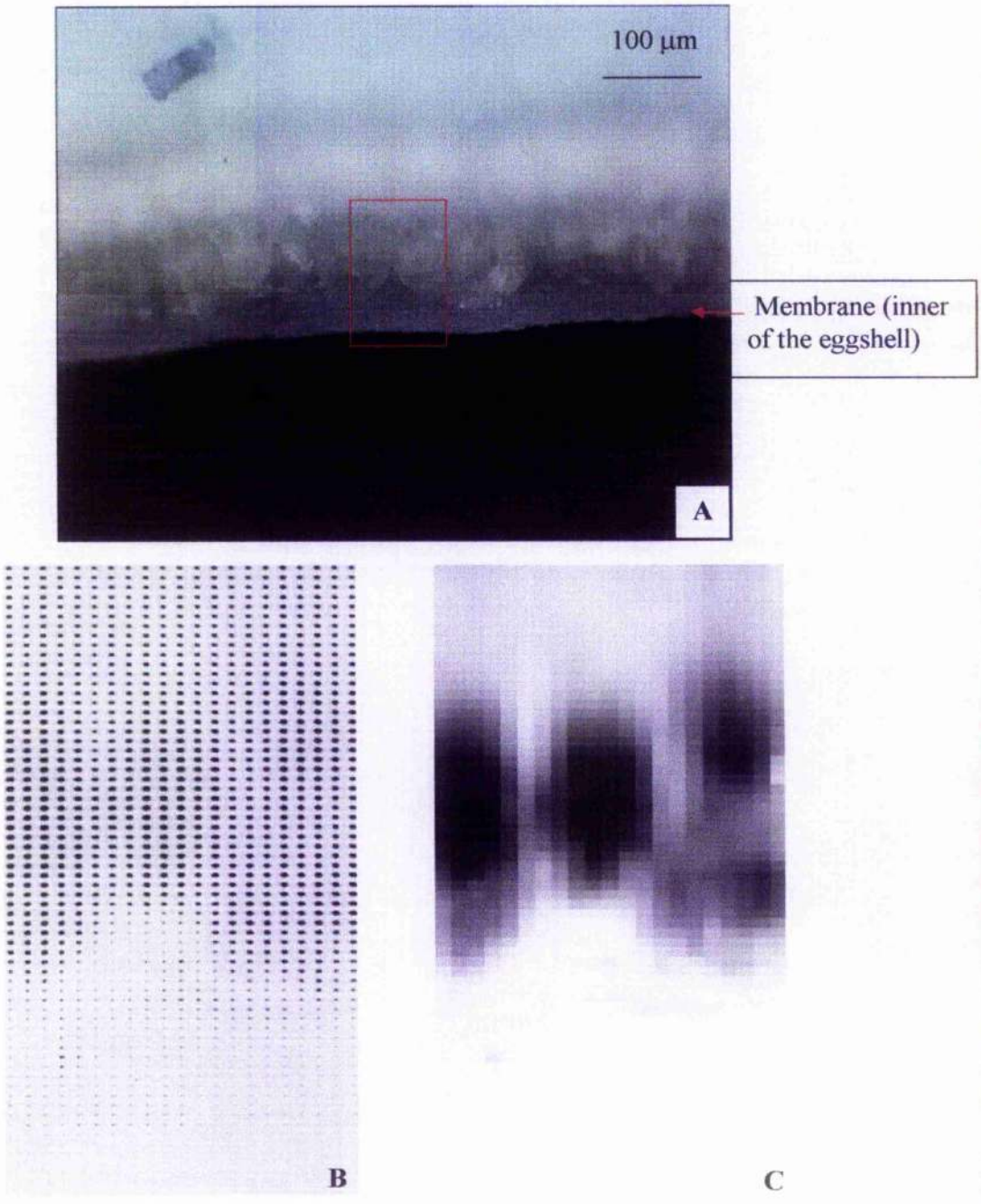

Figure 3.11 Two-dimensional data collected at ID13 of a 110 μm thick normal eggshell. (A) Light microscope image, where the area highlighted in red is the mammillary region of the eggshell that was scanned. (B) Composite of the scattering patterns from the section of the mammillary scanned. The area scanned was 130 μm vertically at 2 μm intervals and 100 μm horizontally at 5 μm intervals. (C) Total scattering intensity map relating to the mammillary layer.

The total intensity of each scattering pattern was measured and the values were used to produce a two-dimensional map of the total scattering intensity (Figure 3.11C). The regions of greater scattering signal seen in the composite image correspond to the darker tones at specific regions on the total scattering intensity map, and are likely to correspond to the mammillary core. This is in agreement with the observations obtained at beamline ID18F, Figures 3.7 and 3.10. This effect is most likely the result of specific nanofeatures within this region, arising from the high concentration of proteins associated with the mammillary cores (Fraser *et al.*, 1998). This would cause electron density contrast with the inorganic portion, and thus an increase in the scattered X-rays.

3.3.4 ID13 – 50 μm Section of Normal Eggshell

Figure 3.12A shows two mammillary knobs attached to the membranes. This area was scanned using microfocus SAXS and the composite of the SAXS patterns are shown in Figure 3.12B. Areas of greater scattering intensity can be observed in the central region of the mammillary knobs in this figure. X-ray transmission measurements were used to produce the two-dimensional map shown in Figure 3.12C. The mammillary knobs are lighter especially the central part compared to the membranes, indicating that X-ray transmission through this region of the mammillary layer is lower. The corresponding total scattering intensity map, shown in Figure 3.12D, confirms that the greatest intensity is seen in the centre of the mammillary knobs.

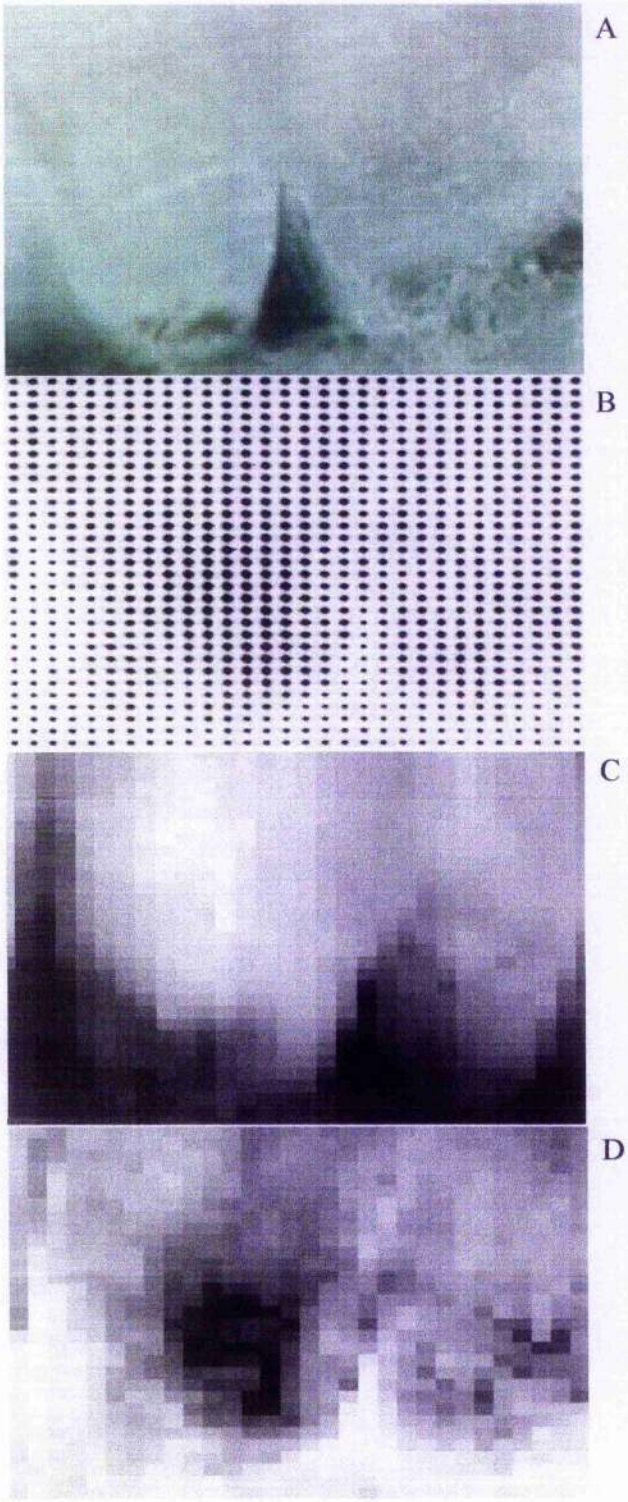

Figure 3.12 Two-dimensional data collected at ID13 of a 50 μm thick normal eggshell. (A) Light microscopy image of the region scanned on the mammillary layer. (B) Composite of the SAXS images obtained over the scanned region. The region scanned was 60 μm vertically at 2 μm intervals and 115 μm horizontally at 4 μm intervals. (C) Transmission image composed of measurements taken at corresponding points where the scattering patterns were taken. (D) Total scattering intensity map from the region scanned.

3.4 Discussion

The structural characteristics of a biomaterial at each length scale are organised in order to optimise the overall functional properties of the material. The eggshell is composed of distinct layers each of which has a series of proteins distributed within, which are thought to influence the growth and formation of the calcium carbonate crystals investigated through *in vitro* studies (Gautron *et al.*, 1996; 1997; Dominguez-Vera *et al.*, 2000; Hincke *et al.*, 2000; Fernandez *et al.*, 2004). The relationship between the proteins and the inorganic portion is an important aspect to understanding the mineralisation process, since the proteins are thought to play a significant role on nucleation, crystal growth and morphology and so influence the resulting composite. The principles of the mineralisation process may be applied to novel systems through biomimetic processes, which has been discussed previously (Heuer *et al.*, 1992; Arias and Fernandez, 2003) and through studying the formation of mineralised shells (Arias and Fernandez, 2003). Therefore, information regarding the structure at different length scales and protein interactions is required in order to understand biomineralisation events. X-ray diffraction studies of intact eggshell structure have focused on examining the microstructure of eggs in terms of the preferred orientation of the crystals (Cain and Heyn, 1964; Sharp and Silyn-Roberts, 1984; Rodriguez-Navarro *et al.*, 2002). In this chapter, microfocus SAXS techniques at beamlines ID18F and ID13 at the ESRF were used to provide detailed novel information relating to the nanostructural organisation of the eggshell.

The transmission images obtained at ID18F from normal eggshells in the current work served to highlight microscopic features of the eggshell, and drew particular attention to the mammillary layer (Figure 3.4A). Within the main bulk of the calcified layer microscopic features were less apparent. A similar result was seen with the transmission images obtained

from the abnormal eggshells, where microscopic features were again most apparent at the level of the mammillary layer (Figure 3.8A).

The scattering composite images and total scattering intensity maps obtained using μSAXS indicated that there is a greater degree in variations of scatter at specific layers within the eggshell, which represent differences in the nanostructural organisation (Figure 3.4B, C and 3.8B, C). This important observation could relate to the reported variation in chemical composition of the eggshell matrix, as previously highlighted in section 1.5.4 and Figure 1.12.

Gautron *et al.* (1997) examined the uterine fluid collected at the initial phase (6-9 hours after ovulation), rapid phase (14-18 hours after ovulation) and terminal phase (22-23 hours after ovulation), and found that the protein profiles changed considerably from one phase of shell formation to the next. The uterine fluid contains the precursors of the eggshell matrix proteins and in terms of function it has been suggested that several of these proteins have a direct role to play in directing crystal growth mechanisms (Nys *et al.*, 2004). It is therefore hypothesised that nanovoids or nanopores (absence of inorganic material) are formed in the eggshell as a result of these matrix proteins becoming embedded within the mineral phase during the shell forming process. Moreover, since the electron density contrasts between the inorganic and organic components are detectable using μSAXS, it is further proposed that the nanostructural changes observed throughout the shell thickness in the current work arise from the temporal and spatial changes in the composition of the organic matrix during shell deposition.

Based on this argument, the darker bands observed in the composite and total scattering maps of the normal eggshell presented in Figures 3.4B and C respectively, can be interpreted as the localisation of individual matrix proteins causing electron density interfaces for SAXS contrast, which in turn produces a stronger scattering signal. In support of this, it is interesting to note that the matrix proteins ovalbumin, lysozyme and ovotransferrin are most highly concentrated in the mammillary layer of the eggshell (Panheleux *et al.*, 1999). The specific localisation of these proteins could therefore be responsible for the darker banding observed in the maps associated with this specific region of the eggshell. The concentration of ovocalyxin-32, in contrast, is known to increase at the terminal phase of formation (Gautron *et al.*, 2001b) and so the unique distribution of this protein could contribute to the darker banding in the maps associated with the outer palisade region.

The composite image from the abnormal eggshell (Figure 3.8B) shows regions within the mammillary layer that have a greater scattering signal, although the banding effect seen with the normal eggshell is absent. There are also regions of darker tone within the mammillary layer seen on the total intensity map, implying that the mammillary layer within the abnormal eggshell is structurally disordered at the microscopic level. Whilst this was not confirmed in the current study, a disruption of the ultrastructural organisation of the mammillary layer has previously been reported for this type of abnormality by Solomon (1991).

The absence of banding in the different layers of the abnormal eggshell suggests a lack of cohesion throughout the thickness within this type of eggshell; this is particularly obvious in the two-dimensional maps shown in Figure 3.8. Therefore, it is reasonable to suggest that the structural organisation of abnormal wrinkled eggs has been severely disrupted at all

length scales due to a change in the normal expression and distribution of matrix proteins whilst this eggshell was being formed in the shell gland.

Extracting information relating to the size of the scattering object is essential in order to provide details about the nanostructure of the material being examined (Fratzl *et al.*, 1991; Glatter, 1991; Fratzl *et al.*, 1996a; Gupta *et al.*, 2003; Hiller and Wess, 2006). Analysis of the size dimensions map associated with the normal eggshell (Figure 3.4E) indicates that within specific regions of the eggshell, there is distinct variation in the size of the scattering objects. Specifically, there is a darker band at the beginning of the mammillary layer and towards the outer surface of the eggshell. The size values obtained for normal eggshells in this study ranged between 3.5 – 4 nm, with the biggest difference in the size values occurring at the mammillary/palisade layer interface. This region also produced the strongest SAXS signal indicating that proteins in this location may act as X-ray lucent voids. The change in pore size observed at this location may therefore correspond to an abrupt alteration in the complement of proteins being expressed as the slow phase is superseded by the more rapid phase of calcification.

Transmission electron microscopy has previously been used to illustrate that the organic matrix is most highly concentrated in the mammillary cores (Fraser *et al.*, 1998). These authors also found that the morphological appearance of organic matrix changed throughout the palisade layer depending on the age of the bird laying the egg and that this in turn affected the quality of shell produced. At the beginning of lay (24 weeks of age), Fraser *et al.* (1998) found that the inner palisade was found to have fewer vesicles and was more fibrous compared to the outer palisade, which was mainly vesicular in nature. At the end of lay (72 weeks of age), all three palisade regions examined revealed an increase in the number

of matrix vesicles/10 cm^2 compared to both the beginning and middle (46 weeks) of lay, and shell quality was notably poorer. Whilst it is not immediately obvious how to relate changes in morphology to the nanostructural variations presented in the current study, both types of observations do add support to the premise that the organic matrix component of the eggshell has a direct effect on the quality of the egg produced.

Panheleux *et al.* (2000) reported that the total protein content in eggshells was not affected by the age of the hen laying the egg. However, these authors found that the expression of individual proteins does vary in eggs from aged hens which characteristically produce poorer quality shells. Unfortunately, μSAXS analysis cannot distinguish between the voids formed from individual matrix proteins. The size dimensions presented in Figures 3.6 and 3.9 for the normal and abnormal eggshells respectively, relate to the overall protein voids within the eggshell sample at each specific location. Thus, if the overall protein content of the eggshell matrix remains the same in eggs of differing quality then it is perhaps not surprising that the overall size dimension data generated from the normal and abnormal eggshells were comparable. Whilst the overall deposition of protein within the different layers of the eggshell may not be altered within the abnormal eggshell, the protein voids in each layer could become misaligned due to the underlying membranes being malformed and wrinkled. This effect could offer some explanation as to why there was a lack of distinct banding of tone in the two-dimensional maps for the abnormal eggshells (Figures 3.8 C, D and E) compared to the normal eggshell samples (Figures 3.4 C, D and E).

A more detailed microfocus X-ray scattering analysis of the membranes and mammillary layer of the normal eggshell was undertaken at beamline ID13. Examination of all the two-dimensional maps produced from the data collected at beamline ID13 confirms that there are

variations in scatter seen within regions of the mammillary layer, specifically in the centre of the mammillary knobs. Subsequent analysis of these results again confirmed that the scattering signal is likely to be associated with changes in the nanoporosity arising from the embedded proteins within the calcified matrix, with size dimensions in the range of 3 – 5 nm. The scattering variations observed within the mammillary layer as depicted in Figures 3.11B and 3.12B could be a result of localised alterations in protein deposition or type of protein within the mammillary cores. This suggestion is consistent with the current literature, which states that several matrix proteins have a direct role in initiating and directing crystal growth during the initial stages of shell formation (Panheleux *et al.*, 1999; Hincke *et al.*, 2000; Gautron *et al.*, 2001a).

The ability to illustrate that there is a variation in the nanostructural organisation of the eggshell is an important addition to our knowledge of the eggshell structure. In an analysis of texture by Perrott *et al.* (1981), it was found using TEM and electron diffraction that the calcite columns within the palisade layer consisted of crystallites of diameter 20 – 30 μm. Moreover, Cain and Heyn (1964) found the mineral particle sizes (crystal sizes) to be 200 μm by using the number of diffraction spots in the rings to determine the sizes. The overall sizes of the calcite crystals are therefore known to be too large for accurate detection using μSAXS, because the size of the beam is smaller than the size of the crystal, and the objects are beyond the size range detectable using SAXS. The measurements that are presented here therefore constitute detail on the nanoscale and represent a unique insight into the relationship between inter and intracrystalline proteins found in many types of biominerals. The size of the objects identified in this work is commensurate with the size of many globular proteins, and therefore it is possible that the embedded proteins provide the scattering interfaces while the lower contrast proteins appear as a void in the high density

calcite. It cannot be unequivocally confirmed from SAXS results alone that these voids account for the scattering signal; the presence of nanocrystallites of calcite by the inversion principle could also produce a similar effect. But at the time of writing there is no literature and evidence to show this.

In conclusion, microfocus SAXS can be used to provide novel information about the nanostructural properties of the eggshell, which can in turn be related to existing knowledge at other length scales and to existing information relating the chemical composition and organisation of the organic matrix component of the eggshell. The two-dimensional maps produced in this study have confirmed that nanostructural changes exist throughout the eggshell thickness and that in abnormal eggshells this nanostructural organisation becomes severely disrupted.

The next chapter of this thesis concentrates on bulk SAXS analysis specifically designed to investigate the nanostructure of eggshells expelled at different stages of gestation to determine if it is possible to detect changes in the nanostructural organisation of the forming eggshells, which correspond to specific events in the shell forming process.

Chapter 4

Nanostructural Examination of Powdered Eggshells at Different Stages of Gestation using X-ray Diffraction and Small Angle X-ray Scattering

4.1 Introduction

The mechanical properties of biomaterials results from the hierarchical organisation at each length scale (Aizenberg *et al.*, 2005). The fully developed eggshell is a highly ordered structure (Parsons, 1982; Solomon, 1991) and is composed of five different layers. Using a combination of techniques, such as scanning electron microscopy (SEM), X-ray diffraction and small angle X-ray scattering, information from micron through to nanometer level of detail can be obtained about the eggshell. The ultra- and microstructure of eggshells have been studied extensively and in the previous chapter, microfocus SAXS was used for the first time to provide information at the nanometer length scale. Specifically, the size and arrangement of nanovoids were found to vary through the eggshell thickness and in visually poor quality eggshells the nanostructure was clearly disrupted. The preparation time and availability of beamtime at the ESRF limited the number of samples that could be analysed in detail using high resolution microfocus SAXS instrumentation.

The NanoSTAR is an in-house X-ray system; therefore, is much more readily available and has proved particularly useful in providing information about the nanostructure of other types of biominerals such as bone (Hiller *et al.*, 2003). The NanoSTAR instrumentation can be used for both X-ray diffraction and SAXS data collection depending on the sample to detector distance. In order for average measurements such as size and shape of the structural features within bulk samples to be obtained, this instrumentation simply requires the samples to be powdered. This has certain benefits, particularly when larger numbers of specimens

are being compared. The main aim of this chapter was to establish what information this instrumentation can provide about the nanostructural organisation of the eggshells.

Solomon (1991) used scanning electron microscopy to describe the temporal and spatial changes in the ultrastructural organisation of eggs that were prematurely expelled from the oviduct at different stages of gestation. Gautron *et al.* (1997) was able to expel eggs more precisely at 8, 10, 12, 14, 16, 18, 20 and 22 hours by timing the preceding oviposition then administering intravenously a prostaglandin injection to the hen after that number of hours had elapsed. Eggs which have been prematurely expelled from the oviduct in this way could provide a useful experimental model in which to compare the nanostructural changes at different locations in the eggshell thickness where bulk measurements are employed, since the average measurements would be expected to vary in relation to how much of the final structure is present.

In this chapter, variations in the nanostructure of the eggshell at different stages of gestation were therefore compared using the NanoSTAR facility described in section 2.9.1. Both X-ray diffraction and SAXS capabilities of this instrumentation were used to analyse the powdered samples of eggshell material. The opportunity to repeat the X-ray diffraction analysis at station 14.1 at the SRS Daresbury Laboratory subsequently became available, which enabled shorter exposure times for data collection and diffraction patterns of greater intensities to be obtained. The information obtained from each type of scattering is discussed in relation to the inter-relationships between the organic and inorganic components of the eggshell and the variation in nanostructural organisation previously described in Chapter 3.

4.2 Materials and Methods

4.2.1 Egg Source

Eggs from ISA (Institut de Sélection Animale) brown hens were prematurely expelled at different points of gestation by administration of a 100 µg prostaglandin injection (Gautron *et al.*, 1996; 1997) at 8, 10, 12, 14, 16, 18, 20 and 22 hours after the preceding oviposition. These procedures were carried out at INRA, Tours, France. Duplicate eggs from each point of gestation were then sent to the UK for ultrastructural assessment to confirm the stage of shell formation.

4.2.2 Ultrastructural Assessment using SEM

1cm^2 sections from each expelled egg were removed from the equator using a diamond tipped circular saw and mounted onto aluminium stubs using conductive silver paint in such a way that the forming surface faced uppermost. Each specimen was then coated with gold palladium for 4 minutes using an Emscope sputter coater SC500 (Ashford, Kent, England). The specimens were subsequently observed using an Hitachi S570 scanning electron microscope at 15 keV.

4.2.3 X-ray Diffraction and SAXS Data Collection

Initial X-ray diffraction and SAXS analyses of the samples were carried out on the NanoSTAR (see subsection 2.9.1). Samples were powdered using a pestle and mortar and mounted between two sheets of ultralene within a sample holder. The eggshell data was corrected for the small scattering contribution from the ultralene by measuring the ultralene with no sample present and subtracting it from the data after corrected for transmission. The sample to detector distance was 0.22 m for X-ray diffraction studies and 1.07 m for SAXS;

the wavelength of the incident radiation was 1.54 Å. The samples were exposed for 2 hours at the X-ray diffraction configuration and 3 hours at the SAXS configuration, each measurement was repeated three times. Additional sections of approximately $1cm^2$ were powdered, then mounted between two sheets of mica on a slide and examined by X-ray diffraction at station 14.1, SRS Daresbury Laboratory (described in subsection 2.9.2). At station 14.1, X-ray diffraction data was collected using an ADSC Quantum 4R CCD detector with a sample to detector distance of 60 mm and the wavelength of the incident radiation was 1.488 Å. The samples were exposed for 1 s, and each measurement was repeated three times. The two-dimensional data were radially integrated through 360° to produce one dimensional linear profiles using in-house software. The 2θ range was 3.8 – 63.6° with a step size of 0.064°. The procedure for the analysis of the X-ray diffraction data and SAXS data is given in subsections 2.10.1 and 2.10.2 respectively.

Further samples of powdered eggshell material at 8, 14, 16 and 22 hours were analysed at the Technical University of Denmark. X-ray powder diffraction measurements were performed in Bragg-Brentano geometry (reflection mode) with a Philips PW1820/3711 diffractometer, equipped with a primary autodivergence slit and a secondary graphite monochromator, employing CuKα radiation (λ = 1.5418 Å). Data were collected in the 2θ range of 10 - 110° with a step size of 0.02° and a counting time of 5 seconds per step.

Rietveld refinements (Rietveld, 1967; 1969) were performed with WINPOW, a locally modified Windows version of the LHMP program (Howard and Hill, 1986). The program performs a full pattern fitting, where parameters for reflection profiles, unit cell, background, overall scale factor, 2θ zero-point and atomic coordinates, thermal movements and occupancies are fitted in a least-squares procedure. Profiles were fitted with a Voigt

function, which allowed for an estimation of the average crystallite size. This study was carried out in order to compare the results from the Rietveld method with the X-ray line broadening analysis.

4.3 Results

4.3.1 SEM Data

The SEM images shown in Figure 4.1 show the extent of shell formation at 8, 10, 12, 14, 16, 18, 20 and 22 hours of gestation. With the exception of Figure 4.1G these figures are all representative of the outermost surface of the forming eggshell. A number of individual mammillae can be observed in the eggshell obtained at 8 hours gestation (Figure 4.1A). Spherulitic crystal growth continues radially and upwards but is inhibited downwards because of the shell membranes, so that by 10 hours the individual mammillae almost completely obscure the underlying membranes (Figure 4.1B). In Figure 4.1C, the mammillary layer is almost complete, and in Figure 4.1D the palisade layer has began to form (14 hours). Figures 4.1E and 4.1F show the palisade layer at different stages of completion, this layer makes up the bulk of the eggshell. The transverse section of a complete eggshell is given in Figure 4.1G along with the approximate levels at which the other images were taken.

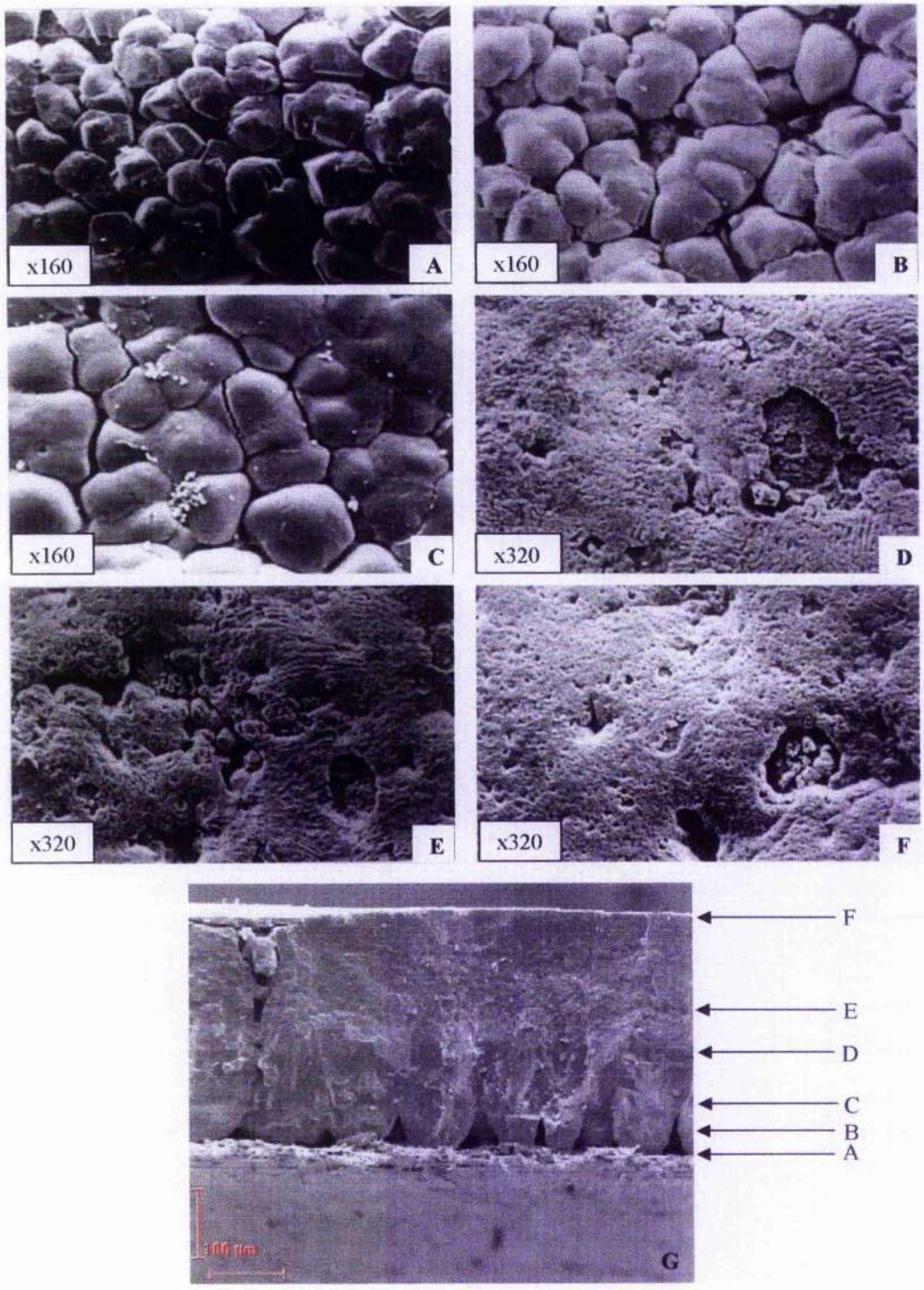

Figure 4.1 SEM surface images of prematurely expelled eggs. A = 8 hour, B = 10 hour, C = 12 hour, D = 14 hour, E = 16 hour and F = 22 hour sample. G is an SEM image of a transverse section of a complete eggshell, the arrows indicate at which point in the growth process would correspond to the surface images labelled above. Images courtesy of Poultry Research Group, University of Glasgow.

4.3.2 X-ray Diffraction Data from the Powdered Eggshell Samples

An example of the X-ray diffraction data obtained from station 14.1 at the SRS Daresbury Laboratory is shown in Figure 4.2. Further analysis was only carried out on this data set, since the diffraction patterns were of greater intensity than those obtained on the NanoSTAR. Within the diffraction rings, diffraction spots can be seen; one is highlighted in Figure 4.2 by the red arrow. This is an indication that these reflections are from large intact crystals. The breadth of the diffraction lines can be measured to obtain an estimation of the average crystallite size when they are less than ~100 nm in size (Lipson and Steeple, 1970). The diffraction rings correspond to the different reflections of the lattice planes in calcite. These planes can be identified based on their orientation in the unit cell using Miller indices (*hkl*) and are the reciprocals of intersection distances of the lattice planes (see subsection 2.3).

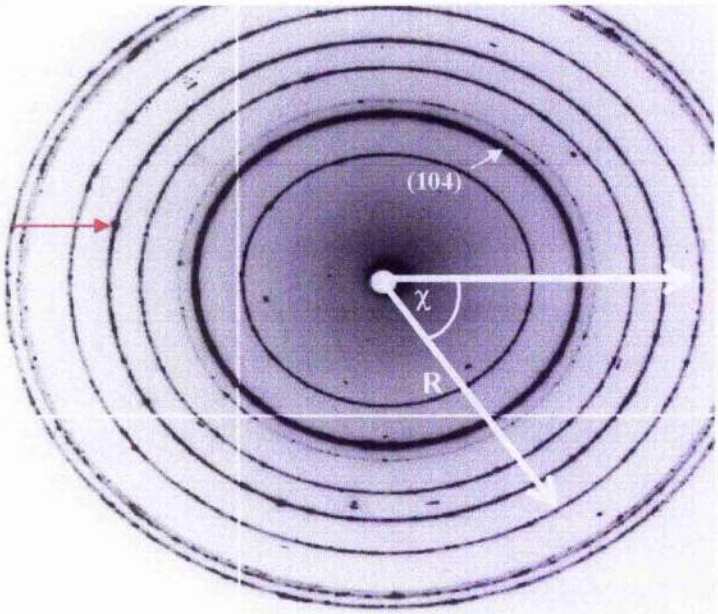

Figure 4.2 An X-ray diffraction pattern from a 22 hour powdered eggshell sample obtained on station 14.1, SRS Daresbury Laboratory. R is the scattering vector length and χ is the azimuthal angle to an arbitrary reference point. The d-spacing per pixel = 7.466×10^{-3} nm^{-1}.

The white arrows on the X-ray pattern in Figure 4.2 highlight the area which was subsequently integrated and converted to polar coordinates (R,χ) as shown in Figure 4.3, where R is the distance from the centre of the beam and χ is the azimuthal angle, (the angular position). This plot was then used to produce the linear trace required to measure the FWHM (described in subsection 2.10.1).

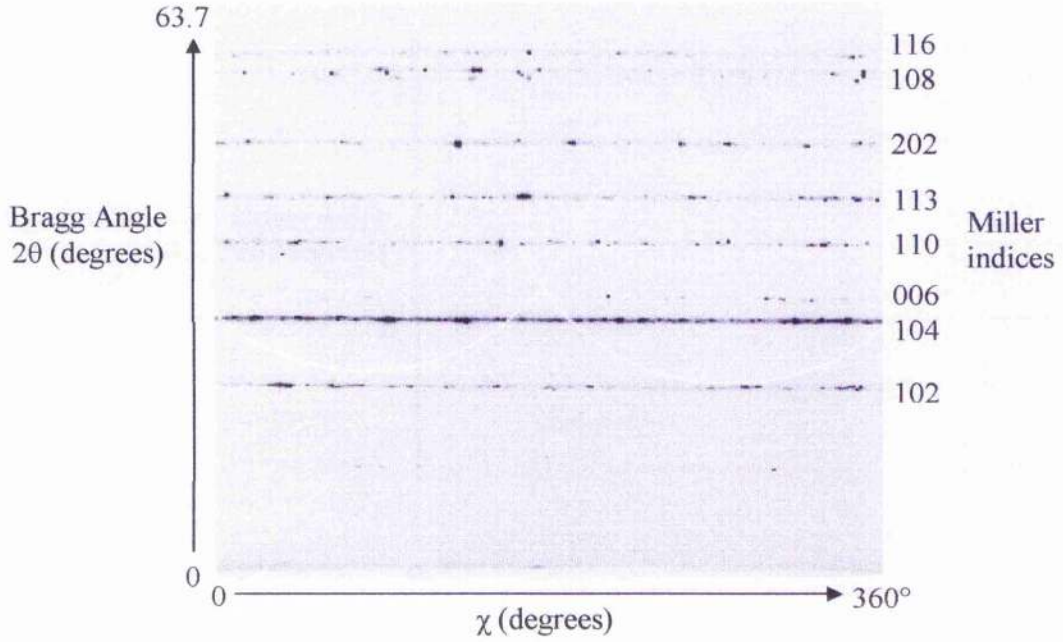

Figure 4.3 A polar plot showing the angular integration of the X-ray diffraction pattern. The reflection indexes for each corresponding lattice plane of calcite are shown on the left. The faint white lines are from the sectioned detector and should be discounted as it does not contribute to the data.

The intensity of the X-ray diffraction pattern was plotted as a linear profile in Figure 4.4, which shows the prominent (104) peak of calcite. This peak profile was used to calculate the FWHM measurements for each eggshell sample, which in turn was used to calculate crystallite size by entering the value into the Debye-Scherrer equation (Equation 2.5).

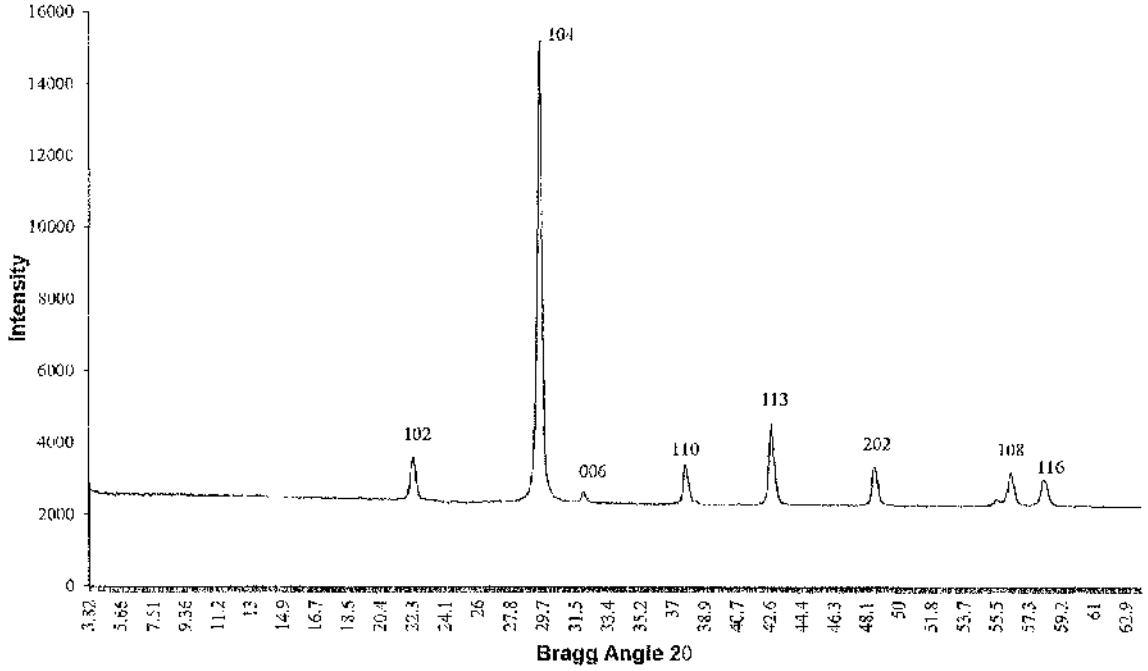

Figure 4.4 A linear intensity profile obtained from integrating the two-dimensional X-ray diffraction data. The prominent peak reflections are shown in the linear profile, and each peak is labelled with its respective (hkl) index for calcite.

The average crystallite sizes were deduced from analysis of the X-ray diffraction data using the FWHM from the (104) orientation peak seen on the linear intensity profile shown in Figure 4.4, where the greater the width of the peak the smaller the crystallite. The average

crystallite sizes that were obtained using the X-ray line broadening from each of the powdered eggshell samples examined in the group are represented in Figure 4.5.

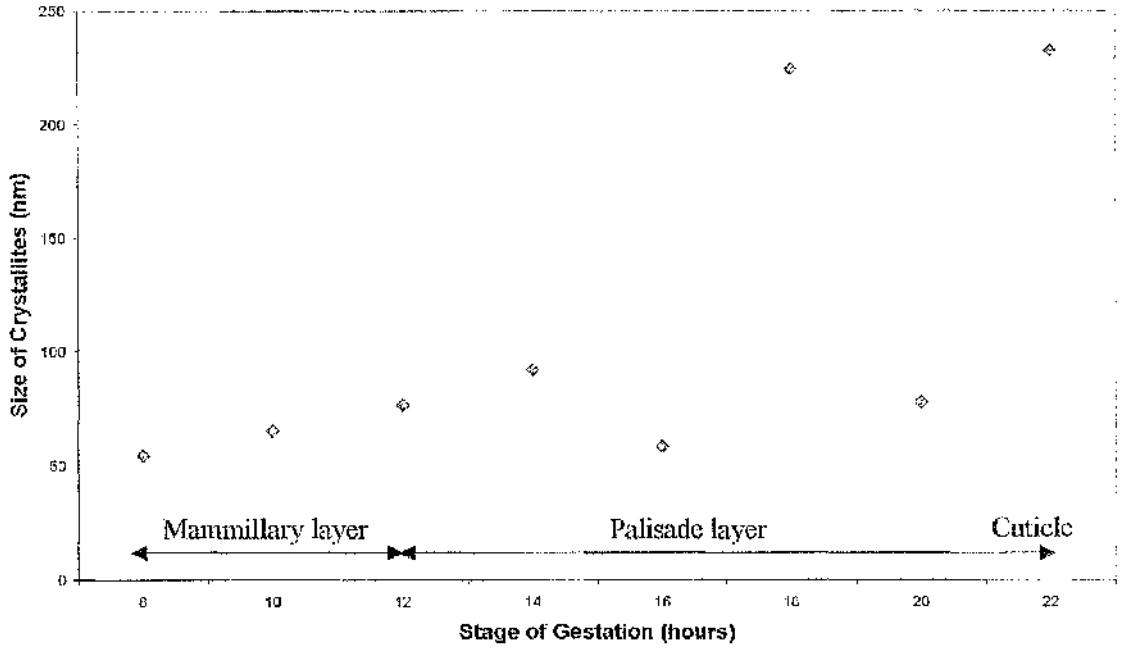

Figure 4.5 Graph of crystallite size obtained from measuring the X-ray line broadening at different accumulative stages of shell formation.

The size values obtained by measuring the broadening of the X-ray diffraction lines ranged from 54 – 232 nm. According to Figure 4.5, between 8 and 14 hours of gestation there is a gradual increase in the average crystallite size. This effect could result from there being an increase in the number of larger crystallite sizes as more of the mammillary layer and early stages of the palisade layer are being formed. After 14 hours of gestation however the average crystallite size seems to vary.

The observed pattern, the difference pattern, the refined background (red), and the positions of the Bragg peaks (blue) of the CuKα_1 positions produced from the Rietveld refinement with the diffraction data for the four eggshell samples are shown in Figure 4.6, 4.7, 4.8 and 4.9.

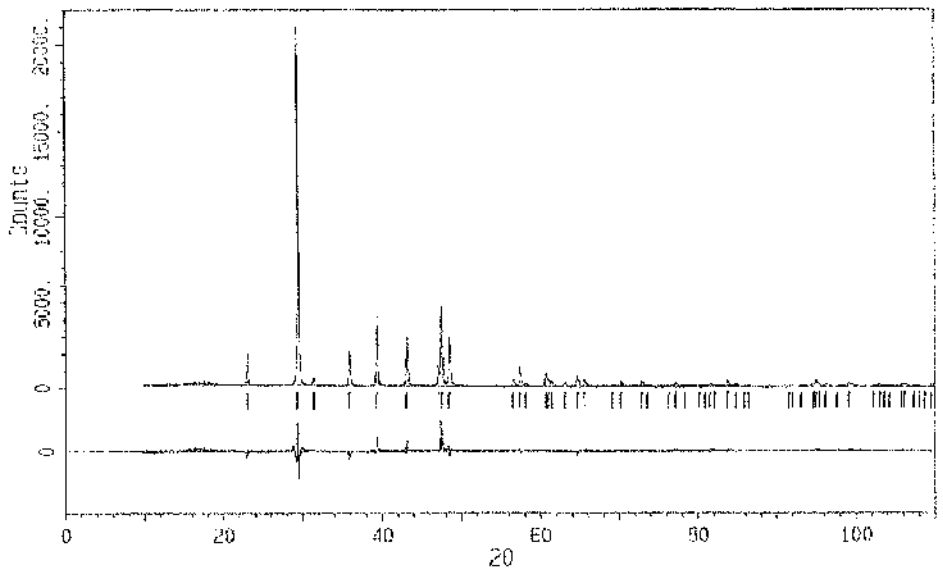

Figure 4.6 Rietveld profile fit to the diffraction data from the 8 hour eggshell sample.

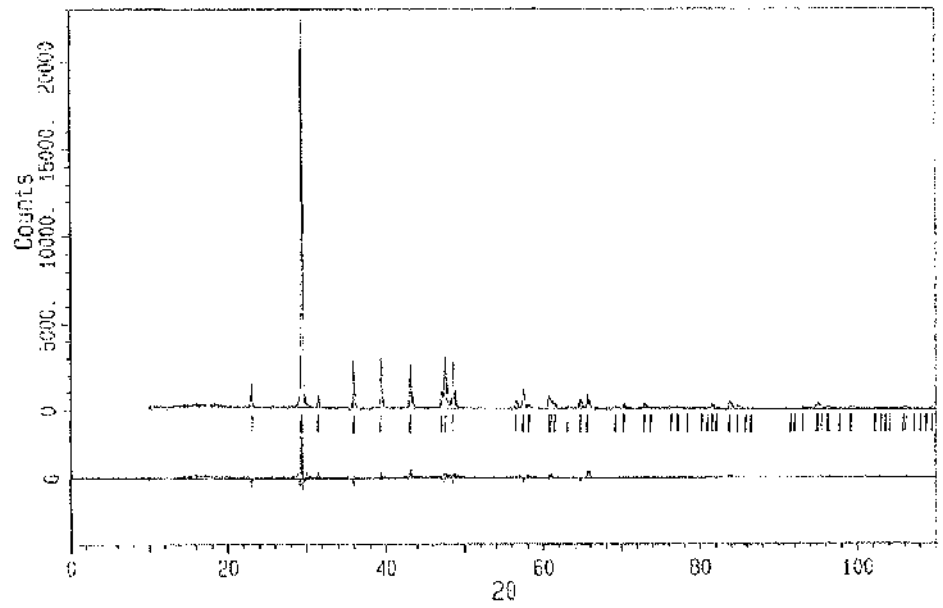

Figure 4.7 Rietveld profile fit to the diffraction data from the 14 hour eggshell sample.

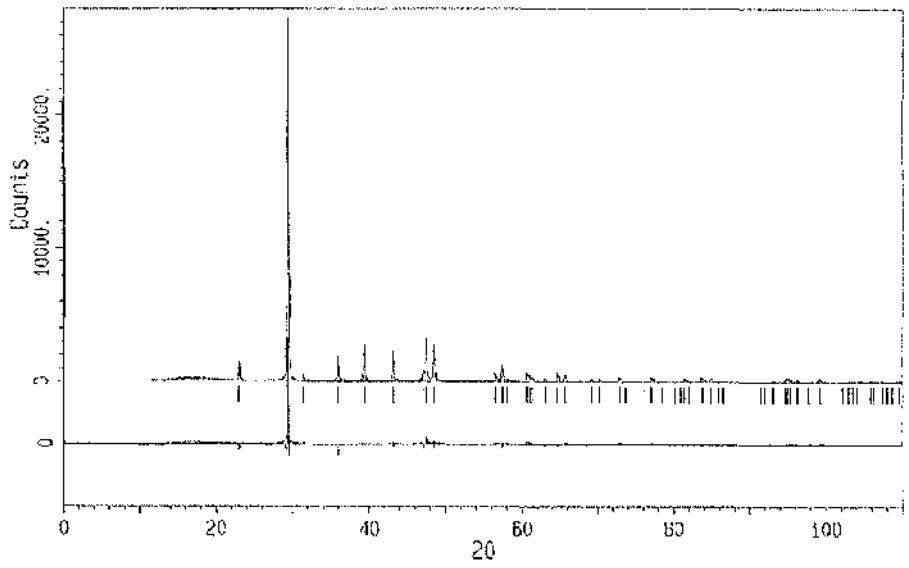

Figure 4.8 Rietveld profile fit to the diffraction data from the 16 hour eggshell sample.

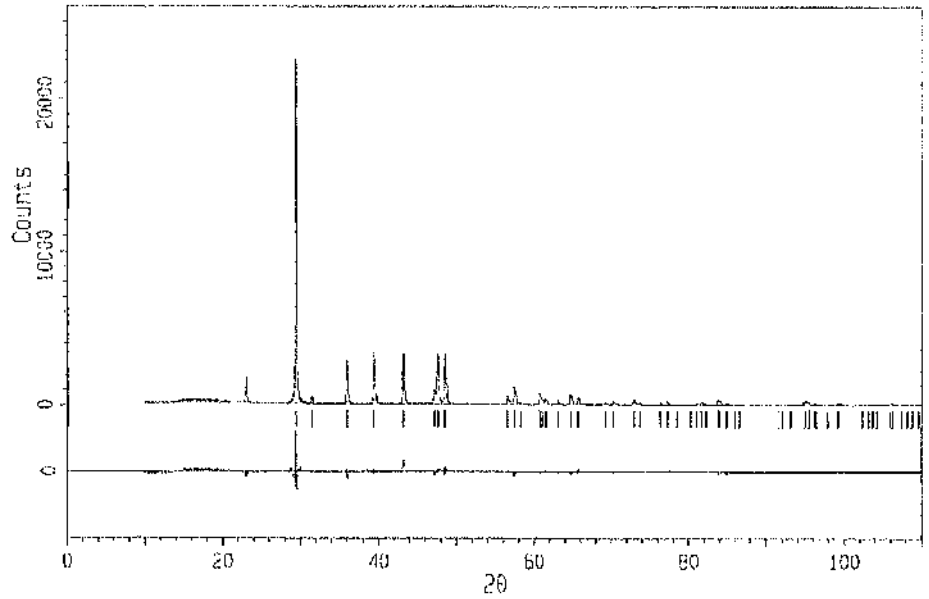

Figure 4.9 Rietveld profile fit to the diffraction data from the 22 hour eggshell sample.

The average crystallite size calculated using the Rietveld method was 90 nm, but varied from 75 nm at 8 hours, to 106 nm at 14 - 16 hours, and 75 nm at 22 hours, as shown in Figure 4.10. These results suggest that the crystallite sizes are in fact larger than the upper size limit for XRD analysis to be accurately detected, and also supports the hypothesis that the SAXS measurements presented in Chapter 3 represent nanostructural features within the calcium carbonate crystallites possibly arising from the interactions between the inorganic and organic components of the eggshell.

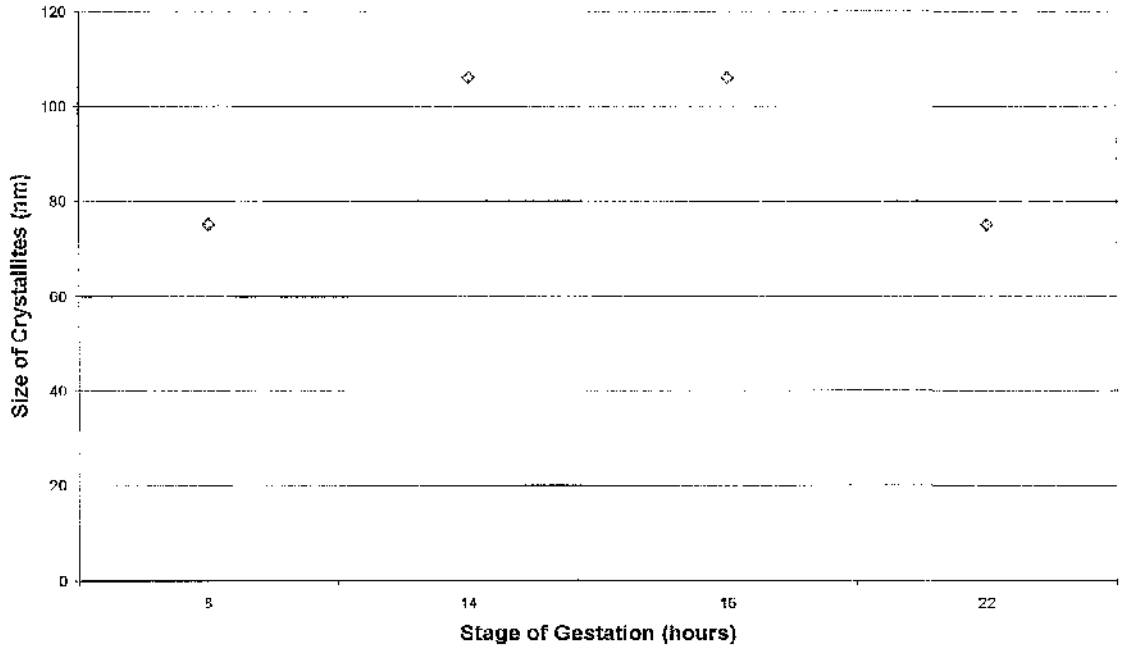

Figure 4.10 Crystallite size measurements from a subsection of the eggshell samples obtained using the Rietveld method.

4.3.3 Small Angle X-ray Scattering Data from the Powdered Eggshell Samples

A typical SAXS pattern obtained using the NanoSTAR from an eggshell expelled at 8 hours of gestation is shown in Figure 4.11.

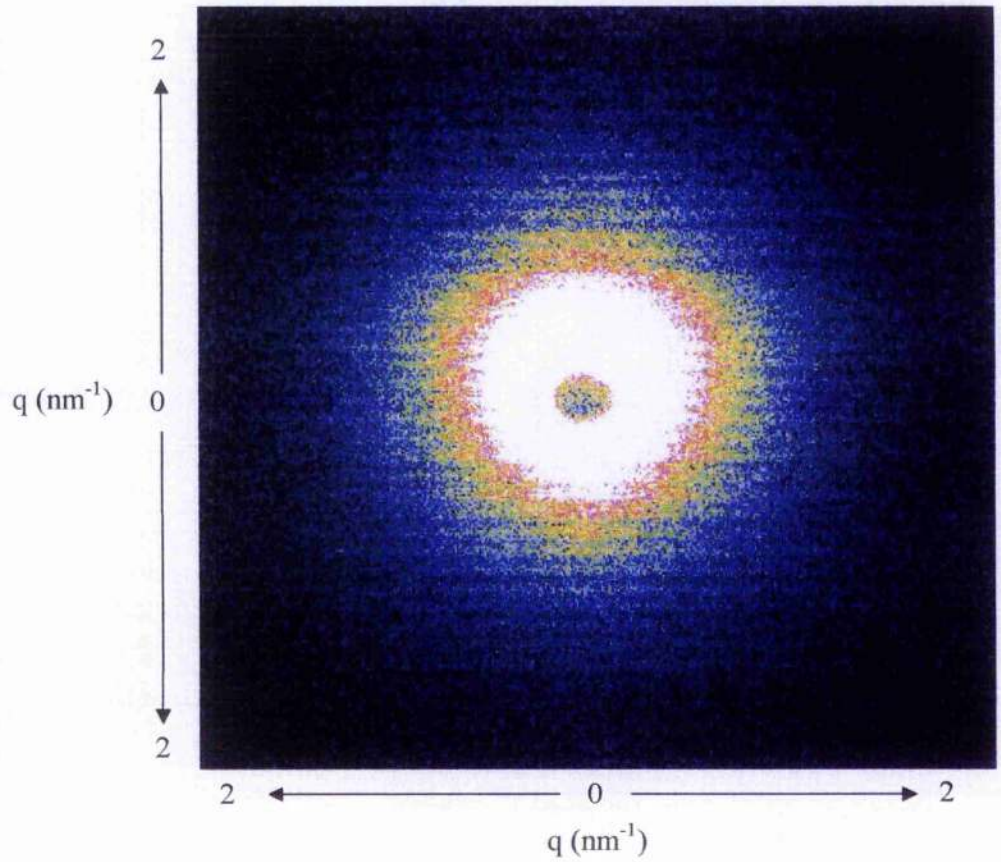

Figure 4.11 SAXS pattern from an eggshell expelled at 8 hours of gestation obtained using the NanoSTAR. 1 pixel corresponds to 0.02 nm^{-1} in q.

The two-dimensional data was integrated and plotted as Kratky plots ($I(q)q^2$ against q) as shown in Figure 4.12, where the shape of the scattering curve provides information about the shape of the scattering objects within the sample material.

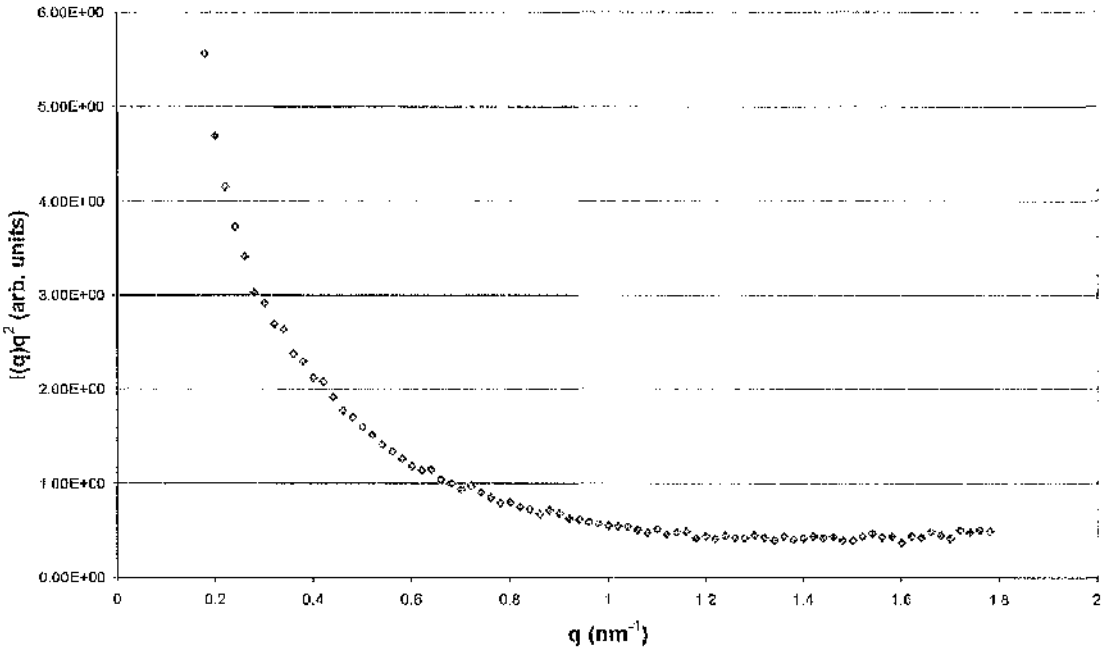

Figure 4.12 A Kratky plot ($I(q)q^2$ against q) from an 8 hour powdered eggshell sample. The linear profile is an indication of polydispersity of shapes of the scattering structures within the sample.

The linear profile of the scattering data shown on the Kratky plots corresponds to a Lorentzian type profile (Fratzl *et al.*, 1991; Wess *et al.*, 2000), which is considered to indicate polydispersity, i.e. a combination of different shapes and sizes of the scattering objects. The same result was found for all of the prematurely expelled powdered eggshell samples. Thus, no clear conclusion can be made about the exact shape of the scattering objects in the powdered samples since there is likely to be a combination of shapes that compose the scattering profile.

4.3.3.1 Feature Size Derived from SAXS

The size values obtained from the analysis of the data collected on the NanoSTAR are displayed in Figure 4.13. The size values obtained using powdered samples of eggshell from the different stages of gestation ranged between 5.7 – 7.2 nm with an average of 6.7 ± 0.5 nm.

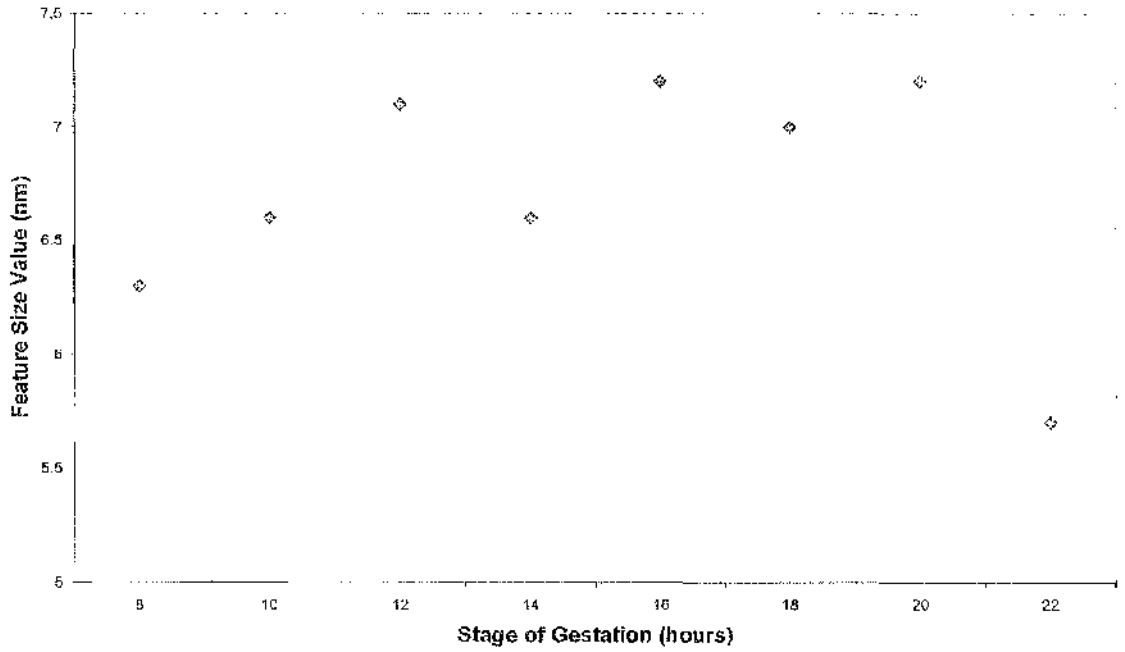

Figure 4.13 Size values obtained from the analysis of the SAXS data collected on the NanoSTAR, the samples were exposed for 3 hours.

These size values are an order of magnitude smaller than those determined using X-ray diffraction and are consistent with the SAXS size values reported in Chapter 3. The slight variation in the average size values with the stage of eggshell development shown in Figure 4.13 could correspond to the changes in nanostructure imposed by the expression of the different protein components of the eggshell matrix.

4.4 Discussion

A temporal and spatial variation in the inter-relationship between the inorganic and organic fraction of the eggshell would reduce the measurements of the coherent regions within the powdered material being examined using X-ray diffraction. From the broadening of X-ray diffraction lines, the size values obtained in this experiment ranged from 54 – 232 nm with a steady increase occurring until the 14th hour of shell formation. The unpredictable change in size value obtained thereafter could be explained by the knowledge that size, structural faults and lattice distortion of crystallites all contribute to line broadening in X-ray diffraction traces (Lipson and Steeple, 1970). This effect may also be cumulative, where the growth process of calcite in the eggshell could involve the formation of similar sized calcium carbonate crystallites being deposited on top of each other instead of forming a continuous calcite column, which extends through the entire thickness of the eggshell. Another possibility for the variations in size value obtained after 14 hours could be due to 'infilling'. The assumption that once calcium carbonate crystallites are deposited they are not altered could be incorrect; the surrounding bicarbonate and calcium ions may in fact be modifying the existing crystallites that have already been deposited, thus altering their size. Evidence of this effect has previously been observed at the ultrastructural level in the mammillary layer, where extra deposits of calcium carbonate form in the inter-mammillary spaces and give rise to the structural variant referred to as 'cuffing' (Solomon, 1991).

Comparable measurements were made on a subset of samples using the Rietveld method. The size values obtained using this method showed less variation and were between 75 – 106 nm. Full pattern fitting to the experimental diffractogram by means of Rietveld analysis (Rietveld, 1967; 1969) allows all reflections to be included. However, there are still some uncertainties with this method, particularly with large crystallite sizes and defects within the

sample will also add to the widths and complicate the interpretations similar to that of the X-ray line broadening method. X-ray line broadening and Rietveld fitting to powdered eggshell diffraction data are therefore much less suitable for use when a material consists of large crystallites of calcium carbonate, and this seems to be the case with the eggshell.

The calcium carbonate crystal sizes within eggshell that were obtained in recent studies (Rodriguez-Navarro *et al.*, 2002; Ahmed *et al.*, 2005) (see subsection 1.3.4) indicate that the size measurements determined in this chapter are from structural features that are at a smaller length scale. The size values obtained from the SAXS analysis in this experiment were between 5.7 – 7.2 nm, and are comparable to those presented in Chapter 3. One explanation for the different values between the SAXS and X-ray diffraction results could relate to the component of the structure that is being measured, for example crystallite sizes versus the dimensions of pore/voids within the crystallites. The size measurements obtained from the SAXS data are more likely to represent the pores/voids within the crystallites arising from proteins embedded within the different inorganic layers. In comparison, the X-ray diffraction measurements are likely to be from the coherent regions within the calcium carbonate crystallites or from an accumulation of individual crystallites formed on top of one another. In other words, the different size measurements obtained from these studies are dependent on the structural feature being examined. Thus, the likelihood that there are pores/voids within the calcium carbonate crystallites is the most convincing explanation for the size measurements that were produced from the analysis of the SAXS data.

The SAXS analysis showed that the average size of these nanovoids changed slightly in relation to the stage of eggshell development; this effect could be consistent with a variation in the spatial localisation of individual organic matrix proteins throughout the eggshell

thickness as described in Chapter 1, section 1.5.4. In other words, these analyses have indirectly provided further evidence that it is the embedded proteins causing nanovoids throughout the eggshell thickness.

The linear profiles displayed as Kratky plots produced from the SAXS data collected from the eggshell samples correspond to Lorentzian type curves, which give an indication of polydispersity. This data analysis of the shape determination of the crystallites has been used in bone studies (Fratzl *et al.*, 1996a; Wess *et al.*, 2001b). These results suggest that there is a broad range of sizes and shapes of scattering objects within the eggshell at the nanostructural length scale; therefore, no clear conclusion can be made about the exact shape of these features. Indeed, there may be no precise overall shape as it is the shape of the voids themselves which are being determined and these may be highly variable with no dominant shape.

In conclusion, the results from the work presented in this chapter indicate that the crystallites in eggshells are possibly too large to be examined using either X-ray diffraction line broadening or the Rietveld method of analysing X-ray diffraction data obtained from powdered specimens of eggshell. This confirmed that the most appropriate technique to investigate the nanostructure of eggshells is SAXS. SAXS can be used to investigate structural properties on a length scale range of between about 10 Å up to several thousand Å (depending on the X-ray source and configuration). The size measurements obtained in this chapter possibly correspond to nanopores/voids within the calcium carbonate crystallites arising from the presence of embedded proteins. The likelihood that the size measurements and the nanostructural changes within the eggshell are a result of the nanoporosity due to the embedded proteins is investigated further in Chapter 5. Here, the porosity of the eggshell at

the nanometer length scale is examined again using SAXS and mercury intrusion porosimetry on eggshells of different mechanical strengths.

Chapter 5

An Examination of the Nanostructure of Eggshells Exhibiting Different Mechanical Strengths

5.1 Introduction

A number of features are considered to be synonymous with eggshell quality, including eggshape, texture, cleanliness and soundness. Eggshell quality however is usually more precisely defined using a variety of methods and laboratory techniques, which can be broadly defined as being either traditional or novel (De Ketelaere *et al.*, 2004). Traditional methods of assessing eggshell quality have been extensively reviewed by Voisey and Hunt (1974) and Hamilton (1982), and include methods which either directly or indirectly assess the strength of the eggshell. The direct measurements include the quasi-static compression test where the strength of the egg is measured in a materials testing machine by compressing it between two flat steel plates at a constant speed until it breaks. Indirect measurements include measuring a parameter related to eggshell strength such as eggshell thickness and the eggshells specific gravity, which provides an estimation of the percentage of shell. Recently, Bain (2005) reviewed the more novel methods of assessing eggshell quality, which include the dynamic stiffness measurements (De Ketelaere *et al.*, 2002), microstructural studies (Rodriguez-Navarro *et al.*, 2002) and studies associated with the organic matrix component of the eggshell (Nys *et al.*, 2004). The dynamic stiffness measurement according to Dunn *et al.* (2005) and Bain *et al.* (2006) could be directly applied to improve eggshell quality in genetic selection programs, whilst the micro-structural and organic matrix related studies have significantly contributed to our understanding of how the inorganic and organic components of the shell interact and influence the mechanical properties.

There are a number of factors that are known to influence eggshell quality; these include genetics, nutrition, disease, management (for example housing, feeding program, temperature) and bird age. Eggshells of aged hens are known to decrease in strength (Hamilton *et al.*, 1979b; Potts and Washburn, 1983) but this is not simply associated with an age related decline in the thickness of the shell. Panheleux *et al.* (2000) for example, compared the organic matrix of eggshells from young and aged hens and found that whilst the total protein content of the eggshells did not change, the concentrations of specific individual eggshell matrix proteins (ovalbumin, ovotransferrin and ovocleidin-17) was increased in the eggshells from aged hens. These results suggest that a change in the composition of the organic matrix rather than the amount of matrix material present may have been responsible for the measurable differences in eggshell strength of eggs laid by young versus aged hens. An XRD study on the same group of eggs by Rodriguez-Navarro *et al.*, (2002) subsequently revealed that the eggshells laid by younger hens displayed only a single preferred crystal orientation, and that this was correlated to an increase in eggshell strength. The eggshells from the aged hens in comparison showed two preferred crystal orientations. In addition, crystallographic texture (preferred orientation of the crystal grains), thickness, and grain morphology was more variable in the eggs from the aged hens. It was suggested that these microstructural changes were due to the variations in protein content previously observed by Panheleux *et al.* (2000).

The effect of an induced moult on eggshell strength, crystallographic texture and the organic matrix were investigated by Ahmed *et al.* (2005) using similar techniques. These authors found that after moult, breaking strength increased, the average size of the calcite crystals decreased, but crystal orientation remained the same. In addition, these authors reported that there was an increase in the total organic matrix protein concentration and a variation in the

concentrations of individual proteins after the moult: OC-116 and OC-17 were found to increase, whilst ovotransferrin, ovalbumin and lysozyme decreased.

These two studies support the hypothesis that there is a direct relationship between the mechanical properties or quality of the eggshell and its microstructural organisation, and that the microstructure of the eggshell is in turn directly influenced by the protein components of the eggshell matrix. In Chapter 3, it was proposed that microfocus SAXS can be used to measure the nanoporosity arising from the presence and incorporation of organic material within the inorganic portion of the hen's eggshell. The aim of the work presented in this chapter was to examine if variations in nanostructure can be detected using SAXS in eggshells exhibiting different quality characteristics.

Nielsen-Marsh and Hedges (1999) investigated bone diagenesis using mercury intrusion porosimetry. Briefly, mercury intrusion porosimetry is a technique that uses non-wetting mercury to gain information regarding the pores within a material. Due to the non-wetting nature of mercury, high pressure is required in order to force the mercury into the smaller pores. The permeability and diffusivity properties of the material are related to the pore size, shape, arrangement and connectivity of the pores in the network, since the mercury intrudes from the outside of the sample inwards. This technique has been used in material and soil sciences to investigate porosity of the material; recent work includes studies of concrete (Pradhan *et al.*, 2005), paper (Moura *et al.*, 2005), pharmaceutical drugs (van Veen *et al.*, 2005) and soils (Gorres *et al.*, 2001; Pagliai *et al.*, 2004). In the context of this chapter, mercury intrusion porosimetry was used to test for differences in the pore size distribution in eggshells, which exhibited measurable differences in quality characteristics. The results

obtained by this method were then compared with the SAXS data to observe whether they support or extend the size range obtained for eggshell as reported in Chapters 3 and 4.

5.2 Materials and Methods

5.2.1 Egg Source

Eggs from Young and Aged Hens

100 eggs were sourced from a commercial producer; half were laid by hens at 35 weeks (young) and half by hens at 72 weeks (aged) of age. The eggs were checked for the presence of defects/cracks. Breaking strength measurements were only carried out on intact eggs. Breaking strength was measured by quasi-static compression. In brief, each egg was placed between large flat plates and compressed in an equatorial direction using a LRX materials testing machine (Lloyd Instruments, Fareham, Hampshire, UK) at a displacement rate of 5 mm/min. During the test and up until fracture, both the force and resultant displacement were monitored using a Nexygen MT Materials Test and Data Analysis Software (Lloyd Instruments, Fareham, Hampshire, UK). The maximum force (N) on the force displacement curve was taken as a measurement of the breaking strength. Further details of the quasi-static compression tests are given in Voisey and Hunt (1974). After removal of the egg contents, a 1 cm^2 section of each eggshell was cut from the equator using a diamond tip circular saw. 18 eggs from each age group were subsequently selected for analysis of nanoporosity using SAXS.

5.2.2 Preparation of Samples for SAXS

The eggshell samples were powdered and SAXS measurements were made from bulk samples; in other words, an average size measurement of the scattering objects was determined for each sample. The powdered samples were each mounted into a sample holder between two sheets of ultralene. The samples were then mounted into the sample chamber on the NanoSTAR and were exposed for 3 – 6 hours. In order to correct for the background, a negligibly low scattering signal measured from the ultralene windows alone was taken and subtracted from the scattering signal obtained from the samples. The samples in each of the individual data sets were exposed for the same amount of time to ensure that a direct comparison could be made within the group and that the scattering intensity was sufficient to provide a valid analysis. The wavelength was 1.54 Å and the sample to detector distance was 1.07 m. A detailed description of the NanoSTAR and its configuration is given in subsection 2.9.1.

5.2.3 Preparation of Samples for Mercury Intrusion Porosimetry

Four eggshells exhibiting either low or high breaking strengths (2 in each category) were selected for further analysis by mercury intrusion porosimetry. The method used is outlined in detail by Nielsen-Marsh and Hedges *et al.* (1999) and Hiller (2003). Briefly, approximately 1g was cut from each eggshell sample and freeze-dried; they were then placed in a penetrometer apparatus and examined in a mercury intrusion porosimeter (Micromeritics) at the University of Newcastle. This technique assumes that the sample contains cylindrical pores and the mercury penetration into these pores is determined by the capillary law shown in equation 5.1, where D is the pore diameter (nm), γ is the fluid surface tension (mJ m^{-2}), θ is the contact angle between the solid and fluid, and p is the applied pressure (pounds per square inch (psi)).

$$D = \frac{4\gamma \cos\theta}{p} \tag{5.1}$$

With this technique the pressure is increased continuously, and the mercury starts to fill the pores. As the pressure increases mercury can penetrate smaller pores. The intrusion volume is monitored through changes in mercury level. The pressure is increased in a specific series and at each pressure point the cumulative volume of mercury is measured. The pressure with which the mercury intrudes the sample provides the pore size, and the incremental volume introduced determines the number of pores with a certain size (La Scala *et al.*, 2000). Plotting the incremental intrusion volume against pore radius provides the relevant information regarding pore size distribution within the sample.

5.2.4 SAXS Data Correction and Analysis

The eggshells examined using the SAXS configuration on the NanoSTAR were analysed to obtain a size value of the smallest dimension of the scattering object, which is likely to be an indication of the pore/void size. The background was subtracted from the SAXS data collected from the eggshells laid by young and aged hens, and the scattering intensity of the two-dimensional patterns was integrated and converted into one-dimensional linear traces of I(q) against q. The integration of the scattering intensity was similar to that used for the Daresbury and ESRF data described in the previous results in Chapters 3 and 4. The size values were calculated using the same equation as described in subsection 2.10.2.

5.2.5 Statistical Analysis

The breaking strength data for young and aged hen groups were compared using a one-way analysis of variance (ANOVA). The relationship between breaking strength and the pore/void size values obtained by SAXS was investigated using simple linear regression analysis. All statistical analyses were carried out using Minitab release 12.1 (© Minitab Inc.1998).

5.3 Results

5.3.1 Comparison of Eggshell Breaking Strength Measurements carried out on the Eggs from Young and Aged Hens

The mean breaking strength from each group of eggshells (n = 50) and the standard deviation values are shown in Table 5.1. The breaking strengths between the two groups were found to be significantly different ($p = 0.008$, statistically significant if $p \leq 0.05$).

Age	n	Breaking Strength (N) mean	Standard Deviation	p-value
35 week old hens	50	28.5	11.0	0.008
72 week old hens	50	23.6	6.4	

Table 5.1 The breaking strength data from the eggshells laid by hens at 35 and 72 weeks of age. There was a significant difference in breaking strength between the two groups ($p = 0.008$).

5.3.2 Comparison of the Nanostructural Measurements carried out on the Eggs from Young and Aged Hens

A double logarithmic graph for one of the eggshells obtained from the younger group of hens is shown in Figure 5.1. In this figure, the pink scattering curve at high q values follows Porod's Law (blue line), where the scattering intensity declines in inverse proportion to the fourth power with respect to the scattering angle. This indicates that the data analysis using the equation determined by Fratzl *et al.* (1996) described in subsection 2.10.2 can be applied. The decay in scattering intensity was similar for all the eggshells in this group; therefore, the same data analysis was applied in each case.

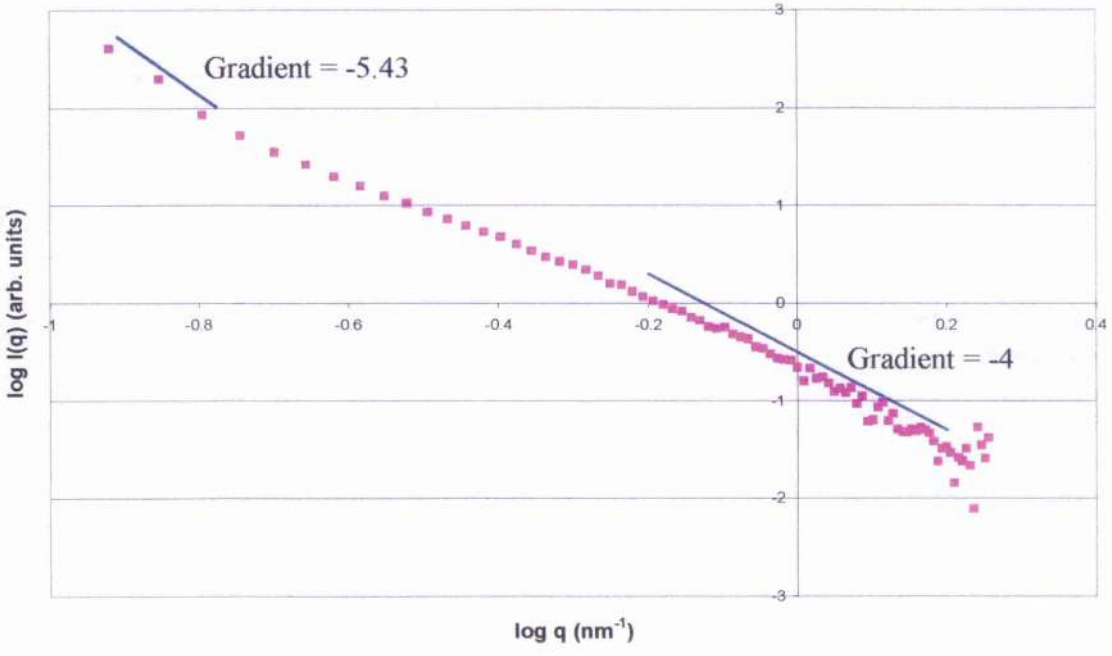

Figure 5.1 Double logarithmic scattering curve shown in pink obtained from an eggshell laid by a 35 week old hen. The blue line with a gradient of -4 depicts the Porod region, where the scattering intensity declines in inverse proportion to the fourth power.

In Figure 5.1, at the lowest observable q values, the scattering intensity decays approximately at q^{-5} (depicted by the blue line with a gradient of -5.43); this indicates that this portion of the scattering curve does not follow Porod's Law. Therefore, there are no scattering features in this region with sharp boundaries between the interfaces. It is possible that the scattering points in this region are from the tail end of scattering associated with the presence of larger vesicular holes as described in subsection 1.3.2. Vesicular holes however, are features of the eggshell ultrastructure and therefore occur at a completely different length scale.

The SAXS data from the eggshell samples laid by the aged hens were similar to the results obtained from the young hens. The scattering intensity was found to decay in inverse proportion to the fourth power at high q values and since this decay in the scattering intensity was observed for all the data within this group, the same analysis procedure to determine the size of the scattering features was applied. One of the scattering curves is shown in Figure 5.2 and is plotted on a double logarithmic graph (log I(q) against log q). The line in pink is the scattering from the eggshell sample, and the straight blue line with a gradient of approximately -4 indicates the Porod region.

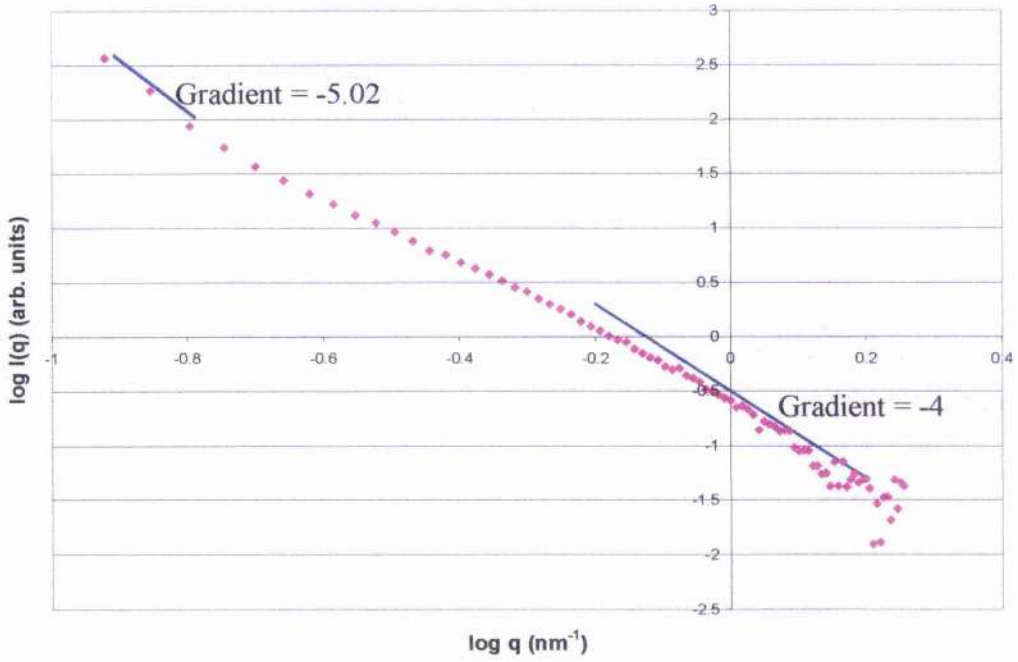

Figure 5.2 Double logarithmic scattering curve shown in pink obtained from an eggshell laid by a 72 week old hen. The blue line with a gradient of -4 depicts the Porod region, where the scattering intensity declines in inverse proportion to the fourth power.

According to this figure the scattering intensity decays approximately at q^{-5} at the lower q values (depicted by the blue line with a gradient of -5.02) similar to the results obtained from the young hens, indicating that the scattering features in this region are not from interfaces with sharp boundaries but from diffuse boundaries. This is similar to what has been suggested for other systems such as silica (Schmidt *et al.*, 1991). The scattering data was analysed and a size parameter calculated following the same procedure that was carried out for the eggshell samples laid by the young hens. The size values obtained in the eggs from young and aged hens are compared in Table 5.2.

Age	n	Pore/Void Size Value (nm) mean	Standard Deviation	*p*-value
35 week old hens	18	5.9	0.7	0.84
72 week old hens	18	5.8	0.6	

Table 5.2 The mean pore/void size value from the SAXS analysis from the 18 eggshells in each group, (hens at 35 weeks of age and hens at 72 weeks of age). There was no significant difference found between the size values obtained ($p = 0.84$).

The range in size values was between 4.7 – 7.2 nm for the eggs from young hens and 4.4 – 7.0 nm for the eggs from aged hens. The size values obtained are consistent with the size of the nanovoids measured in the results section of Chapter 3 (see subsection 3.3). Statistically there was no significant difference in the size of the nanovoids in each experimental group ($p = 0.84$).

5.3.3 The Relationship between the Size of the Nanovoids and Breaking Strength of Eggshells

In Figure 5.3 nanovoid size is plotted against eggshell breaking strength. The eggshell samples laid by the young hens are shown as blue diamonds and the eggshell samples laid by the aged hens are shown as red squares in this figure.

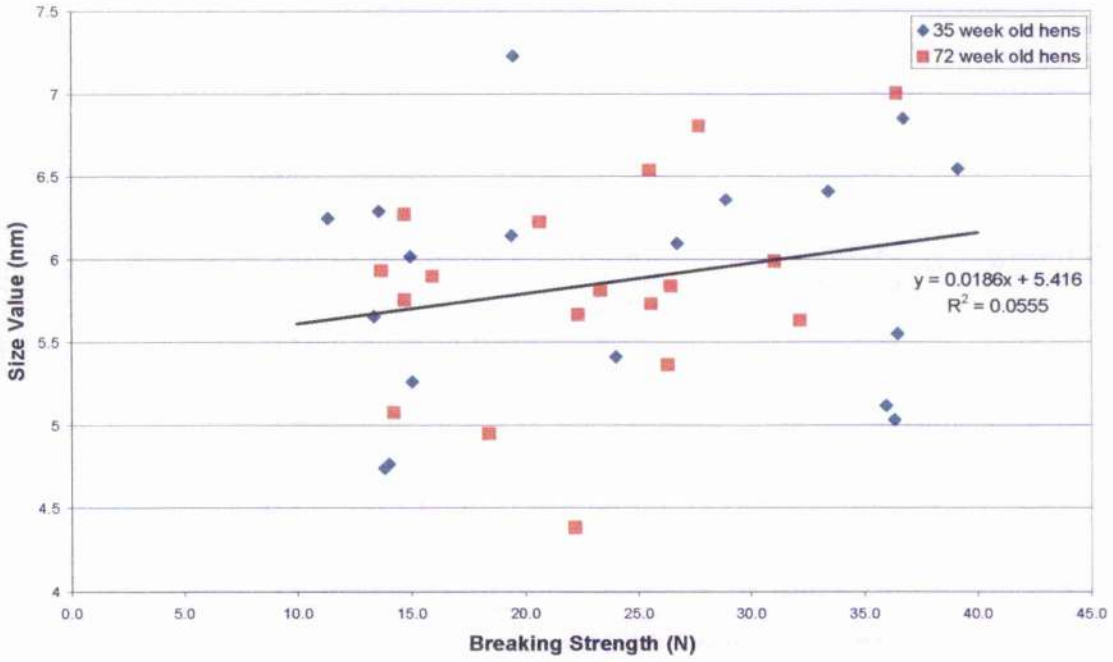

Figure 5.3 Nanovoid size values and eggshell breaking strength of eggs laid by young and aged hens ($R^2 = 0.0555$, $p = 0.168$).

According to Figure 5.3 there is no relationship between the size of the nanovoids and eggshell breaking strength ($R^2 = 0.0555$, $p = 0.168$).

5.3.4 Pore Size Investigated using Mercury Intrusion Porosimetry

The breaking strengths of the eggshells used in the mercury intrusion porosimetry experiments are summarised in Table 5.3.

Eggshell Sample	Breaking Strength Maximum Load (N)
1 (low mechanical strength)	28.09
2 (low mechanical strength)	30.62
3 (high mechanical strength)	45.99
4 (high mechanical strength)	48.12

Table 5.3 Breaking strength measurements of the eggshells analysed using mercury intrusion porosimetry.

The mercury intrusion porosimetry results show the pore size distribution in each eggshell sample, where the pore radius (nm) against incremental intrusion volume (ml/g) is plotted. Figures 5.4 and 5.5 display the results from the eggshells with the low mechanical strength, and Figures 5.6 and 5.7 are from the eggshells with the high mechanical strength. According to the figures presented here, all the samples have a dominant pore size distribution at 1000 – 2000 nm and another at 4000 - 5000 nm. Both of these pore size distributions however are well beyond the resolution of SAXS. The height of the peak at 4000 - 5000 nm is the same height in each of the eggshell groups indicating that both categories of eggshell have an equal distribution of pores in this range; however, the peak at 1000 – 2000 nm is larger in height in the eggshells with high breaking strengths. This indicates a greater mercury intrusion volume at this pore size; therefore, there are a larger number of these pores in the

eggshells with higher breaking strengths. There are a number of smaller peaks, which are within the SAXS range (<10 nm) (see Figures 5.4 and 5.5) indicating that smaller voids are present in these eggshells but there is not a dominant peak corresponding to a specific pore size. In contrast, the high mechanical strength eggshells (Figures 5.6 and 5.7) display a more prominent peak corresponding to pore sizes with a radius of approximately 2.9 nm, which is the equivalent to a diameter of approximately 5.8 nm. These pores are of a similar size range to the nanovoids previously defined in this thesis using SAXS.

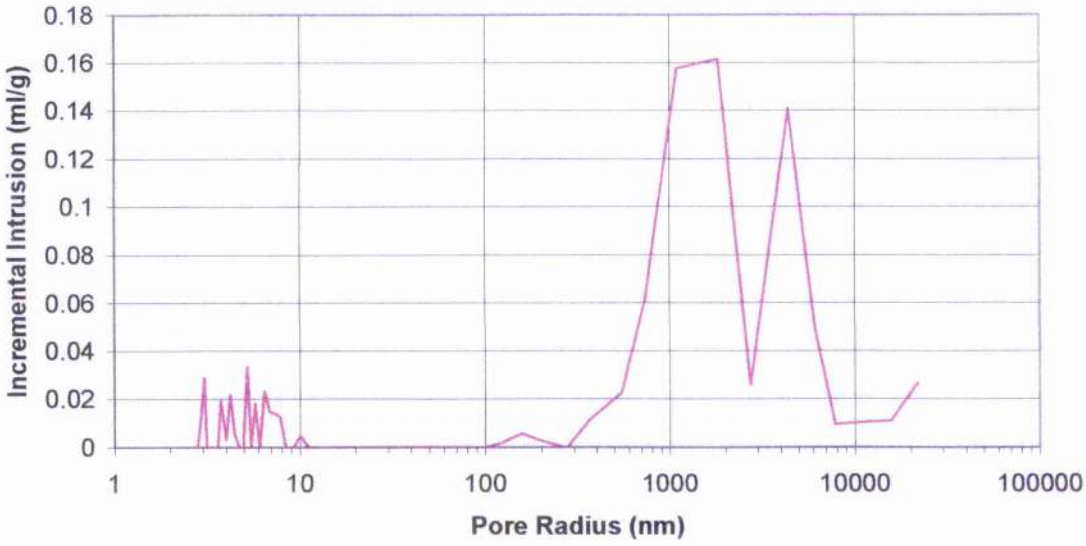

Figure 5.4 Pore size distribution from eggshell 1, which had a low breaking strength.

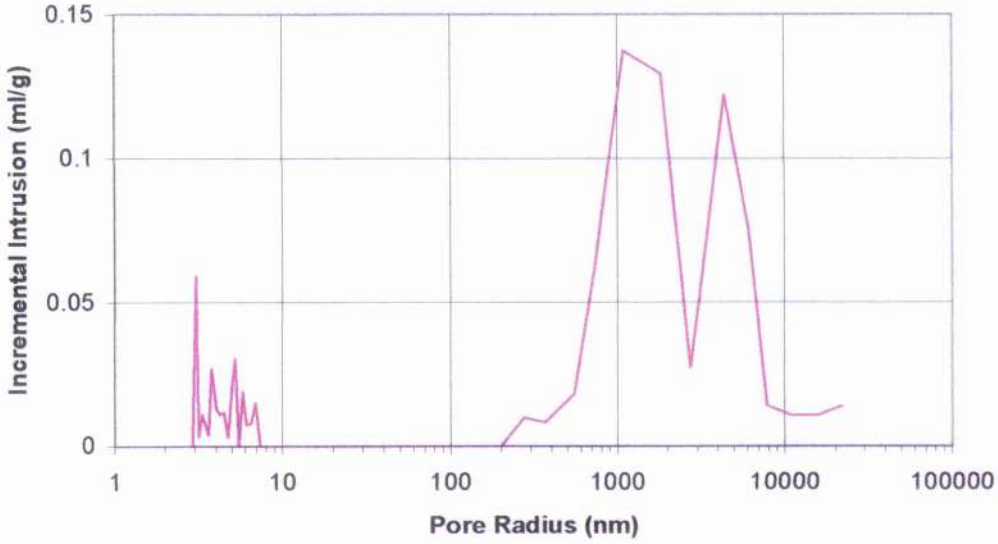

Figure 5.5 Pore size distribution from eggshell 2, which had a low breaking strength.

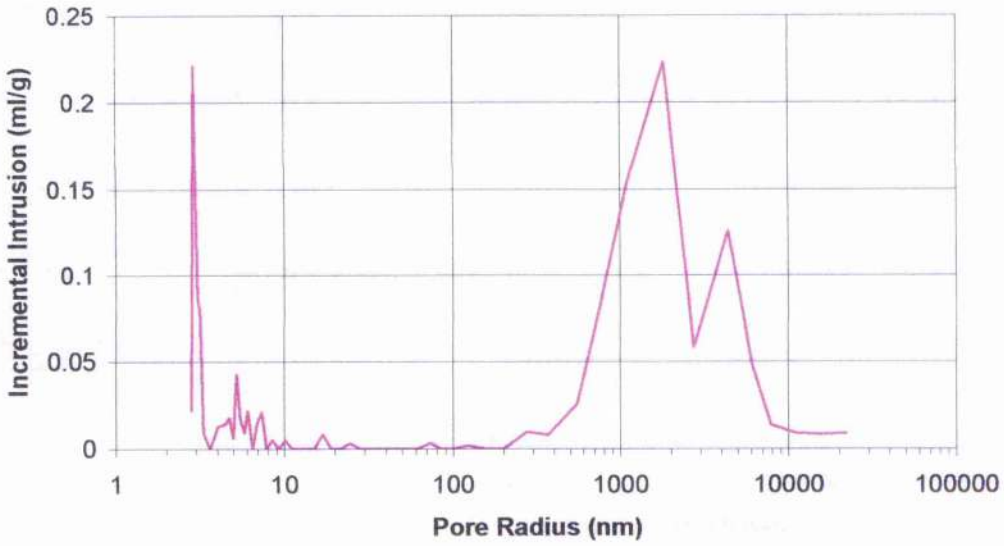

Figure 5.6 Pore size distribution from eggshell 3, which had a high breaking strength.

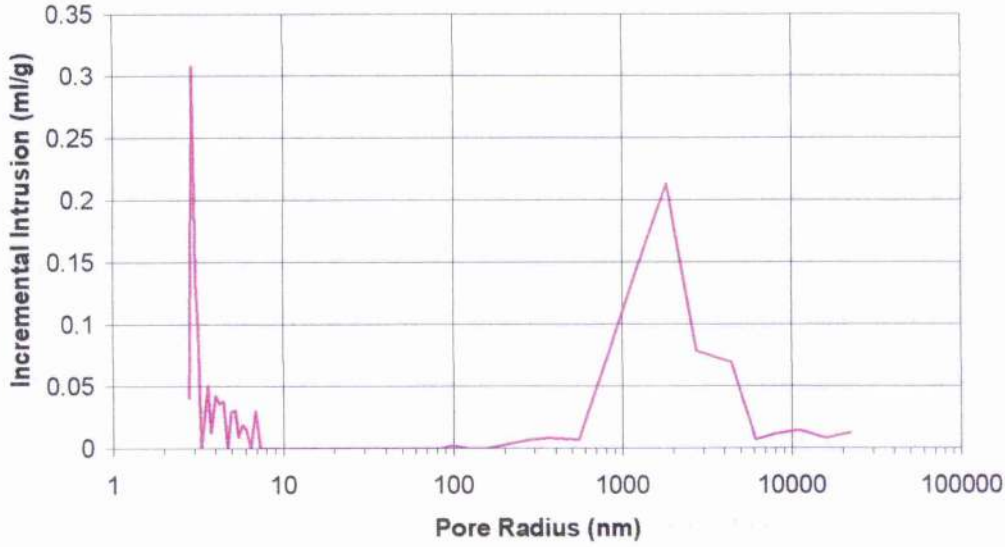

Figure 5.7 Pore size distribution from eggshell 4, which had a high breaking strength.

The incremental mercury intrusion for the pore radii less than 10 nm are compared in Figure 5.8.

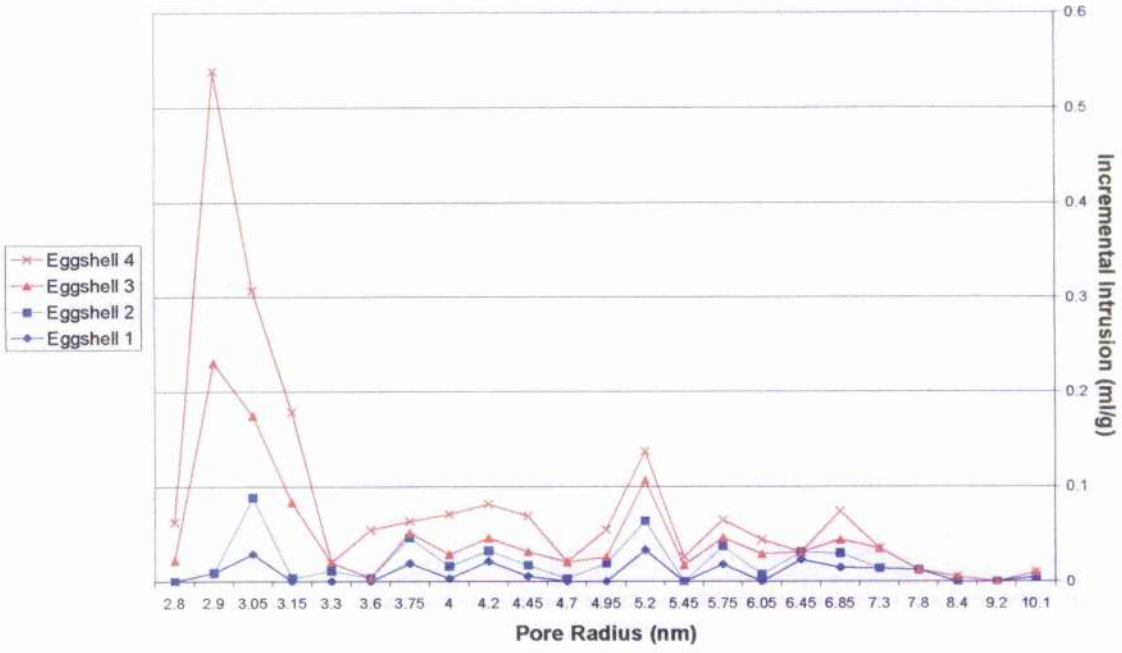

Figure 5.8 Comparison of the pore radius measurements below 10 nm in eggs exhibiting high or low breaking strengths. The high mechanical strength eggshells (shown in red) have a dominant peak at approximately 2.9 nm, unlike the low mechanical strength eggshells (shown in blue).

This plot confirms that the high mechanical strength eggshells (lines are shown in red) have a more dominant pore size population at around 2.9 nm than the low strength eggshells (lines are shown in blue). The spread of pore radii up to 10 nm is similar for both high and low mechanical strength eggshells.

5.4 Discussion

Eggshells from young and aged hens exhibiting different breaking strengths were investigated in this chapter by SAXS using the NanoSTAR instrumentation. The eggshell samples were powdered so the SAXS size values obtained represent the average size values for each specimen. The average size value for the eggshells laid by the young hens was 5.9 nm, and the average size value from the eggshells of the aged hens was 5.8 nm. This indicates that the measurements made regarding information about the scattering features in the powdered eggshell samples from each experimental group are similar.

Within the eggshell, approximately 95 % of the mineral fraction is composed of calcium carbonate crystals in their calcitic form; these crystals are known to be on the micron length scale, which is beyond the range of SAXS. However, in Chapter 3 it was hypothesised that intracrystalline particles or voids occur at the nanometer length scale within these crystals due to the presence of embedded matrix proteins. In this chapter, SAXS revealed that the smallest dimension of the intracrystalline particles in both the eggshells from both young and aged hens was in the range of 5 - 6 nm. These values bear an excellent resemblance to the data obtained from the SAXS data described in Chapter 3 and therefore adds support to this hypothesis.

According to Panheleux *et al.* (2000), the total protein content within the eggshells produced by young and aged hens does not change; however, the concentration of individual proteins was reported to change over time. In the context of the current work, it is possible that in measuring the average size values from bulk powdered eggshell samples that information relating to more subtle changes in the nanoporosity arising from the contributions made by individual matrix proteins has been lost.

An interesting deviance in the slope at lower q values of the scattering curve was observed in the eggshells analysed by the NanoSTAR in this chapter; at higher q values, the intensity decays with a rate proportional to approximately q^{-4}, which has been defined by Porod's Law to be scattering from a two-phase system with sharp boundaries. At lower q values however, the scattering intensity decays with a rate proportional to q^{-5}, which has been observed before in SAXS data from silica by Schmidt *et al.* (1991). Similar observations were made by Lorenz-Haas *et al.* (2003) who investigated the defects at polymer-polymer interfaces. Schmidt *et al.* (1991) reported that a slope being greater than -4 was a result of a "fuzzy" boundary, where the surroundings of the pore boundary does not decline instantly to zero density in the pore, but rather decays continuously from the constant density of the surrounding silica. SAXS does not resolve the structure at the atomic scale; therefore, the density can be regarded as being constant. Lorenz-Haas *et al.* (2003) also observed that steep slopes in the scattering curves are related to a diffuse transition in electron density between two interfaces, the air and the polymer; therefore, structural features with sharp boundaries are not seen. With respect to the slope of -4 as described in Porod's Law, the density change is instant from the inside of the pore, where density is zero, to the surrounding media, which has a constant density. Therefore, the results presented in this chapter seem to indicate that there are diffuse boundaries within the eggshell material at the observed length scale seen at lower q values. There is another possibility that this feature is the tail end of scattering from a group of larger structural features such as the vesicular holes highlighted in section 1.3.2. A longer camera length may have permitted more information to be obtained at this lower q value region.

The apparent lack of a relationship between the eggshell breaking strength and pore/void size (Figure 5.3) suggests that the nanoporosity of the eggshell does not significantly contribute

to the mechanical properties of the shell. This contrasts with the findings of Rodriguez-Navarro *et al.* (2002) and Ahmed *et al.* (2005) who both found a significant relationship between the crystallographic properties of the shell and eggshell breaking strength. The lack of a relationship here could simply relate to the bulk measurements of nanoporosity carried out in these experiments. Future work would concentrate more on characterising the range in nanoporosity through the shell thickness by collecting SAXS data at specific points in the layers of the eggshell instead of bulk averaging.

The quasi-static compression test does not provide a global measurement of the mechanical properties of the eggshell i.e. only two points on the egg are tested; therefore, the test can be heavily influenced by the presence of localised defects in its microstructure (Bain, 1992). It is therefore possible that the method of assessing eggshell strength was flawed in this investigation. A complementary study in which the dynamic stiffness measurement was used instead of the eggshell breaking strength however also failed to reveal any relationship between the pore/void size and mechanical properties of the eggshell (data not presented vs Bain, pers comm). This adds more credence to the argument presented above for the lack of any correlation.

The mercury intrusion porosimetry experiments revealed two sets of pore size distributions outwith the range of SAXS in both the low and high strength eggshells. One pore size distribution was observed to have a diameter of between 2000 – 4000 nm which approximates to the sizes of the vesicular holes observed by previous researchers using electron microscopy techniques (Simons, 1971). La Scala, *et al.* (2000) used mercury intrusion porosimetry but found pore diameters between 0.2 to 5 μm (200 – 5000 nm), which would correspond to the vesicular pores. Although this was only a preliminary investigation,

the eggs exhibiting higher breaking strengths appeared to have a greater volume of these pores or vesicular holes. This is not supported by Fraser *et al.* (1998) who found that eggshells laid by hens at the end of lay (which coincides with a decrease in eggshell quality) showed an increase in the number of vesicles in the palisade layer of the eggshell. The larger pore size distribution observed in these experiments corresponded to a pore diameter of between 9 - 10 μm. The eggs with high breaking strength apparently had fewer of these larger pores, which approximate to the size of large vesicular holes or gaseous exchange pores.

A third pore size distribution was also observed in the eggs with high breaking strength at less than 10 nm with a peak at 2.9 nm (pore radius), which are sizes within the SAXS range. A similar pore size distribution was also observed in the low mechanical strength eggs but the peak at 2.9 nm was not dominant in this group. The diameter of these pores (5.8 nm) is comparable to the values obtained using SAXS, and so these pores are likely to correspond to nanovoids in the eggshell samples. The SAXS analysis on eggs from young and aged hens indicated that both types of eggshells contain nanovoids, but did not provide any information as to the volume of these nanovoids or if they differed in eggs exhibiting contrasting mechanical properties. The results of the mercury porosimetry study suggest that there is a greater volume of these nanovoids in the eggshells exhibiting superior eggshell strength characteristics. It is tempting to speculate that this effect could arise from a change in the protein composition of the organic matrix but this needs to be investigated and is beyond the scope of this thesis. The results presented here nevertheless support the suggestion that mechanical strength of eggshells is related to its porosimetry at all length scales.

In conclusion, the results from the SAXS experiments (young and aged hens eggshells) show that the average size of nanovoids does not change in eggshells which display significant differences in their strength characteristics. Similar size values were determined for each experimental group of eggs suggesting that the measurements obtained by the NanoSTAR were from the same scattering features within the samples. The pore sizes observed by mercury intrusion porosimetry were comparable to the SAXS size values presented throughout this thesis. This adds further support to the hypothesis that proteins embedded within the calcium carbonate crystals and distributed throughout the different layers cause nanovoids in the eggshell structure, and that these are distinct from pores at other length scales. The electron density contrast between the voids and the surrounding inorganic material leads to the scattering signal observed, and analysis of this data reveals size values of the scattering objects to be of the order of 3 – 7 nm, which would correspond to the size of embedded proteins.

In Chapter 6 the complex interactions between proteins and calcium carbonate at the nanometer length scale are investigated further using *in vitro* crystallisation techniques.

Chapter 6

Application of SAXS to Investigate the Modifying Effects of Macromolecules on the Initial Nucleation and Growth of Calcium Carbonate *In Vitro*

6.1 Introduction

The strength and unique functional properties of the hen's eggshell and the rapid rate at which it is formed are a paradigm for those interested in biomineralisation. Understanding the mechanisms and the controlling factors involved in its formation are not only of interest from a biological point of view, but could also be applied to the development of novel systems through biomimetic processes (Heuer *et al.*, 1992; Arias and Fernandez, 2003). This however requires a more complete understanding of the structure of the hen's eggshell at different length scales and how the mineral and inorganic moieties relate and interact with one another.

Several authors have used *in vitro* crystallisation techniques to investigate if eggshell matrix proteins influence the rate of calcium carbonate precipitation and crystal morphology (Gautron *et al.*, 1996; 1997; Dominguez-Vera *et al.*, 2000; Fernandez *et al.*, 2004). In these types of experiments, either the duration of precipitation or morphology of calcium carbonate resulting from a metastable solution of sodium bicarbonate and calcium chloride in water is usually compared with that where eggshell extract or uterine fluid has been added to the system. Under these conditions, the induction time for calcium carbonate precipitation has been shown to be reduced and even inhibited by the presence of uterine fluid, and the morphology of the calcite crystals has also been shown to be markedly altered (Gautron *et al.*, 1997). To date, however, there is no information at the nanometer length scale

describing how these macromolecules might influence the initial nucleation and growth events of calcium carbonate either *in vitro* or *in vivo*.

Calcium carbonate is widely used in industry as a filler in paper, plastics and rubber, and also in paint, sealants, cosmetic and pharmaceutical products (Heeley *et al.*, 2002). Calcium carbonate is also found in parchment, where it forms as a result of the parchment making process (Kennedy and Wess, 2003). Because of its wide industrial application, calcium carbonate formation *in vitro* has received much attention as nucleation events are critical to controlling overall crystal morphology and in the selection of the major mineral phase deposited from the reagent solutions. Recently, time-resolved SAXS at a third generation synchrotron source has been used to study the initial nucleation and subsequent phases of calcium carbonate *in vitro*. Using a large volume crystalliser in conjunction with SAXS, Heeley *et al.* (2002) reported that calcium carbonate formation is in fact a two-step process which initially involves the production of an amorphous phase. Using a stopped flow system, Bolze *et al.* (2002) and Pontoni *et al.* (2003) confirmed this result and proposed that SAXS can be used to provide useful information about the size, shape, mass, density and number of the initial particles and aggregations, which form as a function of the reaction time.

In the light of these exciting developments, the experimental design described by Bolze *et al.* (2002) and Pontoni *et al.* (2003) is applied in conjunction with SAXS in this chapter to investigate the effect of a range of eggshell proteins on the initial nucleation of calcium carbonate *in vitro* at the nanometer length scale. From these experiments, it was hoped to gain some insight into how eggshell matrix proteins might interact with calcium carbonate

during the initial stages of shell formation *in situ*, and how this in turn gives rise to the development of the nanostructural features described in Chapters 3, 4 and 5 of this thesis.

6.2 Materials and Methods

6.2.1 Experimental Set-up

The experiments described in this chapter were all carried out at the SRS Daresbury Laboratory on station MPW6.2 (described in subsection 2.9.3), which was connected to a BioLogic stopped flow cell SFM-300 (stopped flow module), which permits fast and effective mixing of reagents (see Figure 6.1).

6.2.2 In Vitro Crystallisation of Calcium Carbonate

The initial experiments were carried out following the technique described previously (Bolze *et al.*, 2002; Pontoni *et al.*, 2003) using equal volumes (total of 300 – 500 µl) of calcium chloride and sodium carbonate solutions. The concentration of these solutions ranged from between 7.5 – 10.5 mM. At the start of each experiment, 10 ml of each reagent was loaded into each of two syringe reservoirs, labelled 1 and 3 in Figure 6.1. These solutions were then simultaneously injected into mixer 2 of the stopped flow cell and then into the cuvette. An additional syringe (labelled 2 in Figure 6.1) was loaded with 10 ml deionised water. This was used to flush out the system after each experiment to ensure that the mixing lines and capillary were clean before proceeding with the next experiment. At the end of each experiment, dilute hydrochloric acid was also flushed through the system to remove any calcium carbonate precipitate.

6.2.3 Introducing Macromolecules into the Experimental Model

Modified versions of the 9 mM calcium chloride solution were also prepared and used in subsequent crystallisation experiments. These were prepared by adding either 2 mg of ovalbumin or 100 µl - 250 µl of oviducal fluid to the 10 ml reservoir syringe containing the 9 mM calcium chloride just prior to injection. Each modified calcium chloride solution was then mixed with a 9 mM solution of sodium carbonate to investigate whether the presence of macromolecules influenced the formation of calcium carbonate. The oviducal fluid used in these experiments was provided by the Roslin Institute, Edinburgh, UK.

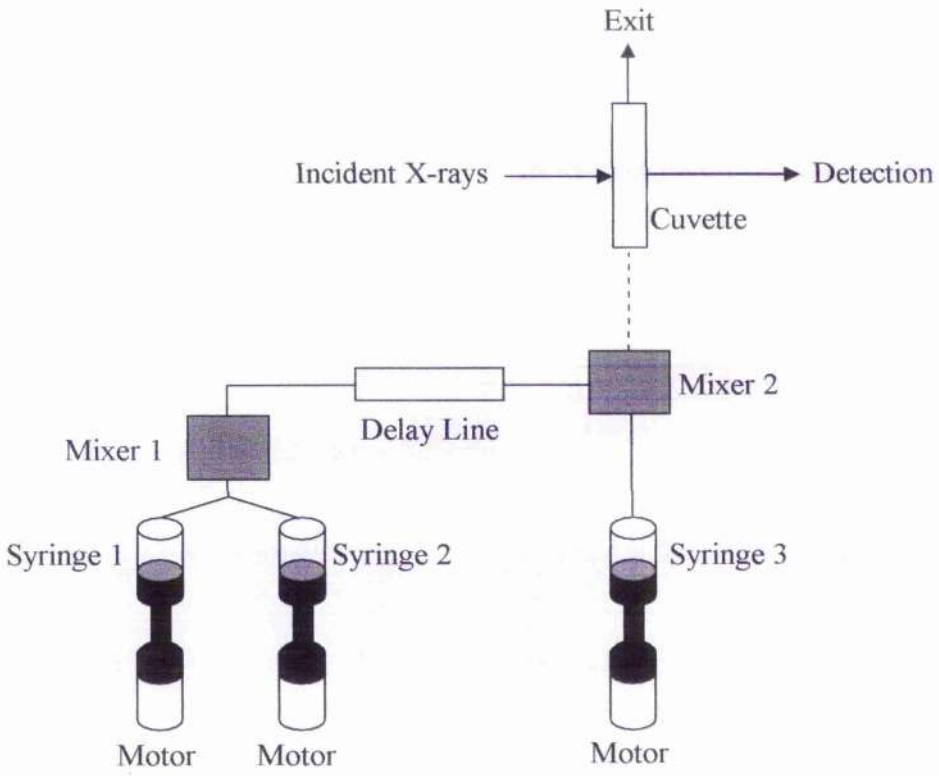

Figure 6.1 Schematic of the Biologic stopped flow cell layout, showing where the delay lines and mixers are located.

6.2.4 Data Acquisition

The SAXS data was collected on a one-dimensional detector (see subsection 2.9.3 for details). The camera length for the SAXS configuration was 3.3 m and the incident photon energy was 12.4 keV (1.0 Å). The scattering limits range from $q = 0.152$ nm^{-1} to 3.72 nm^{-1}. Buffer background measurements for deionised water were taken for each experiment and subtracted from the acquired data. The data acquisition time for each experiment was set to between 50 ms and 1 s, which were used in an attempt to ensure that data was being collected whilst the first calcium carbonate clusters were nucleating.

6.3 Results

A double logarithmic plot of the scattering intensity obtained from mixing 7.5 mM solutions of calcium chloride and sodium carbonate in the stopped flow system is shown as the blue curve in Figure 6.2. The corresponding double logarithmic plots of the scattering intensity obtained when 9 mM solutions of calcium chloride and sodium carbonate were mixed using the same system is shown as the blue curve in Figure 6.3. This figure also shows the effect on the scattering intensity when either 250 µl of oviducal fluid or 2 mg of ovalbumin were added to the 9 mM calcium chloride solution prior to injection (pink and yellow plots respectively).

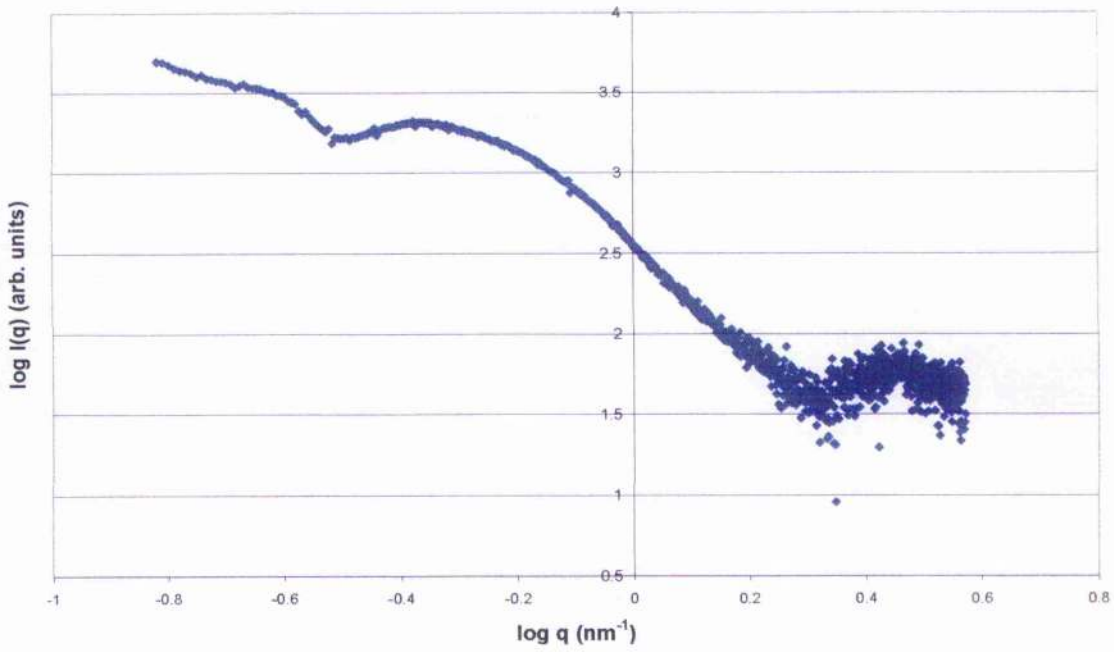

Figure 6.2 A double logarithmic plot of calcium carbonate crystallised from equal concentrations (7.5 mM) of calcium chloride and sodium carbonate solutions. The data acquisition was 100 ms / frame and the average of the first 100 frames is shown. The oscillations suggest that crystals are forming.

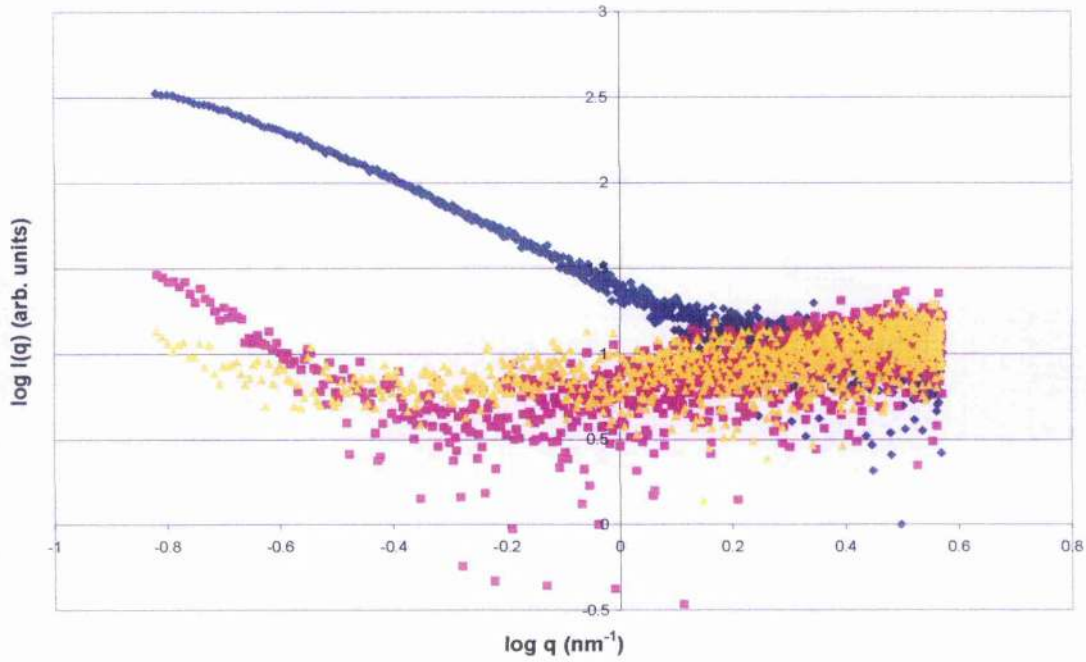

Figure 6.3 A double logarithmic plot of calcium carbonate crystallisation resulting from the combination of equal concentrations (9 mM) of calcium chloride and sodium carbonate (blue) in a stopped flow system, (data acquisition was 100 ms per frame). Similar plots for crystallisation, in the presence of 250 μl oviducal fluid (pink), (data acquisition was 180 ms per frame), and 2 mg ovalbumin (yellow), (data acquisition was 180 ms per frame) are also represented. The average of the first 100 frames of each is shown. All the data have had transmission corrected water backgrounds subtracted.

The only scattering data collected that seemed to indicate that crystals may have formed is shown in Figure 6.2, where oscillations were observed in the scattering profiles. These bear some similarity to those observed by Bolze *et al.* (2002) who suggested that these oscillations result from the formation of spherical particles of calcium carbonate within the system. According to this author, the scattering intensity can be used to provide information about the sizes of the calcium carbonate crystals that are being formed. The radius of gyration was therefore determined through the use of GNOM (Svergun *et al.*, 1988) and was found to be 10.39 ± 0.01 nm.

The scattering curve obtained when 9mM solutions of each reagent were mixed in the stopped flow system do not show this oscillatory behaviour (Figure 6.3). This effect is unlikely to be due to the change in concentration of the reagents as Bolze *et al.* (2002) used similar concentrations. The results presented by Bolze *et al.* (2002) and Pontoni *et al.* (2003) however do not seem to be reproducible in spite of our best efforts. The scattering curves obtained when either oviducal fluid or ovalbumin was added to the 9 mM calcium chloride solution, prior to injection, were much weaker and of lower intensity than that obtained using the standard 9 mM calcium chloride solution, the scattering intensity however still increased at higher q (Figure 6.3).

6.4 Discussion

These preliminary investigations were carried out to determine if SAXS is a useful tool to investigate the role played by matrix proteins in the nucleation and growth of calcium carbonate *in vitro*. This type of investigation has previously been shown to provide information about the initial nucleation and growth process, and the conditions and factors that influence formation, crystal morphology and size. The type of knowledge generated in this type of study and the principles behind the formation of biominerals like the eggshell could be used in attempts to bioengineer new systems.

The lack of consistency in the SAXS data obtained in the current investigations when different concentrations of calcium chloride and sodium carbonate were used may have occurred if the nucleation of calcium carbonate crystals had began either before or after the timings used for data collection. If nucleation was initiated before the data collection had commenced then it is likely that the calcium carbonate crystals would have been too large to be detected by the camera length used in these experiments. The fact that there is some degree of scattering present in the curves generated by both the 7.5 mM and 9 mM stock solutions to some extent support this hypothesis, but a longer length camera would have to have been employed in an attempt to confirm this.

Despite the lack of consistency in the data it is interesting to note that when oviducal fluid or ovalbumin were added to the stock 9 mM solution of calcium chloride, the scattering curve changed considerably. Indeed, by the time the background scattering had been subtracted from this data the scattering intensity became almost zero. The addition of oviducal fluid has previously been shown by Gautron *et al.* (1997) to delay the onset of crystallisation of

calcium carbonate *in vitro*. Hernández-Hernández *et al.* (2003) subsequently observed that high concentrations of four globular proteins (lysozyme, α-lactalbumin, ribonuclease and myoglobin) exhibited a similar inhibitory effect. The lack of scattering observed when macromolecules were introduced in the current work is therefore consistent with a delay in the onset of nucleation. The experiments by Bolze *et al.* (2002) and Pontoni *et al.* (2003) both showed oscillations in the scattering curves when various solutions of calcium chloride and sodium carbonate were mixed in a stopped flow cell. In the studies presented here, oscillations were only observed when 7.5 mM solutions were used.

The radius of gyration provides information about the size of the crystals formed in these investigations; in the current work the size of the scattering objects giving rise to the oscillations was determined to be 10.39 ± 0.01 nm. These size values are much lower than the sizes quoted by Heeley *et al.* (2002), who obtained a size of approximately 35 nm, and Bolze *et al.* (2002), who obtained average radius sizes of 32 nm, 75 nm, and 133 nm at the initial, middle, and final stages of crystallisation, respectively. Heeley *et al.* (2002) inferred that there was a metastable phase, which was amorphous, during the formation of calcium carbonate *in vitro*, which then transforms into the crystalline phase. This was also observed by Bolze *et al.* (2002) and Pontoni *et al.* (2003). It is therefore possible that the smaller calcium carbonate crystal sizes represented in the current work correspond to the beginning of spherulitic formation. Further work however is needed to confirm this hypothesis.

To allow these events to be studied in more detail, greater attention needs to be paid to the triggering of the stopped flow system and the timing of the data acquisition. Due to the advanced technology now available, such as the high brilliance X-ray beam at synchrotron

sources and data acquisition in the millisecond regime (Narayanan *et al.*, 2001; Cernik *et al.*, 2004) it is now possible to carryout fast kinetic experiments. The knowledge gained from studies like this will significantly improve our understanding of the processes, which give rise to the formation of the eggshell *in situ*. The same principles may also be used in attempts to bioengineer new systems in the future.

In conclusion, the preliminary results described in this chapter have provided a clearer picture of the speed at which nucleation of calcium carbonate occurs *in vitro* and have shown that macromolecules are capable of inhibiting nucleation. These experiments have also provided further insight as to the size of the resulting crystals, which form at different phases of this crystallisation process. SAXS is therefore a useful tool which should be exploited further in the future to investigate the role played by eggshell matrix proteins in the nucleation and growth of the hen's eggshell.

Chapter 7

General Discussion and Conclusions

The main aim of this thesis was to investigate structural features of eggshell at the nanometer length scale. The major contributions to our understanding gained by the work presented in this thesis are explained here.

7.1 Two-Dimensional Mapping of Normal and Abnormal Eggshells

Microfocus SAXS was used to investigate nanostructural variations within the different layers of the eggshell by sequentially scanning over the entire thickness of thin intact transverse sections. Two-dimensional mapping showed that there were nanostructural changes throughout the eggshell thickness, with the most substantial variations occurring in the mammillary layer. Within the two-dimensional maps produced for the normal eggshell, a banding of nanoporosity size and scattering intensity was observed in the separate layers; however, this banding effect was absent in the abnormal eggshells. Thus, it can be concluded that for normal eggshells, the nanostructure varies between the different layers of the eggshell in such a way as to create an intricate design, which presumably optimises the functional properties of the eggshell namely, protection and support of the egg contents. Likewise, it can be concluded that if this nanostructural pattern is severely disrupted during shell formation then the gross appearance of the eggshell and hence its functional properties will be severely disrupted. The eggshells analysed in Chapter 3 were extremes in terms of quality, but it is highly likely that even subtle changes in the nanostructural organisation of the eggshell will influence its functional properties and hence overall quality.

The most likely interpretation of the results obtained from the scanning microfocus SAXS in Chapter 3 is that the scattering signal observed in the normal eggshell resulted from the presence of nanopores or voids within the crystallites. The size dimensions of these voids/pores were subsequently found to be between approximately 3 – 5 nm. These nanovoids probably arise as a result of proteins becoming embedded within the calcified framework as the shell is forming. It is interesting to note that the size of these protein voids was comparable in both the normal and grossly abnormal eggshells used in these analyses.

A more detailed analysis of the mammillary layer from normal eggshells using the same technique showed enhanced intensity of scattering specifically in the mammillary cores compared to the surrounding material. The most convincing explanation for this observation is that the scattering was caused by a highly localised concentration of protein within the cores since this may produce a nanoporous structure. These proteins possibly play a key role in the initial nucleation of calcium carbonate during the initial stages of shell formation. No detailed scan of the mammillary layer from an abnormal eggshell was conducted; therefore, no comparison can be made between the normal and abnormal eggshells. However, it is tempting to speculate that variations in the scattering signal might have been observed in the abnormal eggshell signifying a disruption in the initial nucleation of this type of eggshell.

7.2 Nanostructural Examination of Powdered Eggshells at Different Stages of Gestation using X-ray Diffraction and Small Angle X-ray Scattering

The structure of eggshells expelled at different stages of gestation were investigated as they represent different stages in the shell growth process and are therefore ideal for monitoring the temporal and spatial changes in crystallite size and nanoporosity as the eggshell forms. In this study, powdered samples were compared using the NanoSTAR instrumentation. Two

techniques were compared, namely XRD and SAXS, in order to identify which gave the most useful and accurate information relating to the eggshell nanostructure. The results indicated that the calcium carbonate crystallites were too large to be accurately measured using the powder X-ray line broadening from the XRD data and the Rietveld method, whereas the SAXS analysis was shown to be the most appropriate technique for investigating the nanoscale structures with electron density contrast within these larger crystallites. From the SAXS data, the average sizes of the scattering objects obtained from the powdered eggshell material was between, 5.7 – 7.2 nm. The size of the scattering objects was also consistent within samples from different stages of gestation. This was a rather unexpected result but can perhaps now be explained in terms of the fact that although the protein component of the eggshell matrix changes in relation to the phase of shell formation, the size of the voids or pores present within the eggshell due to the presence of these embedded proteins is fairly constant. The size values obtained using powdered eggshell material and the NanoSTAR instrumentation were also consistent with those measured in Chapter 3, thus confirming that in each case the same nanostructural features of the eggshell were being measured.

7.3 An Examination of the Nanostructure of Eggshells Exhibiting Different Mechanical Strengths

The eggshells laid by young and aged hens exhibited an average nanovoid size value of 5.9 ± 0.7 nm and 5.8 ± 0.6 nm respectively, as determined by the SAXS data. In other words, the nanostructural features of both types of eggshell were comparable despite there being significant differences in their mechanical properties. The size values were again similar to the previous results from Chapters 3 and 4, which supports the hypothesis that the size measurements in all cases were from the same voids/pores within the calcium carbonate

crystals. The mercury intrusion porosimetry results revealed pore sizes that were less than 10 nm, which were comparable with the SAXS results. This complementary data provides additional evidence that in all cases the features being measured correspond to the voids formed by embedded proteins within the calcium carbonate crystals. However, in the case of mercury intrusion porosimetry, for the mercury to gain entry into these nanopores they must be inter-connected in some way, for example by channels. Thus, it can be concluded that the embedded proteins in eggshells are not enclosed but have some degree of connectivity between them or a subset of connected nanovoids exists.

7.4 Application of SAXS to Investigate the Modifying Effects of Macromolecules on the Initial Nucleation and Growth of Calcium Carbonate *In Vitro*

The influence of eggshell proteins on the formation of the eggshell is likely to occur at the nanometer length scale. The *in vitro* crystallisation experiments carried out in this thesis were specifically designed to investigate this nucleation event and the subsequent growth of calcium carbonate both with and without the presence of organic matrix proteins. The results presented are only preliminary but they do provide some insight into the speed or rate at which this initial nucleation process takes place, and on the size of the resultant calcium carbonate crystals. For example, it was suggested that the calcium carbonate crystals form very rapidly; future experiments may therefore require the concentration of the active reagents to be substantially reduced if this nucleation event is to be captured. In addition, oscillations were observed in the scattering curve when the reactant solution concentrations were 7.5 mM; these oscillations possibly corresponded to spherulitic formation since the size values obtained were much smaller than those found by other researchers.

7.5 Overall Conclusion and Potential Future Work

The results from the experiments presented in this thesis indicate that nanostructure of the eggshell is characterised by the presence of nanovoids or nanopores within the crystals of calcium carbonate, which form as a result of eggshell matrix proteins becoming embedded during the process of shell formation (Figure 1.10 shows how crystals, crystallites and nanovoids relate to one another). Differences in the nanostructural organisation of eggshells can be identified between normal and abnormal eggshells; the normal eggshell is highly organised structurally and is formed in such a way as to maximise its functional properties. The temporal and spatial distribution of eggshell matrix proteins in eggshells likely exerts some influence on the formation of nanovoids or pores during the shell forming process but apparently exerts little effect on the size of these nanostructural features. The X-ray source and where the experiments were carried out did not seem to influence the size values obtained for these nanostructural features. Both powdered and thin sections of intact eggshell gave similar size values.

Although the NanoSTAR instrumentation makes use of powdered eggshell material it is unlikely that SAXS could never be adapted as a tool for the routine assessment of eggshell quality. This requires a high throughput technique so that large quantities of eggshell samples can be processed at any one time. SAXS, however, can be used to obtain hundreds of SAXS patterns from one individual sample, thus providing detailed information about the nanostructural features of any one specific area of interest; this capability has proven to be fundamental to our understanding of the eggshell nanostructure.

Microfocus SAXS has been shown to provide essential detail regarding the nanostructural changes within the eggshell and more specifically it has been highly useful in highlighting

regions of high protein content, such as the cores of the mammillary layer, where the scattering signal was greater than the surrounding area. If time had permitted, it would have been interesting to conduct similar detailed scans of the mammillary layer of abnormal eggshells. This would perhaps have allowed some comment to be made on whether a disruption to the nanostructural organisation of the initial formation of the mammillary bodies was responsible for or had a knock-on effect on subsequent shell growth mechanisms.

Regarding size measurements of the scattering objects, similar values were obtained from different eggshell samples independent of whether the samples were intact or powdered. The likely explanation for the sizes is that this pore size distribution is from proteins that are known to be embedded within the inorganic material thus resulting in nanoporosity within the eggshell as observed in the SAXS data. This hypothesis is also supported by the data obtained from mercury intrusion porosimetry experiments where pore size distribution coincided with the size measurements from the SAXS analysis. Future work should consider the use of mercury intrusion porosimetry to examine a larger sample set to determine if this could be a useful technique to investigate variations in nanoporosity in eggshells exhibiting different quality characteristics.

In terms of SAXS, future improvements in the read-out times of detectors will significantly reduce the data acquisition time and therefore potentially more samples could be examined at synchrotron beamtime. A more detailed analysis of the nanostructure within individual layers of the eggshell such as the vertical crystal layer and its interface with the cuticle might even be possible using nanobeam SAXS technology, providing a more detailed map of structural changes that are better matched to the size of the morphological variation in the eggshell. The relationship of inter- and intra- crystalline proteins may also be addressed in

the future by attempting to contrast match the calcite crystal interfaces and voids between calcite crystals with a solution of similar electron density. If the intracrystalline proteins that are believed to be embedded in the crystals are not accessible to the contrast matching solution, then this would confirm that the scattering signal results from protein voids within the crystal matrix as suggested in this thesis. Likewise, the way forward to understanding nanonucleation of calcium carbonate crystals and the influence of eggshell proteins on nucleation and growth would be to repeat the in *vitro* crystallisation experiments using a larger range of concentrations of reactant solutions. Another possibility would be to test another stopped flow system such as the one used by Heeley *et al.*, (2002) and to use an alternative beamline, as the SAXS configuration used in the experiments reported here might not have been optimised for nucleation experiments. Once the beamline and configuration have been optimised, and the experiments produce meaningful data proving that nucleation and calcium carbonate crystals are forming, it would then be interesting to repeat them using a full range of eggshell matrix proteins. However, this would require the proteins to be first extracted and purified from eggshells, which at the present time remains both technically difficult and time consuming.

In conclusion, two-dimensional mapping of eggshells by microfocus SAXS has provided a unique insight into the nanostructural features of this complex biomineral especially within the mammillary layer. Similarly, SAXS analysis of powdered bulk samples of eggshells provided valuable nanostructural information despite it not being possible to detect any differences in the nanostructural features of eggs exhibiting different mechanical strengths. SAXS is therefore likely to continue to provide important structural information about eggshells even if it is less suited as a tool for assessing the 'quality' of eggshells per se.

References

Addadi, L., Raz, S. and Weiner, S. (2003) Taking advantage of disorder: Amorphous calcium carbonate and its roles in biomineralization. *Advanced Materials*, **15**, 959-970.

Addadi, L. and Weiner, S. (1992) Control and design principles in biological mineralization. *Angewandte Chemie-International Edition in English*, **31**, 153-169.

Addadi, L. and Weiner, S. (1985) Interactions between acidic proteins and crystals - stereochemical requirements in biomineralization. *Proceedings of the National Academy of Sciences of the United States of America*, **82**, 4110-4114.

Adderley, W. P., Alberts, I. L., Simpson, I. A. and Wess, T. J. (2004) Calcium-iron-phosphate features in archaeological sediments: characterization through microfocus synchrotron X-ray scattering analyses. *Journal of Archaeological Science*, **31**, 1215-1224.

Ahmed, A. M. H., Rodriguez-Navarro, A. B., Vidal, M. L., Gautron, J., Garcia-Ruiz, J. M. and Nys, Y. (2005) Changes in eggshell mechanical properties, crystallographic texture and in matrix proteins induced by moult in hens. *British Poultry Science*, **46**, 268-279.

Aizenberg, J., Weaver, J. C., Thanawala, M. S., Sundar, V. C., Morse, D. E. and Fratzl, P. (2005) Skeleton of Euplectella sp.: Structural hierarchy from the nanoscale to the macroscale. *Science*, **309**, 275-278.

Anderson, G. B. and Carter, T. C. (1976) Hens egg - shell cracking at impact on a heavy, stiff body and factors that affect it. *British Poultry Science*, **17**, 613-626.

Arias, J. L. and Fernandez, M. S. (2003) Biomimetic processes through the study of mineralized shells. *Materials Characterization*, **50**, 189-195.

Arias, J. L., Fink, D. J., Xiao, S. Q., Heuer, A. H. and Caplan, A. I. (1993) Biomineralization and eggshells: cell-mediated acellular compartments of mineralized extracellular matrix. *International Review of Cytology*, **145**, 217-250.

Arias, J. L., Carrino, D. A., Fernandez, M. S., Rodriguez, J. P., Dennis, J. E. and Caplan, A. I. (1992) Partial biochemical and immunochemical characterization of avian eggshell extracellular matrices. *Archives of Biochemistry and Biophysics*, **298**, 293-302.

Arias, J. L., Fernandez, M. S., Dennis, J. E. and Caplan, A. I. (1991) Collagens of the chicken eggshell membranes. *Connective Tissue Research*, **26**, 37-45.

Auvray, L. and Auroy, P. (1991) Scattering by interfaces: Variations on Porod's Law. In: *Neutron, X-Ray and Light Scattering: Introduction to an Investigative Tool for Colloidal and Polymeric Systems*. Zemb, T. (ed) North-Holland, Amsterdam.

Bain, M. M., Dunn, I. C., Wilson, P. W., Joseph, N., De Ketelaere, B., De Baerdemaeker, J. and Waddington, D. (2006) Probability of an egg cracking during packing can be predicted using a simple non-destructive acoustic test. *British Poultry Science*, **47**, 462-469.

Bain, M. M. (2005) Recent advances in the assessment of eggshell quality and their future application. *Worlds Poultry Science Journal*, **61**, 268-277.

Bain, M. M. (1992) Eggshell strength - a relationship between the mechanism of failure and the ultrastructural organization of the mammillary layer. *British Poultry Science*, **33**, 303-319.

Berry, A., Helsby, W. I., Parker, B. T., Hall, C. J., Buksh, P. A., Hill, A., Clague, N., Hillon, M., Corbett, G., Clifford, P., Tidbury, A., Lewis, R. A., Cernik, B. J., Barnes, P. and Derbyshire, G. E. (2003) The Rapid2 X-ray detection system. *Nuclear Instruments & Methods in Physics Research Section a - Accelerators Spectrometers Detectors and Associated Equipment*, **513**, 260-263.

Bolze, J., Peng, B., Dingenouts, N., Panine, P., Narayanan, T. and Ballauff, M. (2002) Formation and growth of amorphous colloidal $CaCO_3$ precursor particles as detected by time-resolved SAXS. *Langmuir*, **18**, 8364-8369.

Bu, Z. and Engelman, D. M. (1999) A method for determining transmembrane helix association and orientation in detergent micelles using small angle X-ray scattering. *Biophysical Journal*, 77, 1064-1073.

Butter, K., Kassapidou, K., Vroege, G. J. and Philipse, A. P. (2005) Preparation and properties of colloidal iron dispersions. *Journal of Colloid and Interface Science*, **287**, 485-495.

Cain, C. J. and Heyn, A. N. J. (1964) X-ray diffraction studies of the crystalline structure of the avian eggshell. *Biophysical Journal*, **4**, 23-39.

Carrino, D. A., Rodriguez, J. P. and Caplan, A. I. (1997) Dermatan sulfate proteoglycans from the mineralized matrix of the avian eggshell. *Connective Tissue Research*, **36**, 175-193.

Castagnola, P., Bet, P., Quarto, R., Gennari, M. and Cancedda, R. (1991) cDNA cloning and gene expression of chicken osteopontin. Expression of osteopontin mRNA in chondrocytes is enhanced by trypsin treatment of cells. *Journal of Biological Chemistry*, **266**, 9944-9949.

Cernik, R. J., Barnes, P., Bushnell-Wye, G., Dent, A. J., Diakun, G. P., Flaherty, J. V., Greaves, G. N., Heeley, E. L., Helsby, W., Jacques, S. D. M., Kay, J., Rayment, T., Ryan, A., Tang, C. C. and Terrill, N. J. (2004) The new materials processing beamline at the SRS Daresbury, MPW6.2. *Journal of Synchrotron Radiation*, **11**, 163-170.

Chanzy, H., Putaux, J. L., Dupeyre, D., Davies, R., Burghammer, M., Montanari, S. and Riekel, C. (2006) Morphological and structural aspects of the giant starch granules from Phajus grandifolius. *Journal of Structural Biology,* **154,** 100-110.

Cotton, J. P. (1991) Introduction to scattering experiments. In: *Neutron, X-Ray and Light Scattering: Introduction to an Investigative Tool for Colloidal and Polymeric Systems.* Zemb, T. (ed) North-Holland, Amsterdam.

Creger, C. R., Phillips, H., and Scott, J.T (1976) Formation of an egg shell. *Poultry Science,* **55,** 1717-1723.

Cullity, B. D. (1978) *Elements of X-ray Diffraction.* Addison-Wesley Publishing Company, Inc., Reading, Massachusetts.

Cusack, M., Fraser, A. C. and Stachel, T. (2003) Magnesium and phosphorus distribution in the avian eggshell. *Comparative Biochemistry and Physiology B - Biochemistry & Molecular Biology,* **134,** 63-69.

De Ketelaere, B., Bamelis, F., Kemps, B., Decuypere, E. and De Baerdemaeker, J. (2004) Non-destructive measurements of the egg quality. *Worlds Poultry Science Journal,* **60,** 289-302.

De Ketelaere, B., Govaerts, T., Coucke, P., Dewil, E., Visscher, J., Decuypere, E. and De Baerdemaeker, J. (2002) Measuring the eggshell strength of 6 different genetic strains of laying hens: techniques and comparisons. *British Poultry Science,* **43,** 238-244.

De Ketelaere, B., Coucke, P. and De Baerdemaeker, J. (2000) Eggshell crack detection based on acoustic resonance frequency analysis. *Journal of Agricultural Engineering Research,* **76,** 157-163.

Dennis, J. E., Xiao, S. Q., Agarwal, M., Fink, D. J., Heuer, A. H. and Caplan, A. I. (1996) Microstructure of matrix and mineral components of eggshells from white leghorn chickens (*Gallus gallus*). *Journal of Morphology,* **228,** 287-306.

Diamond, R. (1974) Real-space refinement of the structure of hen egg-white lysozyme. *Journal of Molecular Biology,* **82,** 371-391.

Dieckert, J. W., Dieckert, M. C. and Creger, C. R. (1989) Calcium reserve assembly - a basis structural unit of the calcium reserve system of the hen egg-shell. *Poultry Science,* **68,** 1569-1584.

Dominguez-Vera, J. M., Gautron, J., Garcia-Ruiz, J. M. and Nys, Y. (2000) The effect of avian uterine fluid on the growth behavior of calcite crystals. *Poultry Science,* **79,** 901-907.

Dunn, I. C., Bain, M., Edmond, A., Wilson, P. W., Joseph, N., Solomon, S., De Ketelaere, B., De Baerdemaeker, J., Schmutz, M., Preisinger, R. and Waddington, D. (2005) Heritability and genetic correlation of measurements derived from acoustic resonance

frequency analysis; a novel method of determining eggshell quality in domestic hens. *British Poultry Science,* **46,** 280-286.

Fernandez, M. S., Passalacqua, K., Arias, J. I. and Arias, J. L. (2004) Partial biomimetic reconstitution of avian eggshell formation. *Journal of Structural Biology,* **148,** 1-10.

Fernandez, M. S., Escobar, C., Lavelin, I., Pines, M. and Arias, J. L. (2003) Localization of osteopontin in oviduct tissue and eggshell during different stages of the avian egg laying cycle. *Journal of Structural Biology,* **143,** 171-180.

Fernandez, M. S., Moya, A., Lopez, L. and Arias, J. L. (2001) Secretion pattern, ultrastructural localization and function of extracellular matrix molecules involved in eggshell formation. *Matrix Biology,* **19,** 793-803.

Fernandez, M. S., Araya, M. and Arias, J. L. (1997) Eggshells are shaped by a precise spatio-temporal arrangement of sequentially deposited macromolecules. *Matrix Biology,* **16,** 13-20.

Fraser, A. C., Bain, M. M. and Solomon, S. E. (1999) Transmission electron microscopy of the vertical crystal layer and cuticle of the eggshell of the domestic fowl. *British Poultry Science,* **40,** 626-631.

Fraser, A. C., Bain, M. M. and Solomon, S. E. (1998) Organic matrix morphology and distribution in the palisade layer of eggshells sampled at selected periods during lay. *British Poultry Science,* **39,** 225-228.

Fratzl, P., Schreiber, S. and Klaushofer, K. (1996a) Bone mineralization as studied by small-angle x-ray scattering. *Connective Tissue Research,* **34,** 247-254.

Fratzl, P., Schreiber, S. and Boyde, A. (1996b) Characterization of bone mineral crystals in horse radius by small-angle X-ray scattering. *Calcified Tissue International,* **58,** 341-346.

Fratzl, P. (1994) Statistical model of the habit and arrangement of mineral crystals in the collagen of bone. *Journal of Statistical Physics,* 77, 125-143.

Fratzl, P., Groschner, M., Vogl, G., Plenk, H., Eschberger, J., Fratzlzelman, N., Koller, K. and Klaushofer, K. (1992) Mineral crystals in calcified tissues: a comparative study by SAXS. *Journal of Bone and Mineral Research,* 7, 329-334.

Fratzl, P., Fratzl-Zelman, N., Klaushofer, K., Vogl, G. and Koller, K. (1991) Nucleation and growth of mineral crystals in bone studied by small-angle X-ray scattering. *Calcified Tissue International,* **48,** 407-413.

Gautron, J., Hincke, M. T., Panheleux, M., Garcia-Ruiz, J. M., Boldicke, T. and Nys, Y. (2001a) Ovotransferrin is a matrix protein of the hen eggshell membranes and basal calcified layer. *Connective Tissue Research,* **42,** 255-267.

Gautron, J., Hincke, M. T., Mann, K., Panheleux, M., Bain, M., McKee, M. D., Solomon, S. E. and Nys, Y. (2001b) Ovocalyxin-32, a novel chicken eggshell matrix protein -

Isolation, amino acid sequencing, cloning, and immunocytochemical localization. *Journal of Biological Chemistry,* **276,** 39243-39252.

Gautron, J., Hincke, M. T. and Nys, Y. (1997) Precursor matrix proteins in the uterine fluid change with stages of eggshell formation in hens. *Connective Tissue Research,* **36,** 195-210.

Gautron, J., Bain, M., Solomon, S. and Nys, Y. (1996) Soluble matrix of hen's eggshell extracts changes *in vitro* the rate of calcium carbonate precipitation and crystal morphology. *British Poultry Science,* **37,** 853-866.

Glatter, O. (1991) Small-angle scattering and light scattering. In: *Neutron, X-ray and Light Scattering: Introduction to an Investigative Tool for Colloidal and Polymeric Systems.* Zemb, T. (ed) North-Holland, Amsterdam.

Glatter, O. and Kratky, O. (1982) *Small Angle X-ray Scattering.* Academic Press, London.

Glusker, J. P. and Trueblood, K. N. (1972) *Crystal structure analysis: A primer.* Oxford University Press, New York.

Gorres, J. H., Savin, M. C. and Amador, J. A. (2001) Soil micropore structure and carbon mineralization in burrows and casts of an anecic earthworm (Lumbricus terrestris). *Soil Biology & Biochemistry,* **33,** 1881-1887.

Guinier, A. and Fournet, G. (1955) *Small angle scattering of X-rays.* Wiley, New York.

Gupta, H. S., Roschger, P., Zizak, I., Fratzl-Zelman, N., Nader, A., Klaushofer, K. and Fratzl, P. (2003) Mineralized microstructure of calcified avian tendons: A scanning small angle X-ray scattering study. *Calcified Tissue International,* **72,** 567-576.

Hamilton, R. M. G. (1982) Methods and factors that affect the measurement of eggshell quality. *Poultry Science,* **61,** 2022-2039.

Hamilton, R. M. G., Hollands, K. G., Voisey, P. W. and Grunder, A. A. (1979a) Relationship between egg-shell quality and shell breakage and factors that affect shell breakage in the field - review. *Worlds Poultry Science Journal,* **35,** 177-190.

Hamilton, R. M. G., Thompson, B. K. and Voisey, P. W. (1979b) Effects of age and strain on the relationships between destructive and nondestructive measurements of eggshell strength for white leghorn hens. *Poultry Science,* **58,** 1125-1132.

Heeley, E. L., Kit Poh, C., Li, W., Maidens, A., Bras, W., Dolbnya, I. P., Gleeson, A. J., Terrill, N. J., Fairclough, J. P. A., Olmsted, P. D., Ristic, R. I., Hounslow, M. J. and Ryan, A. J. (2002) Are metastable, precrystallisation, density-fluctuations a universal phenomena? *Faraday Discussions,* **122,** 343-361.

Helsby, W. I., Berry, A., Buksh, P. A., Hall, C. J. and Lewis, R. A. (2003) The RAPID2 interpolating system. *Nuclear Instruments & Methods in Physics Research Section a - Accelerators Spectrometers Detectors and Associated Equipment,* **510,** 138-144.

Hernández- Hernández, A., Rodriguez-Navarro, A. and García-Ruiz, J. M. (2003) Influence of model proteins on the precipitation of calcium carbonate. In *Proceedings of the Xth European Symposium on the Quality of Eggs and Egg Products*, III. Saint-Brieuc, France.

Heuer, A. H., Fink, D. J., Laraia, V. J., Arias, J. L., Calvert, P. D., Kendall, K., Messing, G. L., Blackwell, J., Rieke, P. C., Thompson, D. H., Wheeler, A. P., Veis, A. and Caplan, A. I. (1992) Innovative materials processing strategies - a biomimetic approach. *Science*, **255,** 1098-1105.

Hiller, J. C. and Wess, T. J. (2006) The use of small-angle X-ray scattering to study archaeological and experimentally altered bone. *Journal of Archaeological Science*, **33,** 560-572.

Hiller, J. C., Thompson, T. J. U., Evison, M. P., Chamberlain, A. T. and Wess, T. J. (2003) Bone mineral change during experimental heating: an X-ray scattering investigation. *Biomaterials*, **24,** 5091-5097.

Hiller, J. C. (2003) Diagenesis of archaelogical bone in European pleistocene cave sites. Ph.D. Thesis, University of Sheffield, Sheffield.

Hincke, M. T., Gautron, J., Panheleux, M., Garcia-Ruiz, J., McKee, M. D. and Nys, Y. (2000) Identification and localization of lysozyme as a component of eggshell membranes and eggshell matrix. *Matrix Biology*, **19,** 443-453.

Hincke, M. T., Gautron, J., Tsang, C. P. W., McKee, M. D. and Nys, Y. (1999) Molecular cloning and ultrastructural localization of the core protein of an eggshell matrix proteoglycan, ovocleidin-116. *Journal of Biological Chemistry*, **274,** 32915-32923.

Hincke, M. T. (1995) Ovalbumin is a component of the chicken eggshell matrix. *Connective Tissue Research*, **31,** 227-233.

Hincke, M. T., Tsang, C. P. W., Courtney, M., Hill, V. and Narbaitz, R. (1995) Purification and immunochemistry of a soluble matrix protein of the chicken eggshell (ovocleidin-17). *Calcified Tissue International*, **56,** 578-583.

Howard C.J. and Hill R.J. (1986) LHMP: a computer program for Rietveld analysis of fixed wavelength X-ray and neutron powder diffraction patterns, AAEC (now ANSTO) Report M112, Lucas Heights Research Laboratory.

Hughes, B. O., Gilbert, A. B. and Brown, M. F. (1986) Categorization and causes of abnormal eggshells - relationship with stress. *British Poultry Science*, **27,** 325-337.

Kelly, A. and Groves, G. W. (1970) *Crystallography and Crystal Defects*. Longman, London.

Kennedy, C. J., Hiller, J. C., Lammie, D., Drakopoulos, M., Vest, M., Cooper, M., Adderley, W. P. and Wess, T. J. (2004) Microfocus X-ray diffraction of historical parchment reveals variations in structural features through parchment cross sections. *Nano Letters*, **4,** 1373-1380.

Kennedy, C. J. and Wess, T. J. (2003) The structure of collagen within parchment - A review. *Restaurator*, **24**, 61-80.

Kirkpatrick, P. and Baez, A. V. (1948) Formation of optical images by X-rays. *Journal of the Optical Society of America*, **38**, 766-774.

Krampitz, G. and Graser, G. (1988) Molecular mechanisms of biomineralization in the formation of calcified shells. *Angewandte Chemie-International Edition in English*, **27**, 1145-1156.

Kurokawa, H., Dewan, J. C., Mikami, B., Sacchettini, J. C. and Hirose, M. (1999) Crystal structure of hen apo-ovotransferrin - Both lopes adopt an open conformation upon loss of iron. *Journal of Biological Chemistry*, **274**, 28445-28452.

Kurokawa, H., Mikami, B. and Hirose, M. (1995) Crystal-structure of diferric hen ovotransferrin at 2.4 Angstrom resolution. *Journal of Molecular Biology*, **254**, 196-207.

La Scala, N., Bolelli, I., Ribeiro, L., Freitas, D. and Macari, M. (2000) Pore size distribution in chicken eggs as determined by mercury porosimetry. *Revista Brasileira Ciência Avícola*, **2**, 177-181.

Lavelin, I., Meiri, N. and Pines, M. (2000) New insight in eggshell formation. *Poultry Science*, **79**, 1014-1017.

Lengeler, B., Schroer, C., Tummler, J., Benner, B., Richwin, M., Snigirev, A., Snigireva, I. and Drakopoulos, M. (1999) Imaging by parabolic refractive lenses in the hard X-ray range. *Journal of Synchrotron Radiation*, **6**, 1153-1167.

Lipson, H. and Steeple, H. (1970) Analysis of the broadening of powder lines. In: *Interpretation of X-ray Powder Diffraction Patterns*. Macmillan and Co Ltd, London.

Lorenz-Haas, C., Muller-Buschbaum, P., Wunnicke, O., Cassignol, C., Burghammer, M., Riekel, C. and Stamm, M. (2003) Scanning microfocus small-angle X-ray scattering: A new tool to investigate defects at polymer-polymer interfaces. *Langmuir*, **19**, 3056-3061.

Lowenstam, H. A. and Weiner, S. (1989) *On Biomineralization*. Oxford University Press, New York.

Lowenstam, H. A. (1981) Minerals formed by organisms. *Science*, **211**, 1126-1131.

Mann, K., Gautron, J., Nys, Y., McKee, M. D., Bajari, T., Schneider, W. J. and Hincke, M. T. (2003) Disulfide-linked heterodimeric clusterin is a component of the chicken eggshell matrix and egg white. *Matrix Biology*, **22**, 397-407.

Mann, K., Hincke, M. T. and Nys, Y. (2002) Isolation of ovocleidin-116 from chicken eggshells, correction of its amino acid sequence and identification of disulfide bonds and glycosylated Asn. *Matrix Biology*, **21,** 383-387.

Mann, K. (1999) Isolation of a glycosylated form of the chicken eggshell protein ovocleidin and determination of the glycosylation site. Alternative glycosylation/phosphorylation at an N-glycosylation sequon. *Febs Letters*, **463,** 12-14.

Mann, K. and Siedler, F. (1999) The amino acid sequence of ovocleidin 17, a major protein of the avian eggshell calcified layer. *Biochemistry and Molecular Biology International*, **47,** 997-1007.

Mann, S. (2001) *Biomineralization: Principles and Concepts in Bioinorganic Materials Chemistry*. Oxford University Press, Oxford.

Matsushima, N., Akiyama, M., Terayama, Y., Izumi, Y. and Miyake, Y. (1984) The morphology of bone mineral as revealed by small-angle X- ray scattering. *Biochimica Et Biophysica Acta*, **801,** 298-305.

Matsushima, N., Akiyama, M. and Terayama, Y. (1982) Quantitative analysis of the orientation of mineral in bone from small-angle X-ray scattering patterns. *Japanese Journal of Applied Physics Part 1-Regular Papers Short Notes & Review Papers*, **21,** 186-189.

Matsushima, N., Akiyama, M. and Terayama, Y. (1981) Quantitative analysis of small-angle X-ray scattering of bone: determination of sizes of its collagen and apatite components. *Japanese Journal of Applied Physics*, **20,** 699-702.

Meenakshi, V. R., Hare, P. E. and Wilbur, K. M. (1971) Amino acids of the organic matrix of neogastropod shells. *Comparative Biochemistry and Physiology Part B: Biochemistry and Molecular Biology*, **40,** 1037-1043.

Mikkelsen, A., Andersen, A. B., Engelsen, S. B., Hansen, H. C. B., Larsen, O. and Skibsted, L. H. (1999) Presence and dehydration of ikaite, calcium carbonate hexahydrate, in frozen shrimp shell. *Journal of Agricultural and Food Chemistry*, **47,** 911-917.

Moura, M. J., Ferreira, P. J. and Figueiredo, M. M. (2005) Mercury intrusion porosimetry in pulp and paper technology. *Powder Technology*, **160,** 61-66.

Narayanan, T., Diat, O. and Bosecke, P. (2001) SAXS and USAXS on the high brilliance beamline at the ESRF. *Nuclear Instruments & Methods in Physics Research Section a-Accelerators Spectrometers Detectors and Associated Equipment*, **467,** 1005-1009.

Newman, R. H. (1999) Estimation of the lateral dimensions of cellulose crystallites using ^{13}C NMR signal strengths. *Solid State Nuclear Magnetic Resonance*, **15,** 21-29.

Nielsen-Marsh, C. M. and Hedges, R. E. M. (1999) Bone porosity and the use of mercury intrusion porosimetry in bone diagenesis studies. *Archaeometry*, **41,** 165-174.

Nimtz, M., Conradt, H. S. and Mann, K. (2004) LacdiNAc (GalNAc beta 1-4GlcNAc) is a major motif in N-glycan structures of the chicken eggshell protein ovocleidin-116. *Biochimica Et Biophysica Acta-General Subjects,* **1675,** 71-80.

Nisbet, A. D., Saundry, R. H., Moir, A. J. G., Fothergill, L. A. and Fothergill, J. E. (1981) The complete amino-acid sequence of hen ovalbumin. *European Journal of Biochemistry,* **115,** 335-345.

Nys, Y., Gautron, J., Garcia-Ruiz, J. M. and Hincke, M. T. (2004) Avian eggshell mineralization: biochemical and functional characterization of matrix proteins. *Comptes Rendus Palevol,* **3,** 549-562.

Nys, Y., Hincke, M. T., Arias, J. L., Garcia-Ruiz, J. M. and Solomon, S. E. (1999) Avian eggshell mineralization. *Poultry and Avian Biology Reviews,* **10,** 143-166.

Nys, Y., Zawadzki, J., Gautron, J. and Mills, A. D. (1991) Whitening of brown-shelled eggs: mineral composition of uterine fluid and rate of protoporphyrin deposition. *Poultry Science,* **70,** 1236-1245.

Pagliai, M., Vignozzi, N. and Pellegrini, S. (2004) Soil structure and the effect of management practices. *Soil & Tillage Research,* **79,** 131-143.

Panheleux, M., Nys, Y., Williams, J., Gautron, J., Boldicke, T. and Hincke, M. T. (2000) Extraction and quantification by ELISA of eggshell organic matrix proteins (ovocleidin-17, ovalbumin, ovotransferrin) in shell from young and old hens. *Poultry Science,* **79,** 580-588.

Panheleux, M., Bain, M., Fernandez, M. S., Morales, I., Gautron, J., Arias, J. L., Solomon, S. E., Hincke, M. and Nys, Y. (1999) Organic matrix composition and ultrastructure of eggshell: a comparative study. *British Poultry Science,* **40,** 240-252.

Paris, O., Zizak, I., Lichtenegger, H., Roschger, P., Klaushofer, K. and Fratzl, P. (2000) Analysis of the hierarchical structure of biological tissues by scanning X-ray scattering using a micro-beam. *Cellular and Molecular Biology,* **46,** 993-1004.

Parsons, A. H. (1982) Structure of the eggshell. *Poultry Science,* **61,** 2013-2021.

Perrott, H. R., Scott, V. D. and Board, R. G. (1981) Crystal orientation in the shell of the domestic-fowl - an electron-diffraction study. *Calcified Tissue International,* **33,** 119-124.

Pines, M., Knopov, V. and Bar, A. (1995) Involvement of osteopontin in egg shell formation in the laying chicken. *Matrix Biology,* **14,** 765-771.

Pontoni, D., Bolze, J., Dingenouts, N., Narayanan, T. and Ballauff, M. (2003) Crystallization of calcium carbonate observed in-situ by combined small- and wide-angle X-ray scattering. *Journal of Physical Chemistry B,* **107,** 5123-5125.

Potts, P. L. and Washburn, K. W. (1983) The relationship of age, method of measuring, and strain on variation in shell strength. *Poultry Science,* **62,** 239-246.

Pradhan, B., Nagesh, M. and Bhattacharjee, B. (2005) Prediction of the hydraulic diffusivity from pore size distribution of concrete. *Cement and Concrete Research*, **35,** 1724-1733.

Reyes-Grajeda, J. P., Jauregui-Zuniga, D., Rodriguez-Romero, A., Hernandez-Santoyo, A., Bolanos-Garcia, V. M. and Moreno, A. (2002) Crystallization and preliminary X-ray analysis of ovocleidin-17 a major protein of the *Gallus gallus* eggshell calcified layer. *Protein and Peptide Letters*, **9,** 253-257.

Rhodes, G. (2000) *Crystallography Made Crystal Clear*. Academic Press, San Diego.

Rietveld, H. M. (1967) Line profiles of neutron powder-diffraction peaks for structure refinement. *Acta Crystallographica*, **22**, 151-152.

Rietveld, H. M. (1969) A profile refinement method for nuclear and magnetic structures. *Journal of Applied Crystallography*, **2**, 65-71.

Robinson, D. S. and King, N. R. (1970) The structure of the organic mammillary cores in some weak egg shells. *British Poultry Science*, **11,** 39-44.

Rodriguez-Navarro, A., Kalin, O., Nys, Y. and Garcia-Ruiz, J. M. (2002) Influence of the microstructure on the shell strength of eggs laid by hens of different ages. *British Poultry Science*, **43,** 395-403.

Rodriguez-Navarro, A. and Garcia-Ruiz, J. M. (2000) Model of textural development of layered crystal aggregates. *European Journal of Mineralogy*, **12,** 609-614.

Schmidt, P. W., Avnir, D., Levy, D., Hohr, A., Steiner, M. and Roll, A. (1991) Small-angle X-ray scattering from the surfaces of reversed-phase silicas: power-law scattering exponents of magnitudes greater than 4. *Journal of Chemical Physics*, **94,** 1474-1479.

Schuster, M. and Göbel, H. (1995) Parallel-beam coupling into channel-cut monochromators using curved graded multilayers. *Journal of Physics D - Applied Physics*, **28,** A270-A275.

Sharp, R. M. and Silyn-Roberts, H. (1984) Development of preferred orientation in the eggshell of the domestic-fowl. *Biophysical Journal*, **46,** 175-180.

Silyn-Roberts, H. and Sharp, R. M. (1986) Crystal-growth and the role of the organic network in eggshell biomineralization. *Proceedings of the Royal Society of London Series B-Biological Sciences*, **227,** 303-324.

Simkiss, K. (1964) Phosphates as crystal poisons of calcification. *Biological Reviews*, **39,** 487-505.

Simons, P. C. M. (1971) Ultrastructure of the hen's egg and its physiological interpretation. Ph.D. Thesis Communication No. 175 Het Spelderholt, Beekbergen, The Netherlands.

Snigirev, A., Kohn, V., Snigireva, I. and Lengeler, B. (1996) A compound refractive lens for focusing high-energy X-rays. *Nature,* **384,** 49-51.

Solomon, S. E. (1991) *Egg and Eggshell Quality.* Wolfe Publishing, London.

Somogyi, A., Drakopoulos, M., Vincze, L., Vekemans, B., Camerani, C., Janssens, K., Snigirev, A. and Adams, F. (2001) ID18F: a new micro-x-ray fluorescence end-station at the European Synchrotron Radiation Facility (ESRF): preliminary results. *X-Ray Spectrometry,* **30,** 242-252.

Stein, P. E., Leslie, A. G. W., Finch, J. T. and Carrell, R. W. (1991) Crystal-structure of uncleaved ovalbumin at 1.95 Å resolution. *Journal of Molecular Biology,* **221,** 941-959.

Stout, G. H. and Jensen, L. H. (1968) *X-ray Structure Determination. A Practical Guide.* The Macmillan Company, New York.

Svergun, D. I., Semenyuk, A. V. and Feigin, L. A. (1988) Small-angle scattering data treatment by the regularization method. *Acta Crystallographica Section A,* **44,** 244-250.

Tang, C. C., Martin, C. M., Laundy, D., Thompson, S. P., Diakun, G. P. and Cernik, R. J. (2004) X-ray beam characteristics on MPW6.2 at the SRS. *Nuclear Instruments and Methods in Physics Research Section B: Beam Interactions with Materials and Atoms,* **222,** 659-666.

Terepka, A. R. (1963) Structure and calcification in avian egg shell. *Experimental Cell Research,* **30,** 171-182.

Thomas, J. J., Jennings, H. M. and Allen, A. J. (1998) The surface area of cement paste as measured by neutron scattering: Evidence for two C-S-H morphologies. *Cement and Concrete Research,* **28,** 897-905.

Tlili, M. M., Ben Amor, M., Gabrielli, C., Joiret, S., Maurin, G. and Rousseau, P. (2001) Characterization of $CaCO_3$ hydrates by micro-Raman spectroscopy. *Journal of Raman Spectroscopy,* **33,** 10-16.

Tyler, C. (1956) Studies on egg shells. VII. Some aspects of structure as shown by plastic models. *Journal of the Science of Food and Agriculture,* **7,** 483-493.

van Veen, B., Pajander, J., Zuurman, K., Lappalainen, R., Poso, A., Frijlink, H. W. and Ketolainen, J. (2005) The effect of powder blend and tablet structure on drug release mechanisms of hydrophobic starch acetate matrix tablets. *European Journal of Pharmaceutics and Biopharmaceutics,* **61,** 149-157.

Voisey, P. W. and Hunt, J. R. (1974) Measurement of eggshell strength. *Journal of Texture Studies,* **5,** 135-182.

Waigh, T. A., Hopkinson, I., Donald, A. M., Butler, M. F., Heidelbach, F. and Riekel, C. (1997) Analysis of the native structure of starch granules with X-ray microfocus diffraction. *Macromolecules,* **30,** 3813-3820.

Wess, T. J., Alberts, I., Hiller, J., Drakopoulos, M., Chamberlain, A. T. and Collins, M. (2001a) Microfocus small angle X-ray scattering reveals structural features in archaeological bone samples: Detection of changes in bone mineral habit and size. *Calcified Tissue International,* **70,** 103-110.

Wess, T. J., Drakopoulos, M., Snigirev, A., Wouters, J., Paris, O., Fratzl, P., Collins, M., Hiller, J. and Nielsen, K. (2001b) The use of small-angle x-ray diffraction studies for the analysis of structural features in archaeological samples. *Archaeometry,* **43,** 117-129.

Wess, T. J., Alberts, I., Cameron, G., Laurie, C., Orgel, J., Hiller, J., Nielsen Marsh, C., Balthazar, V., Drakopoulos, M., Pollard, M. and Collins, M. (2000) Small angle X-ray scattering reveals; changes of bone mineral habit and size in archaeological bone samples. *Fibre Diffraction Review,* **9,** 36-43.

Wolford, J. H. and Tanaka, K. (1970) Factors influencing egg shell quality. *Worlds Poultry Science Journal,* **26,** 763-780.

Wong, M., Hendrix, M. J. C., Vondermark, K., Little, C. and Stern, R. (1984) Collagen in the eggshell membranes of the hen. *Developmental Biology,* **104,** 28-36.

Zhou, Y. Q. (1998) Salt effects on protein titration and binding. *Journal of Physical Chemistry B,* **102,** 10615-10621.